

An International  
Forum For  
The AE Science  
and Technology

# JOURNAL OF ACOUSTIC EMISSION

Vol.36/January-December 2019

Editors: M.A. Hamstad (AEWG) and G. Manthei (EWGAE)

- 36-001 Receiving Sensitivities of Acoustic Emission Sensors: A data  
Compilation Kanji Ono
- 36-001EX Data File for 36-001
- 36-009 Use of Acoustic Emission for Studying Ratcheting Behavior of 304LN Stainless  
Steel Elbows C.K. Mukhopadhyay, T.K. Haneef, Suneel K. Gupta,  
Vivek Bhasin, S. Vishnuvardhan, G. Raghava and P. Gandhi
- 36-039 Far-field wave propagation signals from pencil lead breaks on the open end  
of a thick-walled layered cylinder: Part 1 Amplitudes and frequency content  
M. A. Hamstad
- 36-051 Far-field Wave Propagation Signals from Pencil Lead Breaks on the Open End  
of a Thick-walled Layered Cylinder: Part 2 Modes of wave propagation  
M. A. Hamstad
- 36-071 Detection of Defects in Spur Gears by Acoustic Emission Monitoring  
Swati Gautam and Naresh Tandon

Proceedings of International Conference on Acoustic Emission - 9  
Part I and II

Endorsed by  
AEWG  
and  
EWGAE

Published by  
Acoustic Emission Group  
Encino, CA USA  
©2019 Acoustic Emission Group

# Receiving Sensitivities of Acoustic Emission Sensors: A data compilation

**Kanji Ono**

Department of Materials Science and Engineering, University of California, Los Angeles (UCLA), Los Angeles, CA 90095, USA

## Abstract

This technical note presents the receiving displacement sensitivities of 20 AE sensors that have not been reported and 21 previously reported sensitivity spectra. These were obtained using the same calibration method and provide the basis of rational comparison.

**Keywords:** AE sensors, receiving displacement sensitivities, direct contact method, laser calibration, velocity response, normally incident waves

## Introduction

A recent series of publications examined calibration methods of acoustic emission (AE) sensors and reported receiving displacement sensitivities of 25 sensors [1-4]. Nineteen more sensors were tested for their receiving sensitivities for normally incident waves, but remain unpublished. These will be useful for selecting a sensor for various uses and are presented here. While the receiving sensitivities are for the particular sensors tested, they represent typical sensor behaviors for identical models. All the sensors were tested using the same method and can be directly compared among them, a total of 45 models. An Excel file of the data is made available for research uses of non-commercial nature (see Appendix) and can be converted to velocity or pressure calibration schemes. Responses to bar waves and plate waves were reported in [4,5]. Less than 15 sensors were tested so far for guided wave sensitivities, however.

## Experimental Procedures

The transmission sensitivities of reference transducers were determined using a laser interferometer (Thales Laser SH-140) by exciting the transducers using short pulses of 200 -360 V peak values and determining their displacement responses. Transmitters used for the present work were FC500 (Acoustic Emission Technology), and V101, V103, V104, V189 and V192 (Olympus). Sensor under test (SUT) is coupled to the face of a calibrated transmitter in direct contact (the so-called face-to-face arrangement) using Vaseline as couplant. The transmitter and SUT were held with a weight or in a screw press. Received signals were fed to a digital oscilloscope (PicoScope 3405A) with 10-k $\Omega$  input termination to simulate a typical AE preamplifier input impedance. Digitization rate was 500 MHz and the duration of received signals was between 50 and 200  $\mu$ s. For this work, the pulse input was unchanged between the transmitter calibration and AE sensor calibration, so a spectral division (subtraction in dB-scale) produced the receiving sensitivities in terms of V/nm. Results are given in the decibel scale in reference to 0 dB at 1 V/nm. The FFT routine of Noesis (ver. 5.8, Mistras) was used for converting time domain signals into the frequency domain. Details were given in [1-5].

Most of the AE sensors tested for this study were borrowed from their manufacturers and were their demonstration units in near new conditions. Some from other sources were used for some times (marked with \* and estimated length of use in years). These are: PAC R.45, R3 $\alpha$ ,

picoHF1.2, picoHF1.5, F15 $\alpha$ , F50 $\alpha$ ,  $\mu$ 30 and  $\mu$ 100, Vallen VS30\* (5 years), VS75\* (5 years), VS150 and VS900, Soundwel SR40M, SR150M, SR150N, SR150S, MG50 and WG50, NF AE900M\* (10+ years) and Fuji Ceramics REF-VL\* (5 years). Of these sensors, low frequency parts to 100 kHz for PAC R.45 and R3 $\alpha$  were in [4], but the receiving sensitivities to 500 kHz are given here. For comparison, 18 previously reported sensitivities are also given for PAC R6 $\alpha$ , R15\* (25 years), R15 $\alpha$ , F30 $\alpha$ , WD\* (25 years), pico\* (20 years), S9220, HD50, Olympus V103, Digital Wave B1080\* (25 years), DECI SH225\* (15 years), Valpey Fisher pinducer (VP1093), Score Atlanta SE1000H and KRN BBPCP. Also included are GMuG MA20-400, MA30-200, MA40 and MA40-100 from Gesellschaft für Materialprüfung und Geophysik, Bad Nauheim, Germany. The remaining seven sensors are ultrasonic transducers or ones no longer available (FC500). Three of them, V101, V104 and NDT C16, are included in the data file. Note that the data file identifies 10 sensors borrowed from the manufacturers by letter codes only.

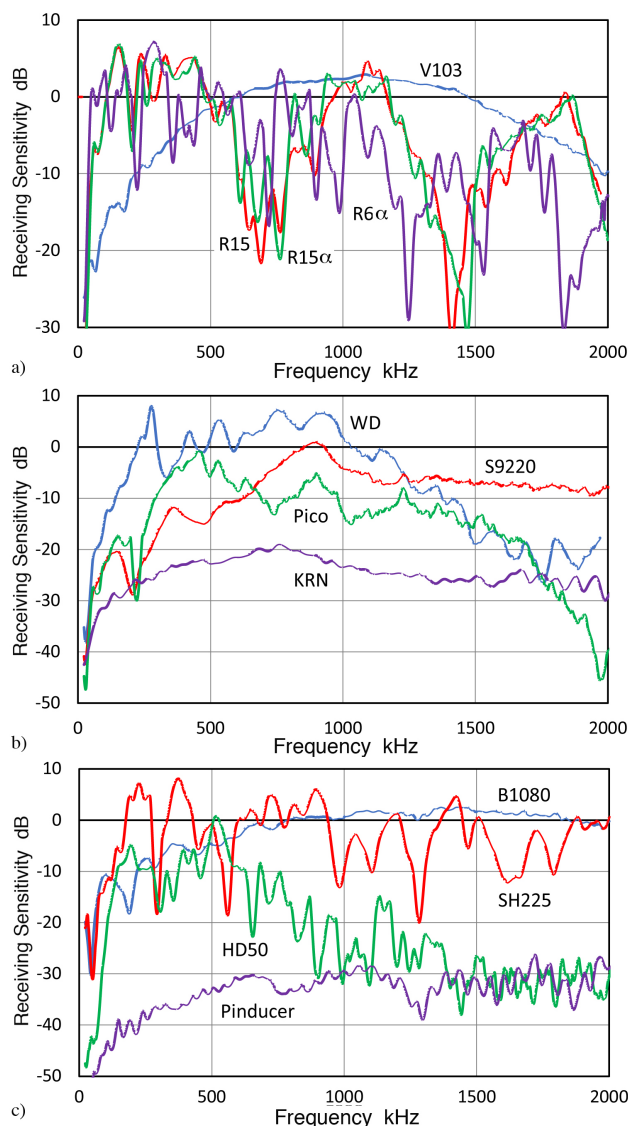


Fig. 1. Receiving displacement sensitivities in dB in reference to 0 dB at 1 V/nm against frequency in kHz. a) V103 (blue), R6 $\alpha$  (purple), R15 (red) and R15 $\alpha$  (green). b) WD (blue), KRN BB-PCP (purple), S9220 (red) and pico (green). c) DW B1080 (blue), Pinducer (purple), SH225 (red) and HD50 (green).

## Results

Receiving displacement sensitivities in dB in reference to 0 dB at 1 V/nm are plotted against frequency in kHz in the following figures. Figure 1 shows those of 12 previously reported sensors, as indicated in the figure. Figure 1a) shows a smooth spectrum for an ultrasonic transducer, V103. This has been used as wideband sensors for rock salt monitoring [6]. Its peak sensitivity is comparable to other high-frequency sensors examined here. Three others are resonance sensors, showing numerous peaks and valleys as expected, with their peaks of around 5 dB. Figure 1b) shows four wideband sensors. While WD has peaks of 7-8 dB, others have lower sensitivities due to their small sizes since the sensitivity decreases in proportion to the sensing area. KRN sensor has 1-mm diameter sensing element and pico sensor has 3.2-mm diameter. This contributes to 20 dB difference in the peak sensitivities as observed here. Figure 1c) has an FET-buffered B1080, which has a relatively flat response and good sensitivities at 600-2000 kHz. SH225 was designed for shear response, but has high peaks as in other resonant sensors. Pinducer has 1.3-mm diameter sensing element and has lower sensitivities than KRN, with generally flat, but fluctuating sensitivities above 500 kHz.

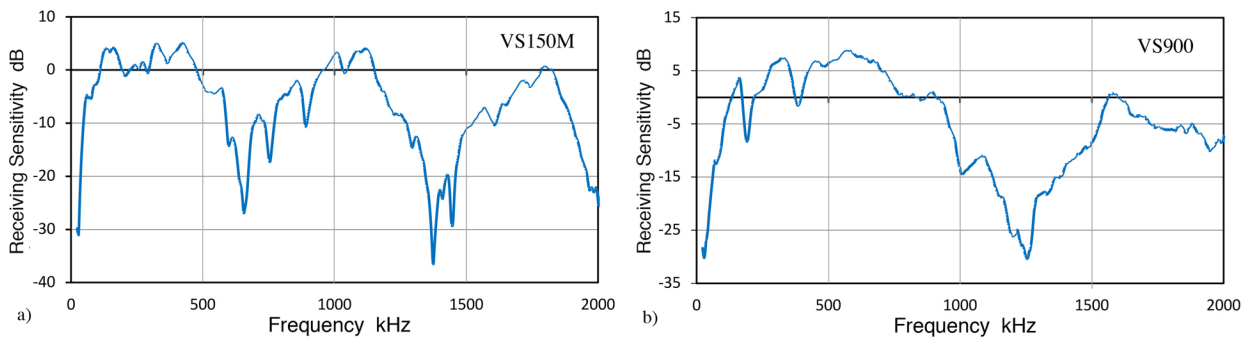


Fig. 2. Receiving displacement sensitivities in dB in reference to 0 dB at 1 V/nm against frequency in kHz. a) Vallen VS150M, b) VS900.

Figure 2 shows two resonant sensors from Vallen. Overall responses are similar to other sensors with prominent resonances. Peak values are 5-8 dB. Both sensors have no large dips near the peak sensitivity range. Figure 3 is also for resonant sensors. These are from Soundwel. Both SR150 M and 150N have high peak sensitivities of 11-12 dB, while SR150S has decreasing sensitivities above the peak with higher frequency peaks at ~15 dB lower from the peak near 220 kHz. Figure 4 gives the sensitivity curves for newer design sensors, with nearly flat peak sensitivities. These are F15 $\alpha$ , F30 $\alpha$  and f50 $\alpha$ , showing 12-13 dB peak sensitivities. These have flat sensitivity range of  $\pm 3$  dB over 200 to 600 kHz, including the peak frequency within the flat zone. Of these three, F30 $\alpha$ 's spectrum was previously reported in [4].

The next two figures show the receiving sensitivities of low frequency sensors. Figure 5 gives sensor spectra for PAC R0.45 and R3 $\alpha$ , and Fig. 6 for Vallen VS30 and VS75. The designations are meant for low frequency sensitivities, but in the case of normally incident waves, responses remain in many of them. Figure 7 gives sensitivity spectra for Soundwel WG50, MG50, and SR40M. The first two show broad responses centering at 500 kHz, while Fig. 7c) is a low frequency sensor, peaking at 55 kHz. This unit showed the highest peak response among the tested sensors.

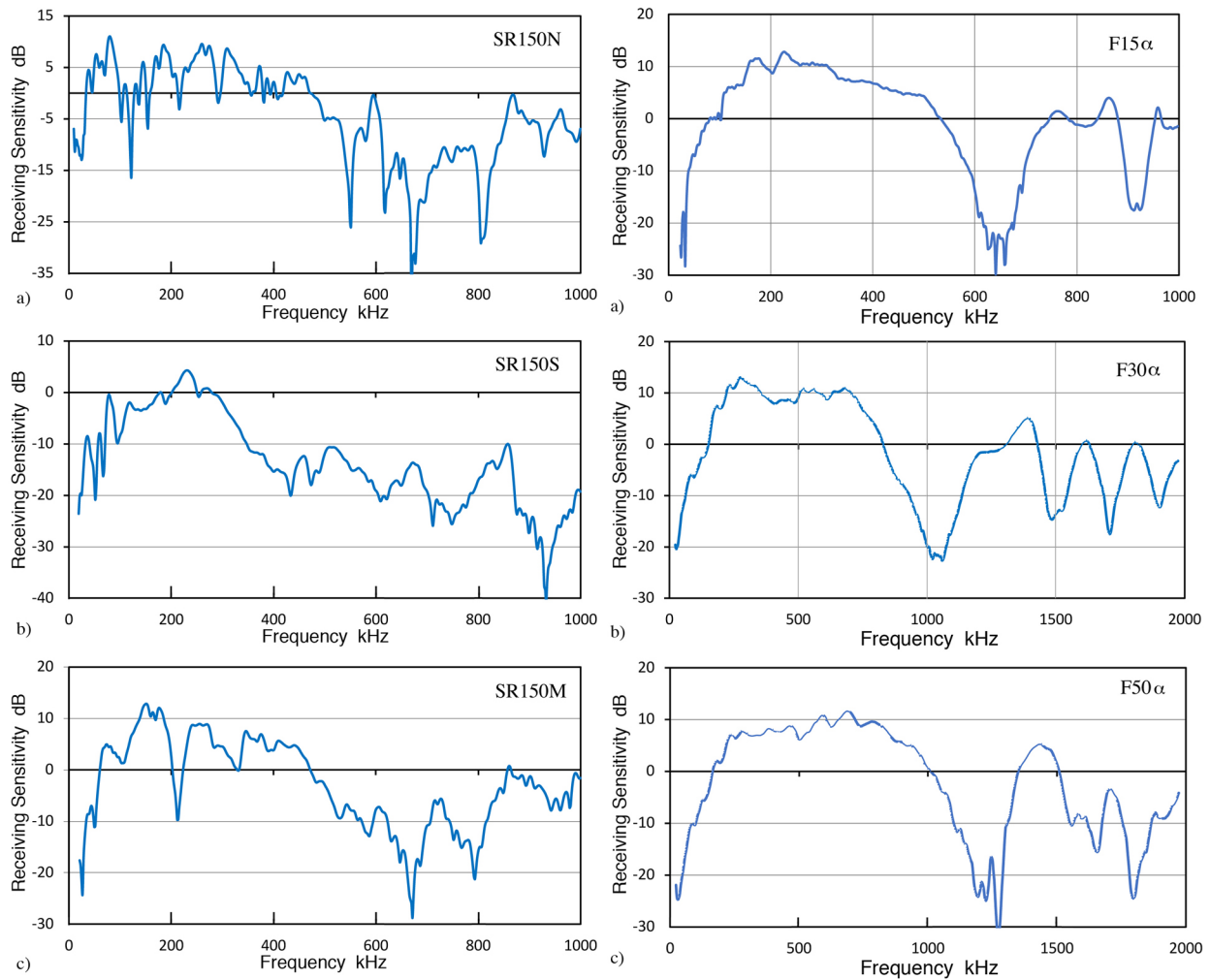


Fig. 3. Receiving displacement sensitivities in dB in reference to 0 dB at 1 V/nm against frequency in kHz. a) Soundwel SR150N, b) SR150S, c) SR150M.

Fig. 4. Receiving displacement sensitivities in dB in reference to 0 dB at 1 V/nm against frequency in kHz. a) PAC F15 $\alpha$ , b) F30 $\alpha$ , c) F50 $\alpha$ .

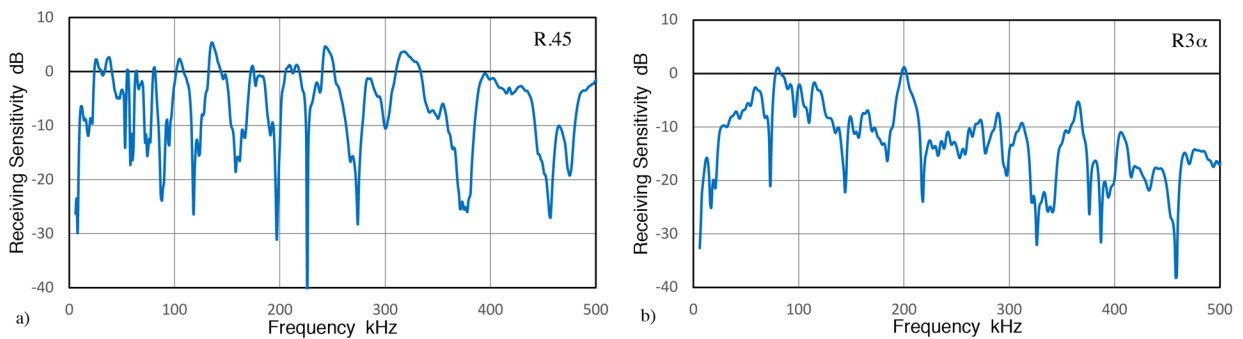


Fig. 5. Receiving displacement sensitivities in dB in reference to 0 dB at 1 V/nm against frequency in kHz. a) PAC R0.45, b) R3 $\alpha$ .

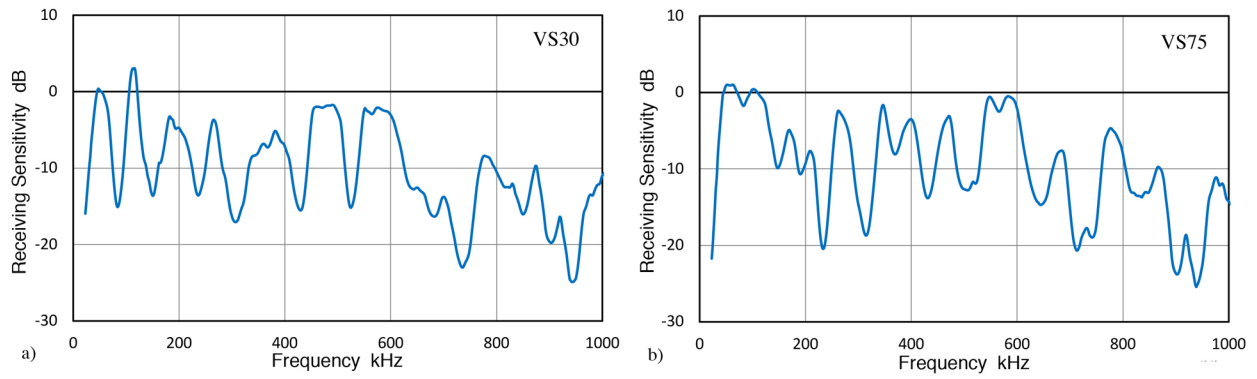


Fig. 6. Receiving displacement sensitivities in dB in reference to 0 dB at 1 V/nm against frequency in kHz. a) Vallen VS30, b) VS75.

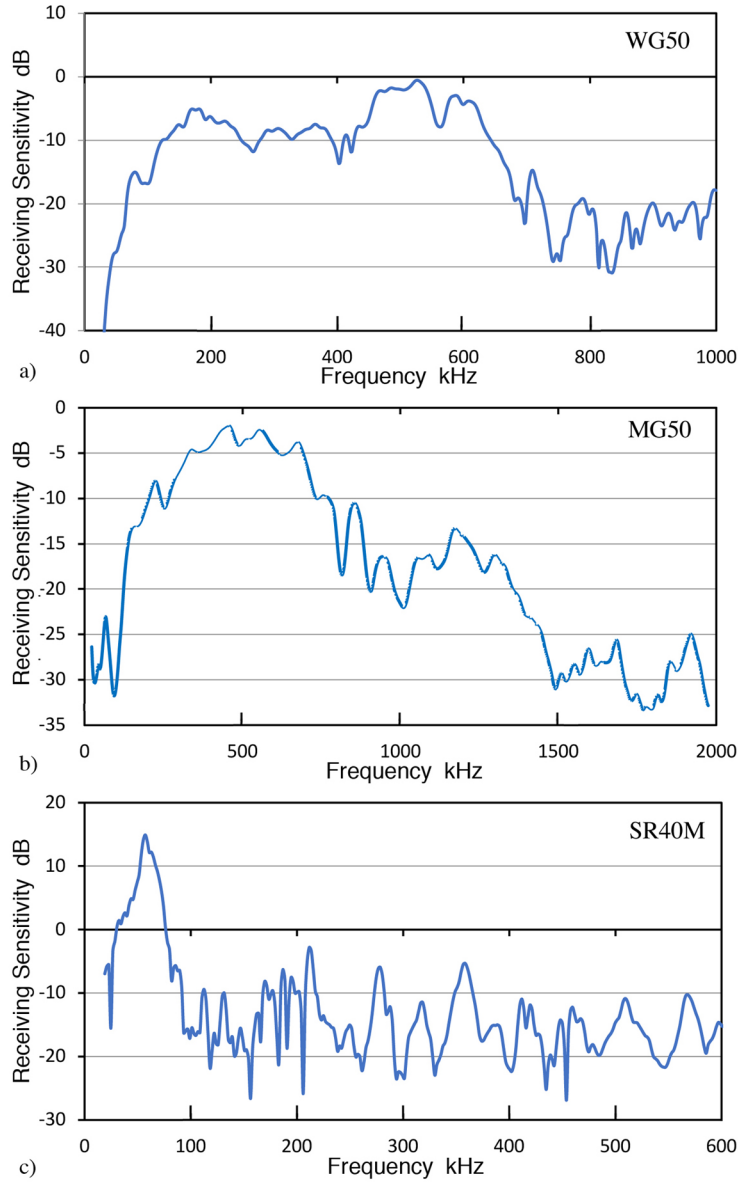


Fig. 7. Receiving displacement sensitivities in dB in reference to 0 dB at 1 V/nm against frequency in kHz. a) Soundwel WG50, b) MG50, c) SR40M.

Figures 8 and 9 show the receiving sensitivities of small sized sensors. Figure 8 gives responses to  $\mu 30$  and  $\mu 100$ . Both have the highest peak of about 10 dB in the 200-300 kHz range. While  $\mu 30$  starts to have reduced response beyond 600 kHz,  $\mu 100$  maintains good responses to 1300 kHz. PicoHF sensors on Fig. 9 have similar sizes like Pico sensor (response shown in Fig. 1b) and show the peak near 500 kHz, like Pico. The high frequency responses to 1.5 MHz are similar among the three, but HF versions keep responses to 2 MHz.

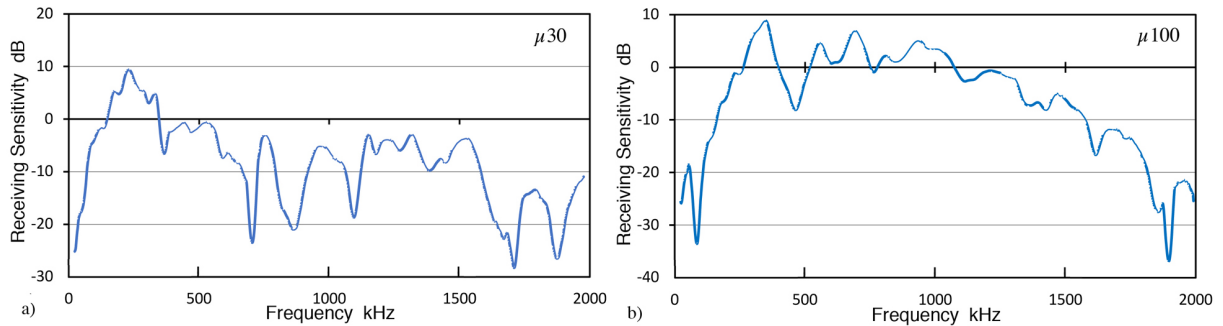


Fig. 8. Receiving displacement sensitivities in dB in reference to 0 dB at 1 V/nm against frequency in kHz. a) PAC  $\mu 30$ , b)  $\mu 100$ .

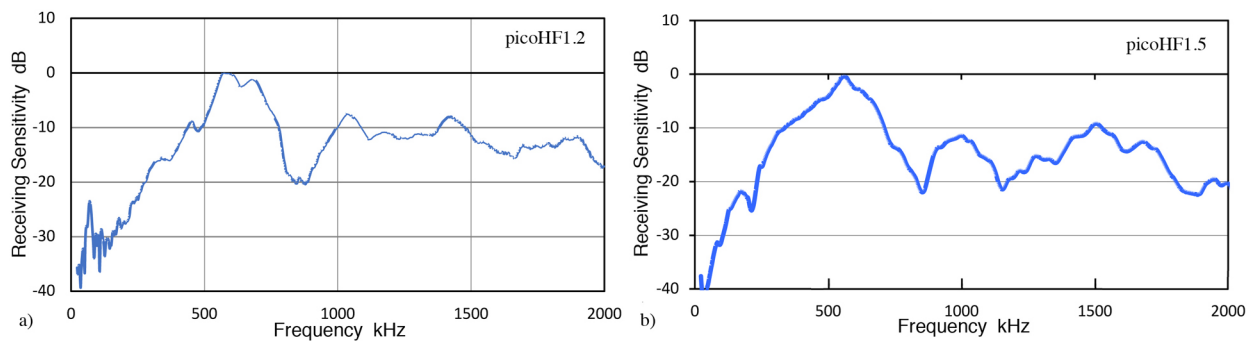


Fig. 9. Receiving displacement sensitivities in dB in reference to 0 dB at 1 V/nm against frequency in kHz. a) PicoHF1.2, b) PicoHF1.5.

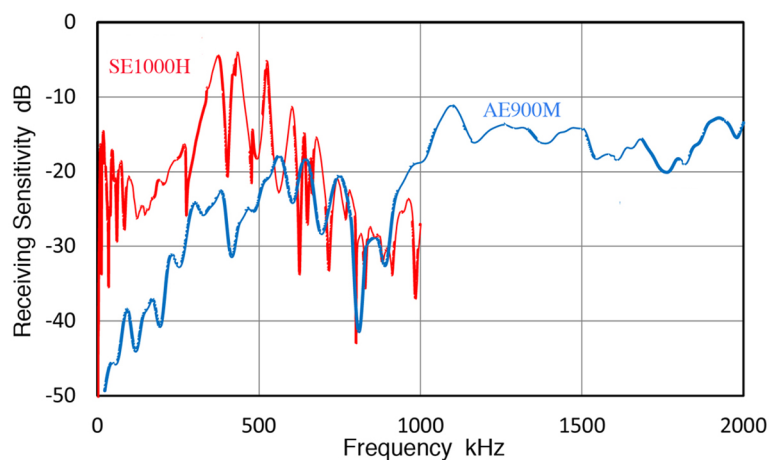


Fig. 10. Receiving displacement sensitivities in dB in reference to 0 dB at 1 V/nm against frequency in kHz. SE1000E (red curve), AE900M (blue curve).

Figure 10 shows the receiving sensitivities of sensors designated as broadband. The response of Score Atlanta (formerly DECI) SE1000H is given in Fig. 10a). This was reported in [3]. SE1000H shows many peaks (of above  $-20$  dB) from 10 kHz to 680 kHz. Figure 10b) is the response of NF AE900M and shows the mean value ( $\pm$ SD) of  $-15.6 \pm 2.1$  dB over 1 to 2 MHz.

Another broadband sensor is from Fuji Ceramics, REF-VL. It has a smooth spectrum, as shown in Fig. 11. The displacement response (blue curve) is similar to Olympus V101 (0.5 MHz transducer) [1], with a dip at 963 kHz. Here, both displacement (blue curve) and velocity (green curve) response spectra are shown so that the latter can be compared to factory calibration (red curve) only available in velocity response. The two velocity spectra matched well between 30 to 930 kHz. The average difference ( $\pm$ SD) was  $3.21 \pm 1.18$  dB. Also plotted in Figure 11 is the velocity response of AE900M, converted from the displacement spectrum in Fig. 10 (purple curve). In the displacement to velocity conversion, the low frequency parts are raised so that the entire spectrum becomes flatter. In this case, the average became  $24.33 \pm 4.35$  dB over 20 kHz to 2 MHz. This dB scale is in reference to 0 dB at 1 V/m/s. A calibration curve for AE900M sensor was recently reported [7] and matches to the present curve well in terms of the peak sensitivity and the amplitude range over 0 – 2 MHz. The sensors tested in this work were five to more than ten years old, but the sensitivities are comparable, respectively.

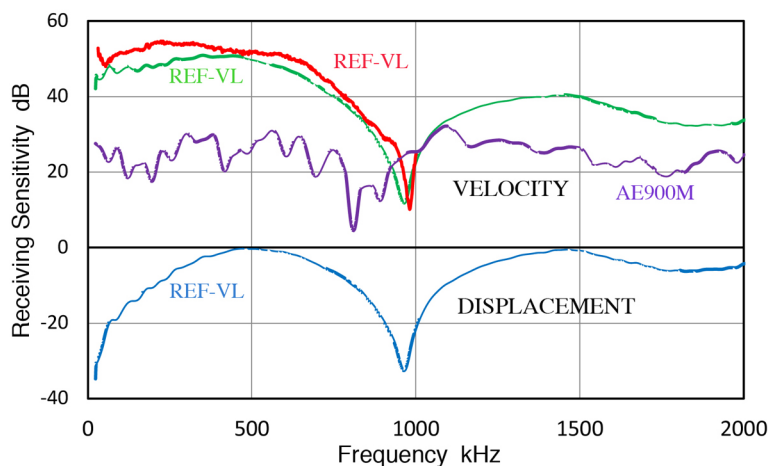


Fig. 11. Receiving displacement sensitivities in dB in reference to 0 dB at 1 V/nm against frequency in kHz for REF-VL (blue curve). Receiving velocity sensitivities in dB in reference to 0 dB at 1 V/m/s against frequency in kHz for AE900M (purple curve), REF-VL (green) and factory calibration for REF-VL (red).

## Discussion

Displacement sensitivities ( $R_x$ ) shown above can be converted to velocity sensitivities ( $R_v$ ) or pressure sensitivities ( $R_p$ ) by the following:

$$R_v = R_x - 20 \log(2\pi f) + 180$$

and

$$R_p = R_v - 143.3,$$

where  $f$  is in Hz,  $R_x$ ,  $R_v$  and  $R_p$  are all in dB scale. Reference for  $R_v$  is at 0 dB for 1 V/m/s and for  $R_p$  at 0 dB for 1 V/ $\mu$ bar. At 20 kHz,  $20 \log(2\pi f)$  corresponds to 102.0 dB and  $R_v$  is 78 dB

higher than Rx. At 2 MHz, the difference is reduced to 38.0 dB. These changes can be seen in Fig. 11 above between blue (Rx) and green (Rv) curves. The above conversion is shown as the last three columns in the sensor data file.

## Appendix

An Excel file accompanies this technical note. The data of this file is to be used only for research purposes of non-commercial nature. (For other uses, contact the author at [ono@ucla.edu](mailto:ono@ucla.edu).) Each column provides receiving displacement sensitivities in dB in reference to 0 dB at 1 V/nm. Some sensor names are only given in letter codes since no agreements with the manufacturers were formalized as to the publication of numerical data. A total of 41 spectra are given. Two of them are duplicates of the same type sensors (KRN and PAC R6 $\alpha$ ). The last three columns on both sheets provide examples of conversion to velocity or pressure sensitivities. The first column gives the values of  $20 \cdot \log(2\pi f) - 180$  that corresponds to the frequency (in kHz) given in column A, the second the velocity sensitivities (Rv), and the third pressure sensitivities (Rp).

## References

1. K. Ono, Calibration methods of acoustic emission sensors, *Materials*, (2016), **9**, 508; doi:10.3390/ma9070508.
2. K. Ono, Critical examination of ultrasonic transducer characteristics and calibration methods, *Res. Nondestruct. Eval.* (2017), **28**, 1–46; doi: 10.1080/09349847.2017.1375585.
3. K. Ono, Frequency dependence of receiving sensitivity of ultrasonic transducers and acoustic emission sensors, *Sensors*, (2018), **18**, 3861; doi:10.3390/s18113861.
4. K. Ono, T. Hayashi, H. Cho, Bar-wave calibration of acoustic emission sensors, *Appl. Sci.* (2017), **7**, 964; doi:10.3390/app7100964.
5. K. Ono, On the piezoelectric detection of guided ultrasonic waves, *Materials*, (2017), **10**, 1325; doi:10.3390/ma10111325.
6. G. Manthei, Characterization of acoustic emission sources in a rock salt specimen under triaxial compression, *Bull. Seismol. Soc. America* (2005), **95**(5), 1674-1700; doi:10.1785/0120040076.
7. M. Haas, U. Cihak-Bayr, C. Tomastik, M. Jech, and M. Gröschl, Primary calibration by reciprocity method of high-frequency acoustic-emission piezoelectric transducers, *J. Acoust. Soc. America*, (2018), **143**, 3557; doi: 10.1121/1.5041266.

# Use of Acoustic Emission for Studying Ratcheting Behavior of 304LN Stainless Steel Elbows

C. K. Mukhopadhyay<sup>1</sup>, T. K. Haneef<sup>1</sup>, Suneel K. Gupta<sup>2</sup>, Vivek Bhasin<sup>2</sup>,  
S. Vishnuvardhan<sup>3</sup>, G. Raghava<sup>3</sup> and P. Gandhi<sup>3</sup>

<sup>1</sup>Non-Destructive Evaluation Division, Indira Gandhi Centre for Atomic Research, Kalpakkam Tamil Nadu 603 102, India; <sup>2</sup>Reactor Safety Division, Bhabha Atomic Research Centre, Trombay, Mumbai 400 085, India; <sup>3</sup>Structural Engineering Research Centre, Council of Scientific & Industrial Research Taramani, Chennai 600 113, India

## Abstract

Acoustic emission technique (AET) has been used for studying ratcheting behavior of elbows made of AISI type 304LN stainless steel. High pressure piping and elbows in nuclear power plants are subjected to large amplitude reverse cyclic loading during an earthquake and the stresses are likely to exceed the elastic limit. A strong possibility for the accumulation of plastic strain by ratcheting thus exists in such components. Monitoring cyclic strain and ovality are normally done to predict damage in pressurized components during ratcheting. The novelty of the present work is the use of acoustic emission (AE) for getting information about the damage and formation of cracks during the ratcheting tests in elbow specimens. The tests were carried out under steady internal pressure and cyclic bending. During the ratcheting tests, the first significant increase in AE signal occurred at around 214 cycles and 103 cycles for the two elbows, and this has been attributed to crack initiation. Higher AE generated beyond that has been attributed to crack growth. Different parameters of the AE signal have been used to substantiate the results.

**Keywords:** Ratcheting, AISI type 304LN stainless steel, crack initiation, piping, elbow, acoustic emission

## 1. Introduction

Ratcheting in a component/structure occurs when it undergoes cyclic loading to constant stress levels, and the resulting plastic strain accumulates from cycle to cycle [1]. During ratcheting, the mean strain (mean of maximum and minimum strain during one cycle) changes during any one cycle at one point or several points of the structure and leads to a reduction in fatigue life of the structure by the loss of ductility.

The phenomenon of ratcheting has been studied by different investigators for different materials including SA 333 Gr. 6 steel [1,2], SA 516 Gr. 70 steel [3] and AISI type 304 stainless steel [4]. A study on SA 333 Gr. 6 steel pressurized elbows was carried out to understand the ratcheting [1,2]. SA means that the ASTM standard has been approved / adopted by Boiler & Pressure Vessel Code by ASME and Gr. means grade. SA 333 Gr. 6 is the steel used in primary heat transport piping of nuclear power plants. In SA 333 Gr. 6 steel the ratcheting strain and mean stress were found to affect the low cycle fatigue life significantly [1,2]. The effect of mean tensile stress with and without ratcheting strain on fatigue life of SA 516 Gr. 70 steel was studied [3]. Thin walled tubular specimens with total length 165.2 mm and dia 28.55 mm at the center were used. It was reported that both tensile mean stress and ratcheting strain have detrimental effects on the fatigue life [3]. The cyclic strain characteristics, ratcheting and failure behavior of

304 stainless steel were studied under uniaxial cyclic loading [4]. Round specimens with diameter as 8 mm and gage length as 30 mm were used. The material showed cyclic hardening, and this depends on strain amplitude. The cyclic hardening also results in a decrease in ratcheting strain rate gradually with the number of cycles [4]. The ratcheting strain was determined as the average of maximum and minimum axial strains in each cycle; and the ratcheting strain rate was defined as the increment of ratcheting strain in each cycle [4]. A number of elbows made of carbon and stainless steels were tested under steady internal pressure, and dynamic in-plane bending moments and the cyclic strain developed for each component was studied [5]. Ratcheting strain was found to be higher in the crown hoop direction compared to the axial direction and increased rapidly after initiation. Cyclic loading experiments with or without internal pressure on pipes and elbows with wall thinning were carried out under displacement control [6]. The failure occurred by crack initiation and growth accompanying ratchet swelling or crack initiation and growth after local buckling [6].

Piping and elbow components in nuclear power plants which are under high pressure, are subjected to large amplitude reverse cyclic loading during an earthquake, where the stresses may exceed the elastic limit. Under such situation, the plastic strain may accumulate in these components by ratcheting and may result in a reduction in fatigue life by loss of ductility leading to damage and eventually to failure by initiation and propagation of cracks. Predicting the damage due to strain accumulation and identifying the initiation and propagation of cracks is important to avoid catastrophic failure. This is usually accomplished by monitoring cyclic strain and ovality in the maximum damaged portion of the elbow. But to understand the micro-mechanisms of damage preceding crack initiation and obtain information about the cracking process, on-line monitoring of ratcheting using a suitable non-destructive testing (NDT) tool is essential. Towards this, acoustic emission (AE) is a potential technique.

Acoustic emission technique (AET) has been applied for understanding deformation and fracture processes [7-9] and for fatigue damage detection [10, 11] in different materials. Acoustic emission signals generated during fatigue can be attributed to dislocation motion, crack initiation, crack growth and ultimate failure. AE monitoring during low cycle fatigue (LCF) tests of AISI 4340 steel showed that total count of the AE signal relates to the cumulative fatigue damage and AE activity increases with strain amplitude [10]. AE along with positron spectroscopy was used to study fatigue damage in ULTIMET alloy where linear source location of AE was used to find the location of crack initiation [11].

Acoustic emission technique was used for determining crack initiation in different materials [12-15] and for detecting crack growth in pressure vessels and pipelines [16-17]. During fatigue testing of X52 pipe steel, the point of crack initiation was detected by a first significant increase in the variation of AE signal with time [12]. In C-Mn steel, the displacement point of crack initiation was described as the value of COD where significant change in slope of the total count of the AE signal vs. COD occurs [13]. During fracture toughness tests of 7075-T651 Al alloy, crack initiation was determined by the sudden change in slope of log-log plots of total count vs. stress intensity factor [14]. The hydraulic pressure test along with AE monitoring was performed on a pipe specimen of main cooling piping of a nuclear power plant, and this showed that the amplitude and energy of AE signal are correlated with the growth of the defect and give advanced warning of a potential leak in the piping [17]. AE associated with microcracking during deformation of compact tension specimens of austenitic stainless steel was reported, and this showed an increase in the frequency content of AE signals due to microcracking [18]. AET has also been used for monitoring the initiation and growth of crack during ratcheting test on

304LN stainless steel straight pipe [19]. The specimen thickness was gradually reduced from the normal section (14.75 mm) to the gauge section at the centre (12.34 mm) by machining over a distance of 250 mm on both sides and the length of the gauge section at the center was 200 mm. In another work [20], ratcheting behavior of both pipe and elbows has been compared. The straight pipes failed either by occurrence of through-wall crack accompanied by simultaneous ballooning, or bursting with simultaneous ballooning. The elbows failed by occurrence of through-wall crack accompanied by simultaneous ballooning. Ratcheting behaviour of straight pipes and elbows was compared and it was inferred that ratcheting was more pronounced in straight pipes than in elbows [20]. The ballooning and reduction in thickness values were less for elbow specimens when compared with the corresponding values for the pipe specimens [20]. This evokes interest to examine the potential of acoustic emission for the detection of damage and cracking process in elbows due to ratcheting. The novelty of the present work is thus monitoring acoustic emission during the ratcheting tests of elbows AISI type 304LN austenitic stainless steel under combined internal pressure and in-plane bending moment, and could provide useful information on the damage and deformation of the elbow and cracking process. The elbow components are used in primary heat transport system of nuclear power plants.

## 2. Experimental studies

The elbow specimens (QCE-RAT-6-L3 and QCE-RAT-6-L4 hereafter referred to as elbow 3 and elbow 4 respectively) used were made of Type 304LN stainless steel conforming to ASTM A 312/A 312 M—09 standard [21]. The specimens were obtained in the solution annealed condition. The chemical composition of 304LN stainless steel is given in Table 1. The total length of the elbow specimen was 1342 mm. The average thickness of the elbows was in the range 14.7 mm to 15.1 mm. At both the ends, the elbow was welded with end flanges. From the center of the flange weld, two threadolets were provided. Threadolet is an opening in the specimen with threads inside and a bolt is used for opening or closing. This provision was used to apply and measure the desired internal pressure.

Table 1: Chemical composition (wt.%) of Type 304 LN stainless steel

C	Mn	P	S	Si	Ni	Cr	Mo	Ti	Nb	Cu	N
0.03	1.78	0.024	0.007	0.38	9.11	18.26	0.16	0.004	0.014	0.23	0.06

The ratcheting tests were conducted at ambient temperature using a servo-controlled electrohydraulic machine with  $\pm 500$  kN capacity. Figure 1 shows the schematic of the test set-up along with locations of AE sensors. The elbows were pressurized with water, and the ratcheting test was conducted under displacement control. The frequency of loading was varied from 0.0021 Hz to 0.0125 Hz. The cyclic displacement of the two elbows was  $\pm 46$  mm and  $\pm 55$  mm respectively. Figure 2 shows the typical displacement time history for elbow 4 during the ratcheting test. For both elbows, the internal pressure was maintained at 27.6 MPa throughout the entire duration of the test. The values of minimum load and maximum load for elbow 3 were -129 kN and +150 kN respectively. Corresponding values for the other elbow were -134 kN and +159 kN. Details of ratcheting test parameters are shown in Table 2. In all the tests, the frequency of loading was varied from one cycle in 8 min (0.0021 Hz) to one cycle in 90 s (0.0111 Hz). In general, ratcheting rate is high during initial few cycles and reduces gradually with increase in the number of cycles before it gets stabilized. Hence, the tests were carried out at a very low frequency during the initial fatigue cycles and the test frequency was gradually

increased toward the end of the tests. The details of test frequency for the two elbows are shown in Table A1 in the Appendix. Further details about the specimens and the ratcheting tests can be found in the earlier papers [20, 22].

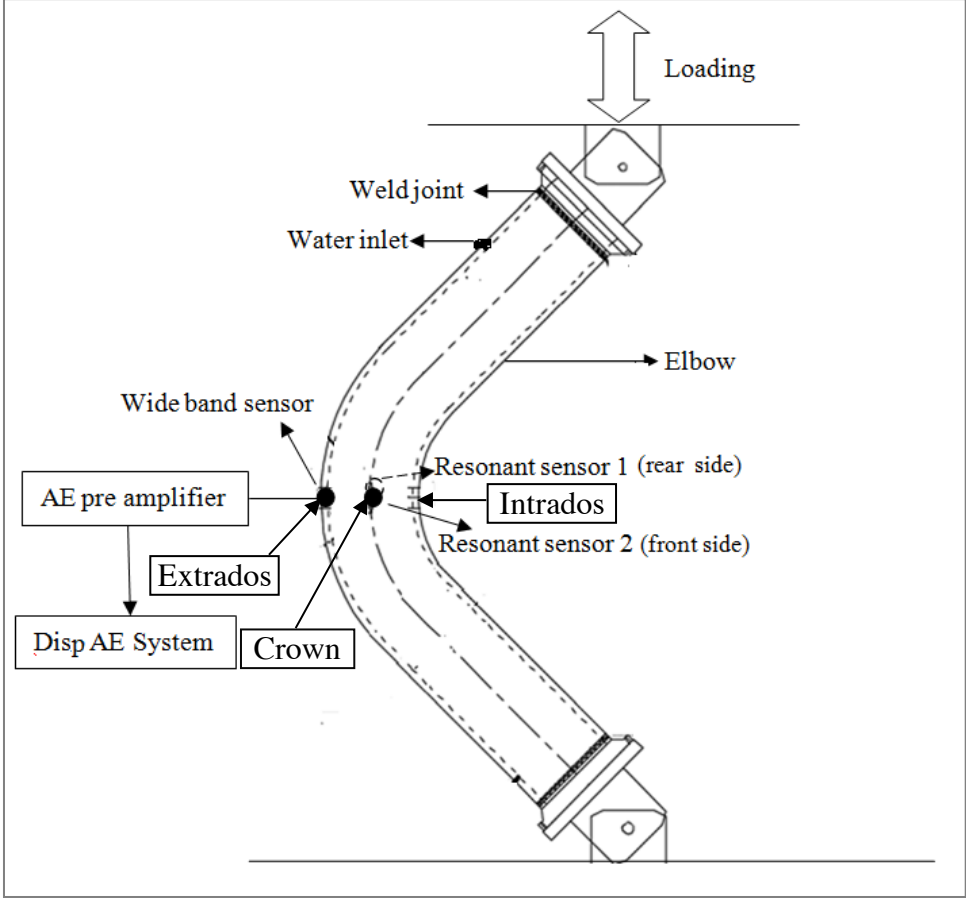


Fig. 1. Schematic of the ratcheting test set-up along with location of AE sensors.

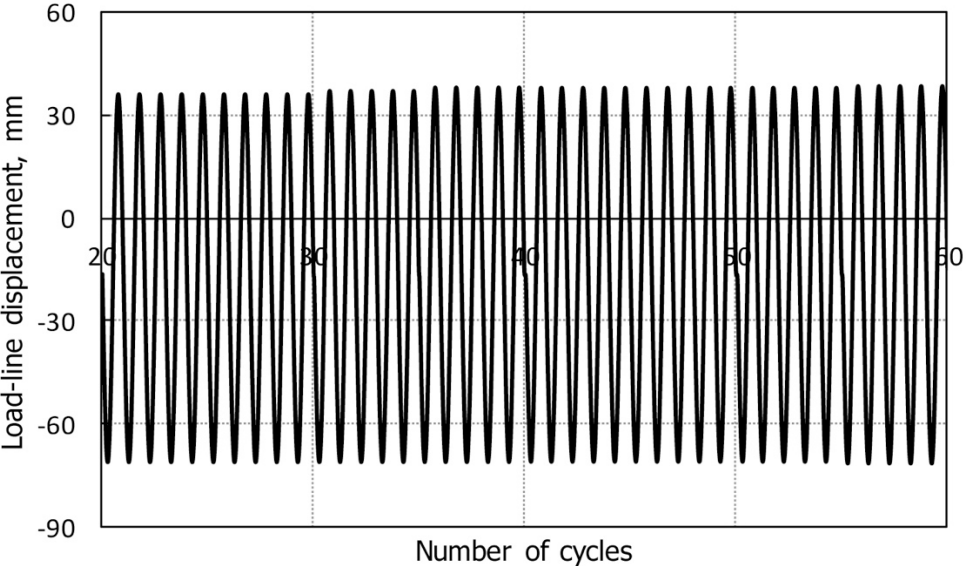


Fig. 2. Displacement history used for the elbow specimen 4. Cycles 20 to 60.

Table 2. Details of ratcheting test parameters

Specimen ID	Applied cyclic displacement (mm)	Load amplitude (kN)		Internal pressure (MPa)
		Minimum	Maximum	
QCE-RAT-6-L3	±46	-129	+150	27.6
QCE-RAT-6-L4	±55	-134	+159	27.6

Values in a cycle with maximum load range.

For the strain measurement, rosette strain gauges were mounted in the curved portion at grid locations in Intrados, Crown and Extradados. The details of the measurements can be seen elsewhere [20, 22]. The circumferential and axial lengths of the bent portion of the elbows were divided into 12 (pitch varied at 4°, 9° and 12°) and 24 (pitch varied at 10° and 20°) segments, respectively and grid lines were marked (Fig.A1 in the Appendix). The circumferential grid lines were numbered in sequence from “A” to “M”; where “A” denotes the top and “M” denotes the bottom of the bent portion. Similarly, the axial grid lines (1 to 24) were marked; where the grid lines 1 and 13 pass through the intrados and extradados respectively, and grid lines 7 and 19 pass through the two crown locations respectively. Eight three element post-yield rosette strain gauges were mounted in the bent portion at different grid locations. Four two element post-yield rosette strain gauges were mounted in the top and bottom straight portions of the elbows. In order to measure the change in the circumference at the bent portion, ovality measurements were continuously obtained using ovality set-up [20, 22]. The ovality set-up consisted of an ovality ring and four LVDTs (linear variable differential transformers). LVDTs were arranged diametrically opposite to each other along the circumference of the elbow. Bend clip was used to measure the increase in diameter. The bend clip consisted of two steel plates. Two strain gauges were fixed on each of these plates. This arrangement was used to record ovalization by taking average of the measured strains. One LVDT was fixed to measure vertical displacement of the elbow. The applied load and load-line displacement were obtained directly through the in-built load-cell and LVDT in the actuator. Circumferential length of the specimen in the bent portion was also measured along all the circumferential grid lines and percentage of ballooning was obtained as an increase in circumferential length at various grid lines.

Acoustic emission signals generated during the ratcheting tests were recorded using AE DiSP system. In this work, two piezoelectric resonant sensors with 150 kHz frequency each were mounted on the crown of the elbows (placed at diametrically opposite point on the elbows). Position of the resonant sensors are marked as “resonant sensor 1 (rear side)” and “resonant sensor 2 (front side)” in Fig. 1. For the two resonant sensors, preamplifiers (40 dB gain) and band pass filters (100 - 300 kHz) were used to record the AE signals. The threshold for the resonant sensors was 40 dB<sub>AE</sub>, and all amplitudes reported are in dB<sub>AE</sub>, even when not so labeled. In order to ensure that no noise is recorded from the grip region, a dummy specimen was subjected to repeated fatigue cycling at higher load levels before the actual testing with simultaneous recording of AE signals. The dummy specimen was of the same geometry and dimensions as that of the actual specimens used, i.e. total length 1342 mm and average thickness in the range 14.7 mm to 15.1 mm. This dummy specimen experienced potential rotation at the pins in the same way as the test elbows. During the test of the dummy sample, the gain and threshold of the resonant sensors were as reported above. The values of peak definition time (PDT), hit definition time (HDT) and hit lockout time (HLT) chosen were 200 μs, 800 μs and 1000 μs respectively. To study the frequency characteristics of AE signal, a broadband piezoelectric sensor (100 kHz - 1 MHz) with integrated preamplifier (gain 40 dB) was mounted on the extradados (at the bend region) (Fig. 1). The threshold of the broadband piezoelectric sensor

was maintained at 40 dB<sub>AE</sub>. For waveform recording, the hit length selected was 15 k and sampling rate was 5 MSPS. Pretrigger value given was zero. The signals recorded by the broadband sensor were digitized. Silicon grease was used as the couplant and all the sensors were mounted using adhesive tape.

The coupling and sensitivity of the sensors before the tests were checked by simulating with pencil lead break test in the central region of the elbows. The pencil lead break is considered to be a repeatable event that produces a stress wave similar to the stress waves normally generated during a dynamic event like crack growth. The simulation was done with pressure inside the elbow specimen. The amplified and filtered signal is passed to the A/D converter where the AE signal is digitized at rates up to 4 MHz. The digitized signal is passed to the feature extraction circuitry. The high-speed feature extracted data is then further processed by the signal processor. The resultant signals captured by two resonant sensors were used. Different parameters of the AE signal such as root mean square (RMS) voltage, AE counts, energy, cumulative count, cumulative energy and peak amplitude (PA) for the two resonant sensors and frequency spectra for the broadband sensor were used for analyzing the results. RMS averaging time was carried out at 500 milliseconds. Displacement was the parameter input to the AE measurement system.

### 3. Results and discussion

Both the specimens showed significant ratcheting in the circumferential direction at crown and intrados locations. Ratcheting was indicated by gradual accumulation of strain with increased loading cycles. The ovality of the elbow gradually increased with increase in the number of cycles. At the cycles of 282 and 133 for elbow 3 and elbow 4 respectively, through-wall cracks appeared, and the cracks were accompanied by ratchet swelling, i.e., ballooning. The cracks appeared in the bent portion at one of the crown locations in both the specimens. The appearance of through-wall crack was indicated by a sharp water jet.

The cyclic displacement applied during ratcheting test on elbow 3 was  $\pm 46$  mm. In the case of elbow 4, the cyclic displacement during ratcheting test was  $\pm 55$  mm. Figure 3 shows typical strain variation for elbow 4. The notations 'G1' and 'G7' represent the locations of rosette strain gauges and 'A', 'B' and 'C' represent the directions of strain measurement, viz., A: axial, B: 45° and C: circumferential. The strain gauges bonded at critical locations failed after completion of a few cycles and hence the strain data could not be acquired till the end of the tests at these locations. Since, the gauges at different locations failed at different cycles, the strain data is not the same for each gauge position.

The result from the dummy specimen is shown as the variations of (a) AE counts and (b) AE energy vs. time up to 10 cycles in Figs. 4a and 4b. It is seen that at the selected gain and threshold, a minimal number of hits were recorded. The selected gain and threshold values were used for the actual tests. However, AE was monitored during the cyclic tests of the elbows and AE was not monitored during the pressurization.

Variations of AE RMS voltage, AE counts, and cumulative counts, and AE energy and cumulative energy as a function of the number of cycles for elbow 3 (which failed at 282 cycles) are shown in Fig. 5. Similar variations for elbow 4 (which failed at 133 cycles) are shown in Fig. 6. The results in Figs. 5 and 6 are from the two resonant sensors. It is seen that AE signals are generated constantly from the beginning of the tests in both elbows. AE cumulative counts and cumulative energy increased with an increase in the number of cycles. The first significant

increase in AE signal (RMS voltage, counts, and energy) was observed at 214 cycles for elbow 3 and 103 cycles for elbow 4 (shown by arrows in Fig. 5 and Fig. 6). The nature of the cumulative count and cumulative energy plots also changes and goes to a higher value around these cycles. AE generated in both the elbows were very high beyond these cycles, and continued up to failure.

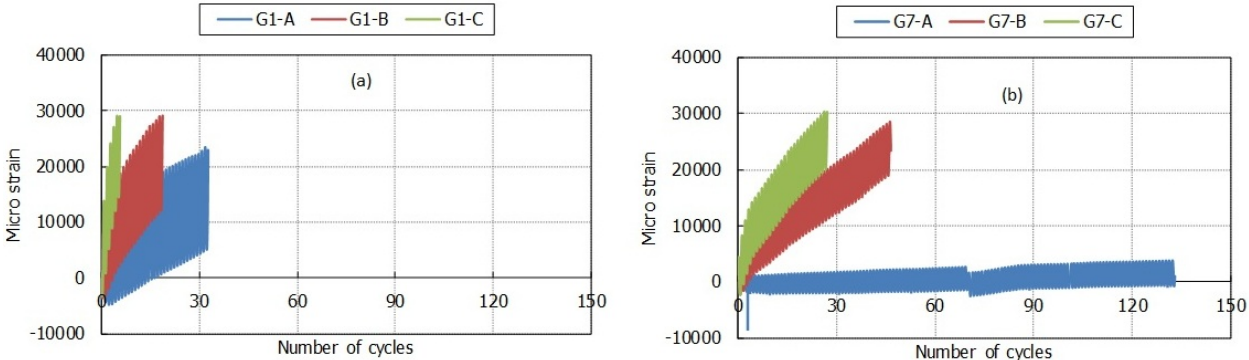


Fig. 3. Strain variation in elbow 4.

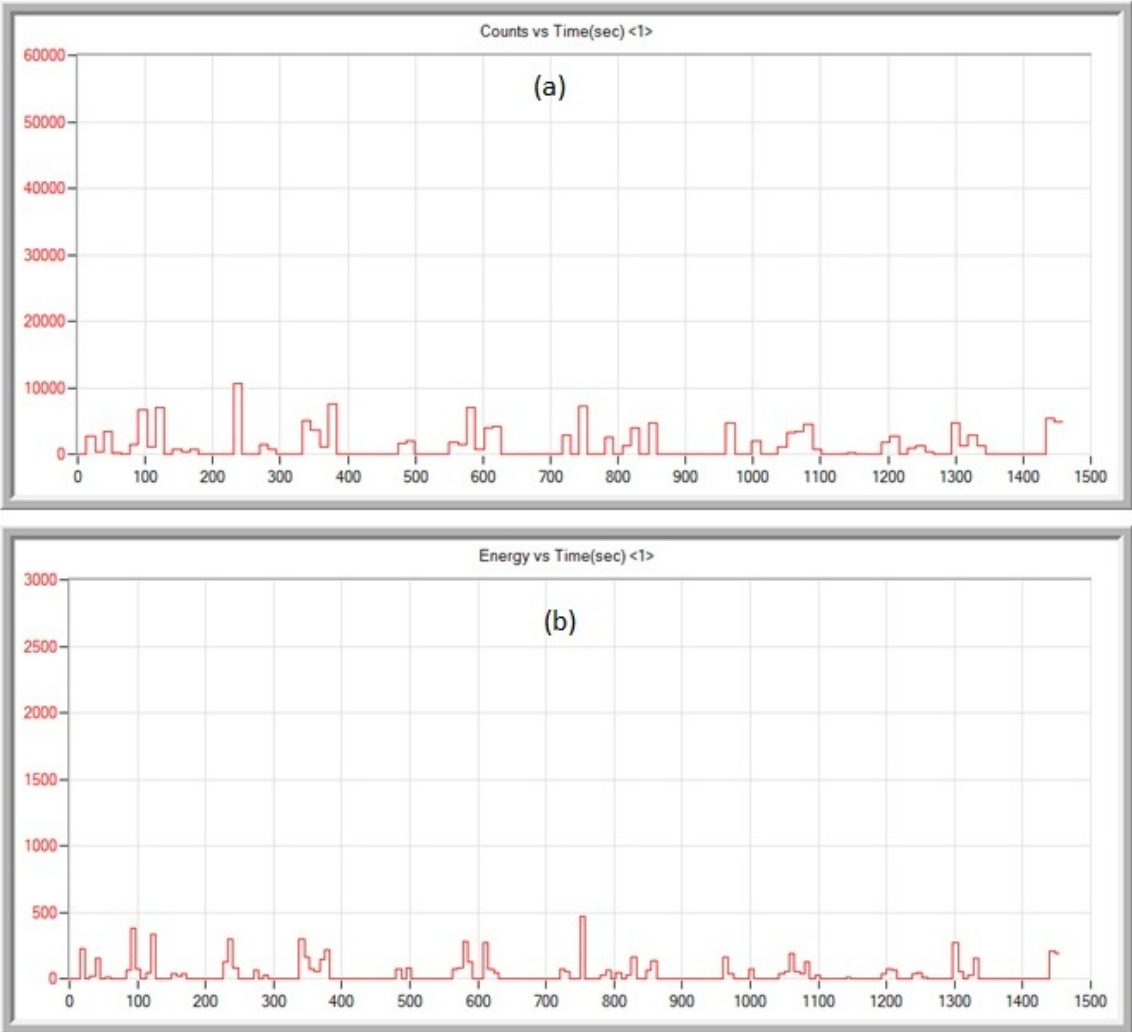


Fig. 4. Variation of (a) AE counts and (b) AE energy vs. time for the dummy specimen up to 10 cycles.

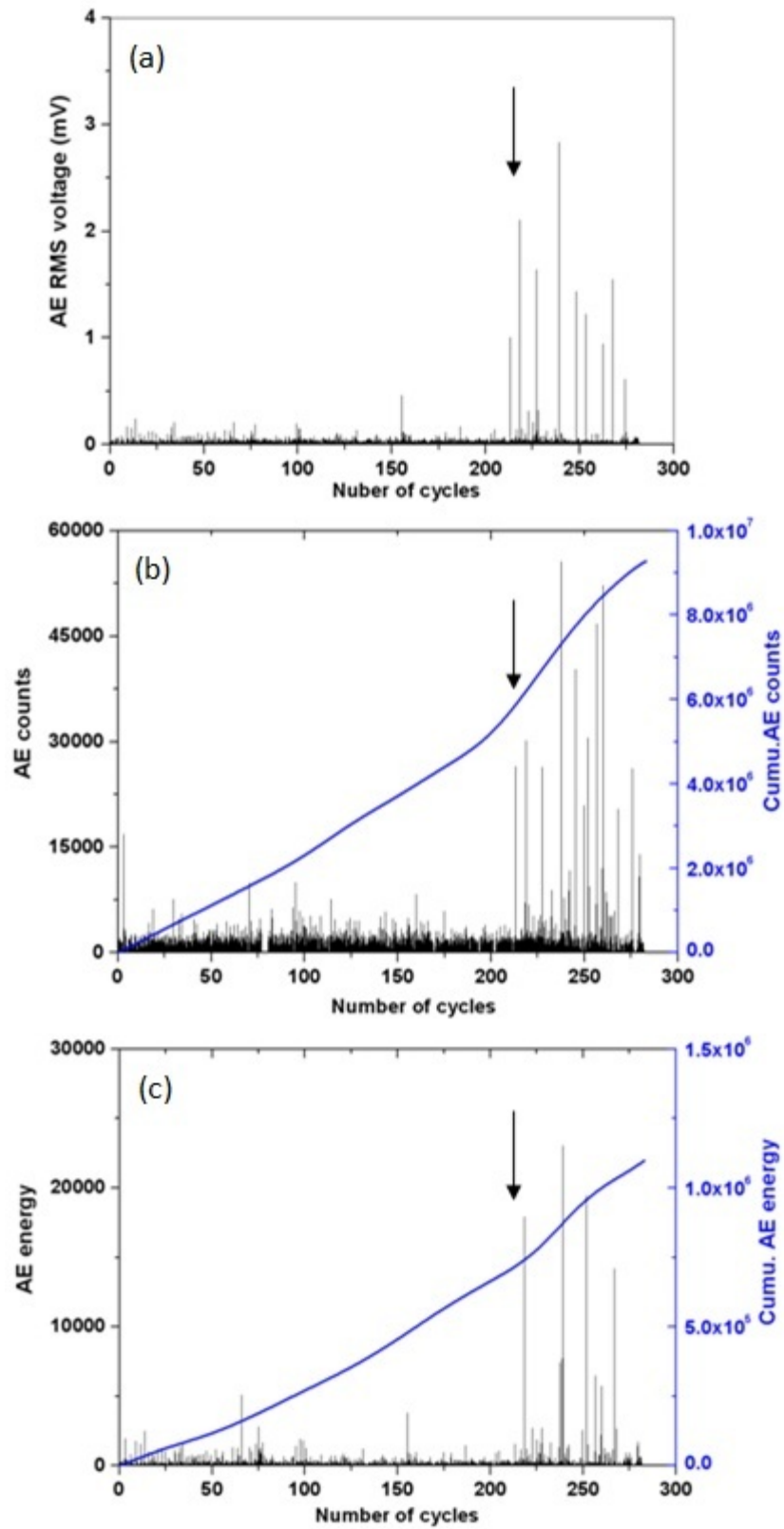


Fig. 5. Variation of (a) AE RMS voltage, (b) AE counts and cumulative count, and (c) AE energy and cumulative energy as a function of number of cycles for elbow 3 (failed at 282 cycles)

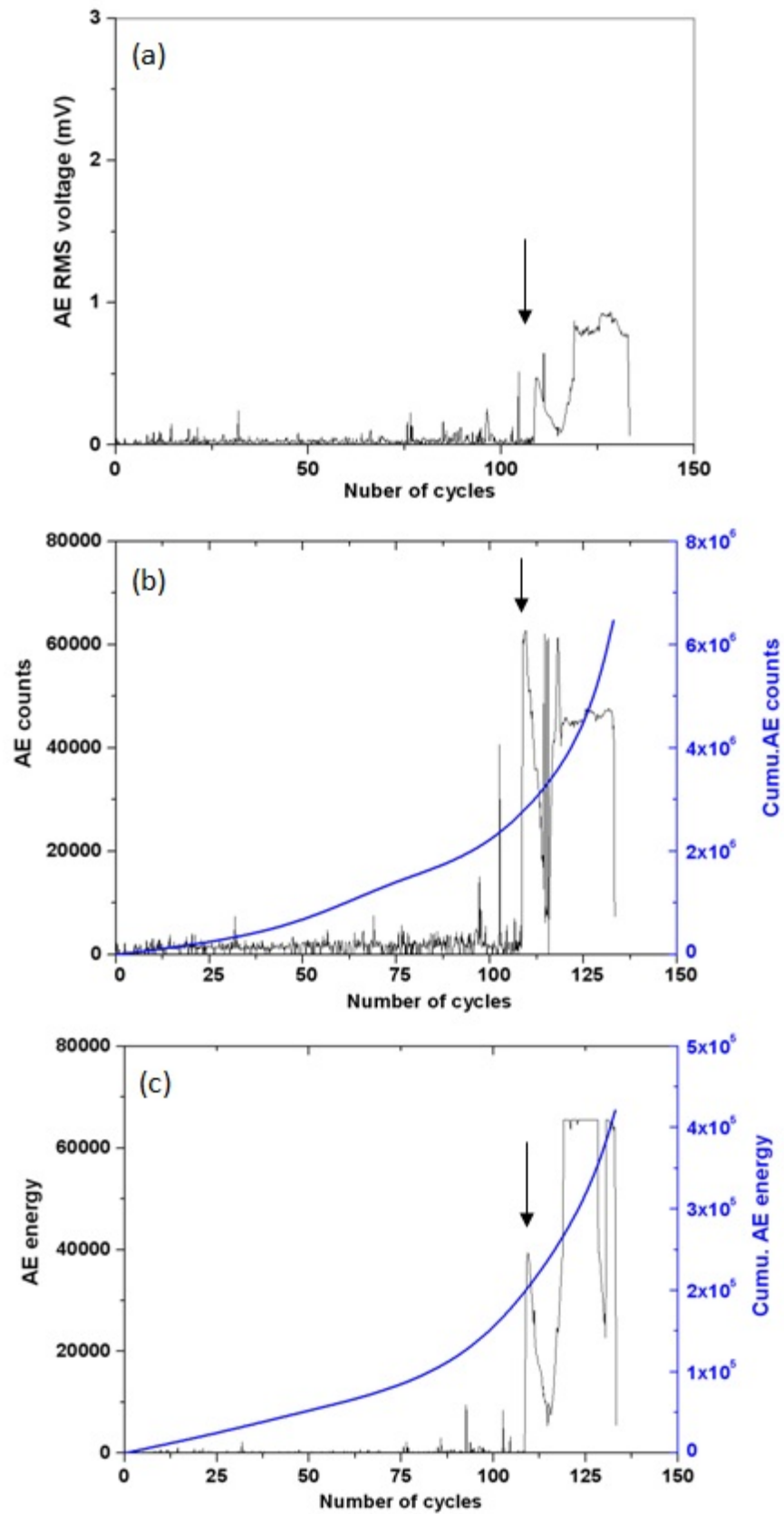


Fig. 6. Variation of (a) AE RMS voltage, (b) AE counts and cumulative count, and (c) AE energy and cumulative energy as a function of number of cycles for elbow 4 (failed at 133 cycles).

Generation of acoustic emission for understanding deformation and fracture processes in austenitic materials is known [7-9]. AE due to damage processes is also generated during fatigue cycling [10, 11]. During ratcheting tests of the elbow specimens, AE is generated continuously from the beginning of the tests, and this is attributed to the occurrence of damage in the material due to simultaneous application of internal pressure and fatigue cycling. Ratcheting studies of different materials reported earlier in the literature showed increased damage processes with increasing number of cycles. In the present study, it was observed that ovality of the elbows gradually increases with increase in the cycles and ratcheting is significant in the circumferential direction.

The distribution of AE hits (events) by peak amplitude for different cycles for the two elbows is shown in Figs. 7 and 8. It is seen from these figures that up to 210 cycles for elbow 3 and up to 100 cycles for elbow 4, hits generated are up to around 75 dB and 65 dB amplitude respectively. But for 211-220 cycles for elbow 3 and for 101-110 cycles for elbow 4, where a first significant increase in AE was noted, higher amplitude signals (>75 dB for elbow 3 and >65 dB for elbow 4) are also generated in addition to the hits generated up to 75 dB and 65 dB. Beyond these cycles also (> 220 cycles for elbow 3 and > 111 cycles for elbow 4), higher amplitude signals are generated in addition to lower amplitude signals. The generation of AE due to deformation during tensile testing in austenitic alloys is characterized by lower peak amplitude events [7]. The first significant increase in AE (RMS voltage, counts and energy) and the appearance of events with higher peak amplitudes around 214 cycles and 103 cycles for the two elbows can be attributed to the process of crack initiation. The first significant increase in the variation of AE with time was used to detect crack initiation during fatigue testing of X52 pipe steel [12]. High amplitude AE events during crack initiation are known to occur by rapid shear linkage of growing voids and reported in the case of A533 pressure vessel steel [13]. During fracture toughness test of 7075-T651 Al alloy, crack initiation was determined by sudden change in slope of log-log plots of total count vs. stress intensity factor and high amplitude AE signals [14]. In ratcheting test on 304LN stainless steel straight pipe [19], generation of higher AE and events with higher peak amplitudes accompanied by AE cluster formation in a localized region between 826-845 cycles revealed the initiation of crack. The crack initiation detected by AET was much before than final rupture of the pipe (1203 and 1225 cycles for two fatigue cracks), which showed the unique potential of acoustic emission technique for the detection of initiation and growth of fatigue cracks during ratcheting test in pipe specimens [19]. Continued generation of AE signals beyond 214 cycles for elbow 3 and 103 cycles for elbow 4 in this study can be attributed to crack growth which emits higher amplitude signals.

The AE waveforms captured by the broadband sensor were studied for frequency spectrum analysis. Applied cyclic displacements of ratchetting are  $\pm 46$  mm and  $\pm 55$  mm for elbow 3 and elbow 4 respectively. All AE waveforms used for analysis in each cycle are selected from peak displacement point (either positive or negative load) of corresponding cycle. For elbow 3, successive five waveforms at  $\pm 46$  mm displacement position and for elbow 4 successive five waveforms at  $\pm 55$  mm displacement position of corresponding cycles have been used. The number of waveforms recorded for different cycle ranges for the two elbows are given in Table 3. One set of waveforms for different cycles for elbow 3 is shown in Figs. 9 and 10. Similarly one set of waveforms for different cycles for elbow 4 is shown in Figs. 11-12. FFT results show amplitude below the 100 kHz. This can be understood in the light of the fact that frictional noise is generally of low frequency. Continuous type waveforms with multiple bursts are observed during initial loading cycles of both elbows 3 and 4. Types of AE waveforms are different during probable crack initiation cycles (cycle 214 of elbow 3 and cycle 103 of elbow 4). In these cycles,

bursts are dominant at the initial portion of the waveform as shown by arrows in Figs. 10 and 11. During crack propagation cycles, again continuous type waveforms with multiple bursts are present throughout the waveforms.

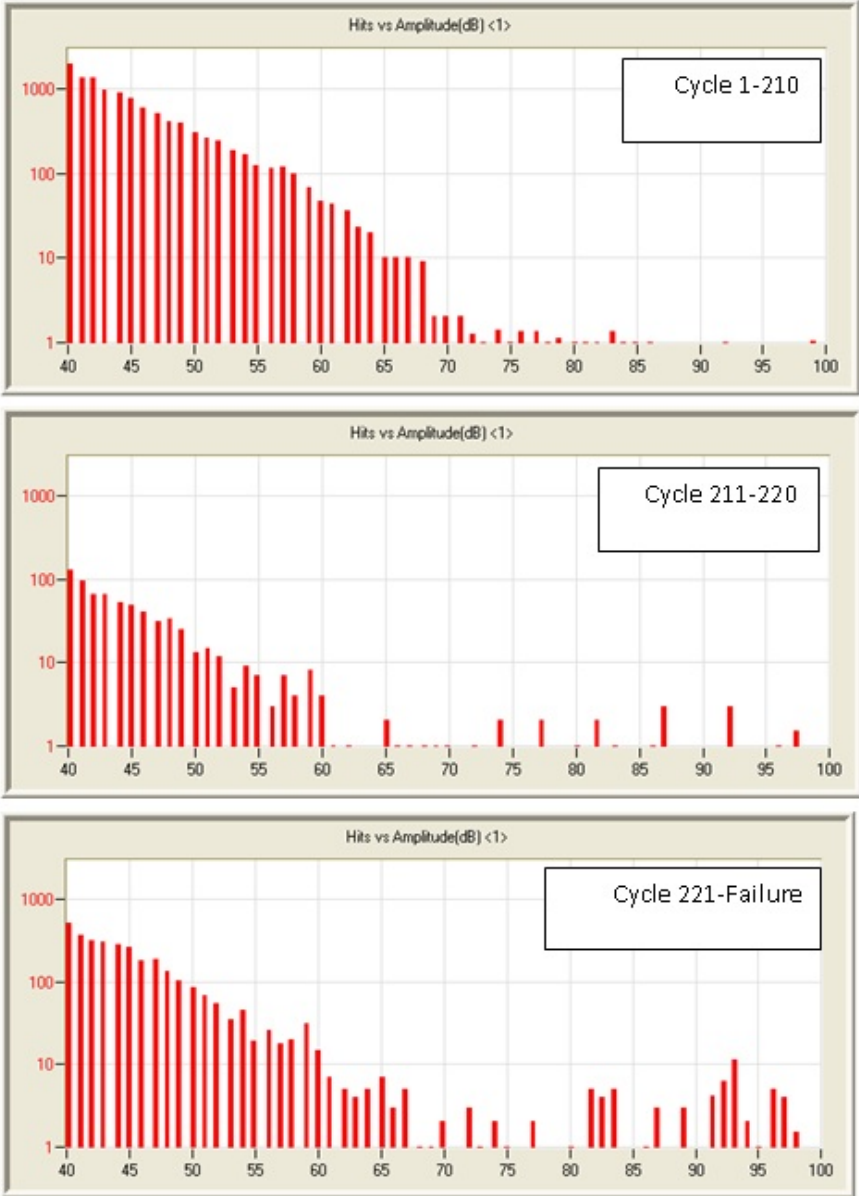


Fig. 7. Distribution of AE hits (events) by peak amplitude for different cycles of elbow 3.

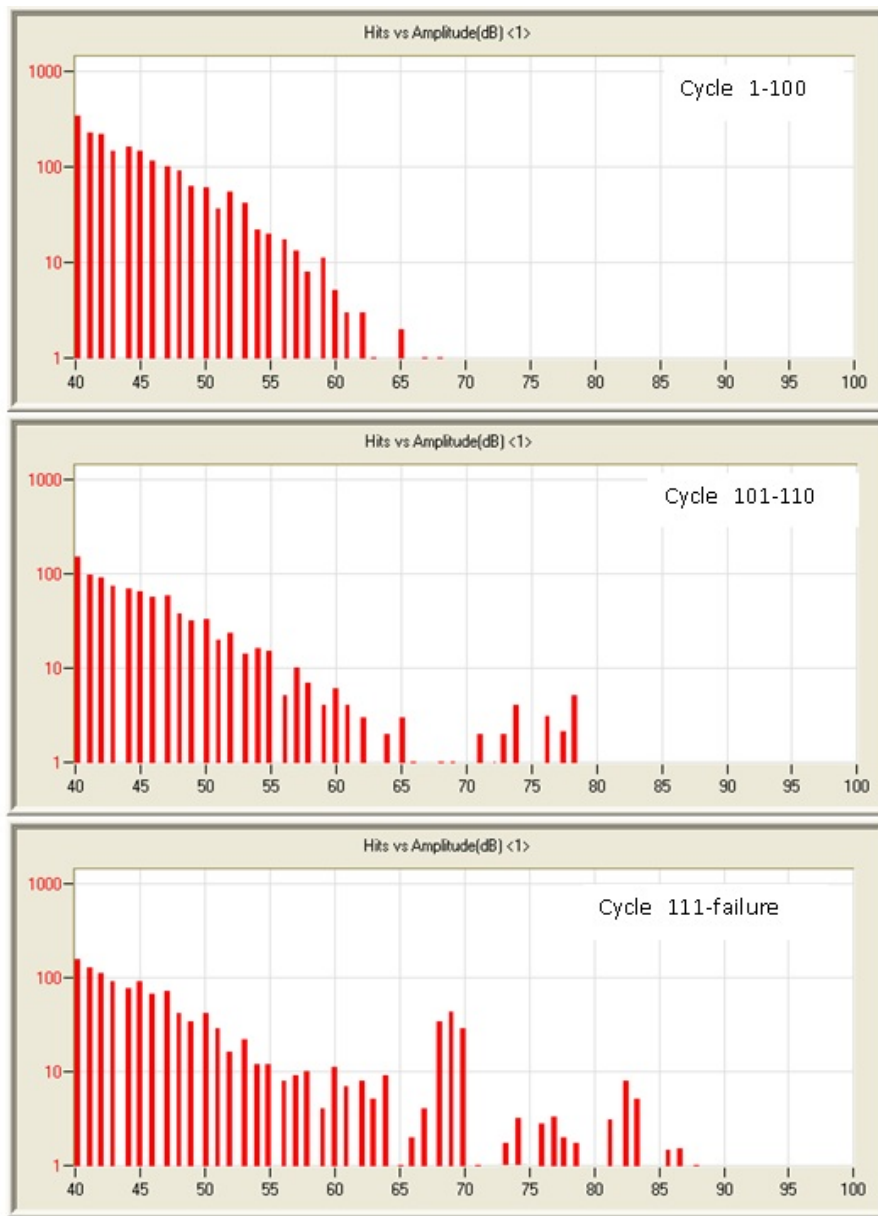


Fig. 8 Distribution of AE hits (events) by peak amplitude for different cycles of elbow 4

Table 3. Number of waveforms recorded for different cycle ranges for the two elbows.

Elbow 3		Elbow 4	
Cycle No.	No. of waveforms recorded	Cycle No.	No. of waveforms recorded
40-50	190	10-15	236
140-150	213	50-60	250
190-200	235	100-110	240
210-220	267	120-135	720
250-260	380	120-135 (rupture)	720
270-282 (rupture)	607		

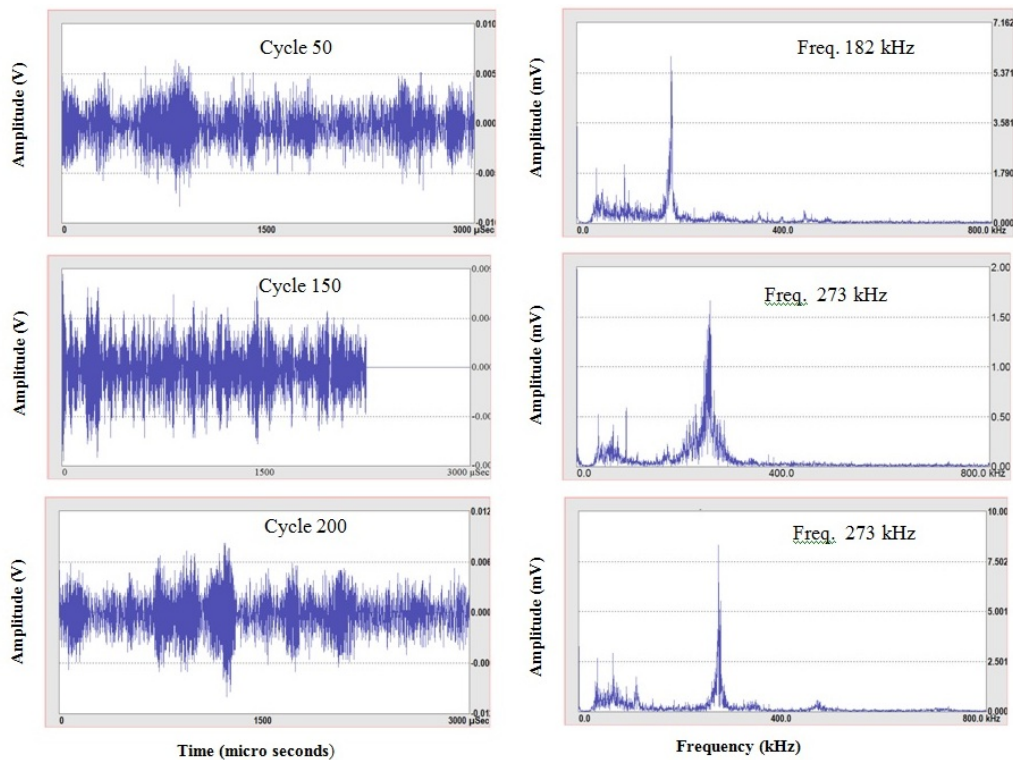


Fig. 9. AE waveforms and frequency spectra generated during various fatigue cycles (50, 150 and 200) of elbow 3.

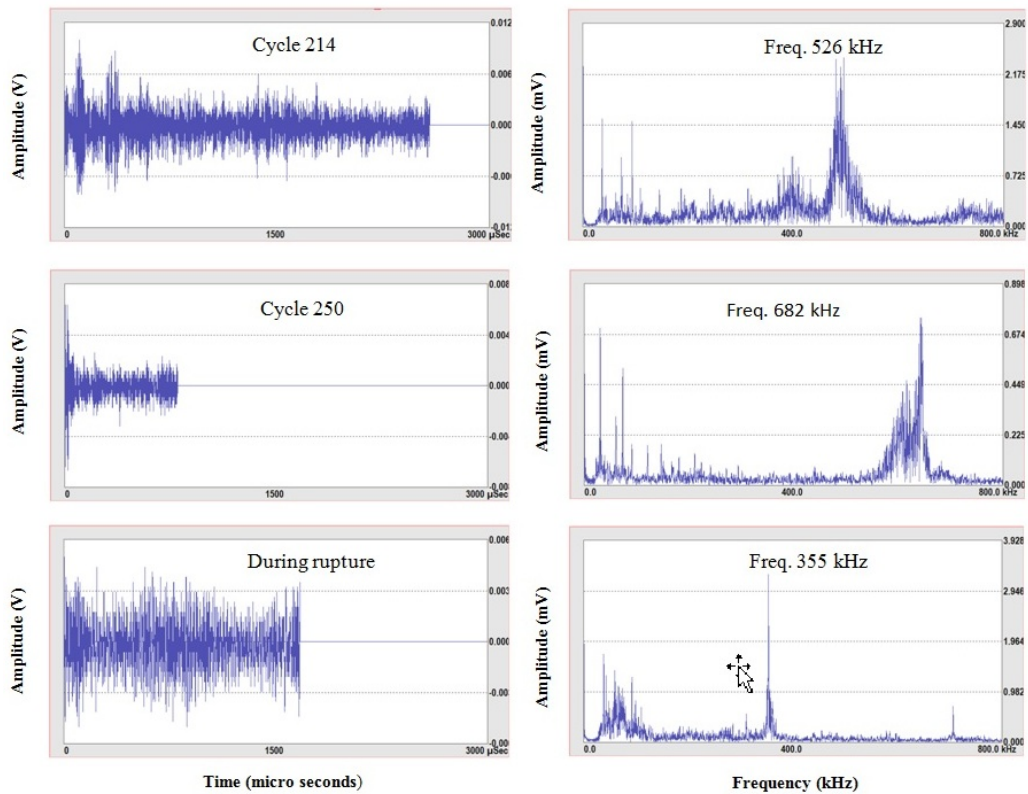


Fig. 10. AE waveforms and frequency spectra generated during various fatigue cycles (214, 250 and during rupture) of elbow 3.

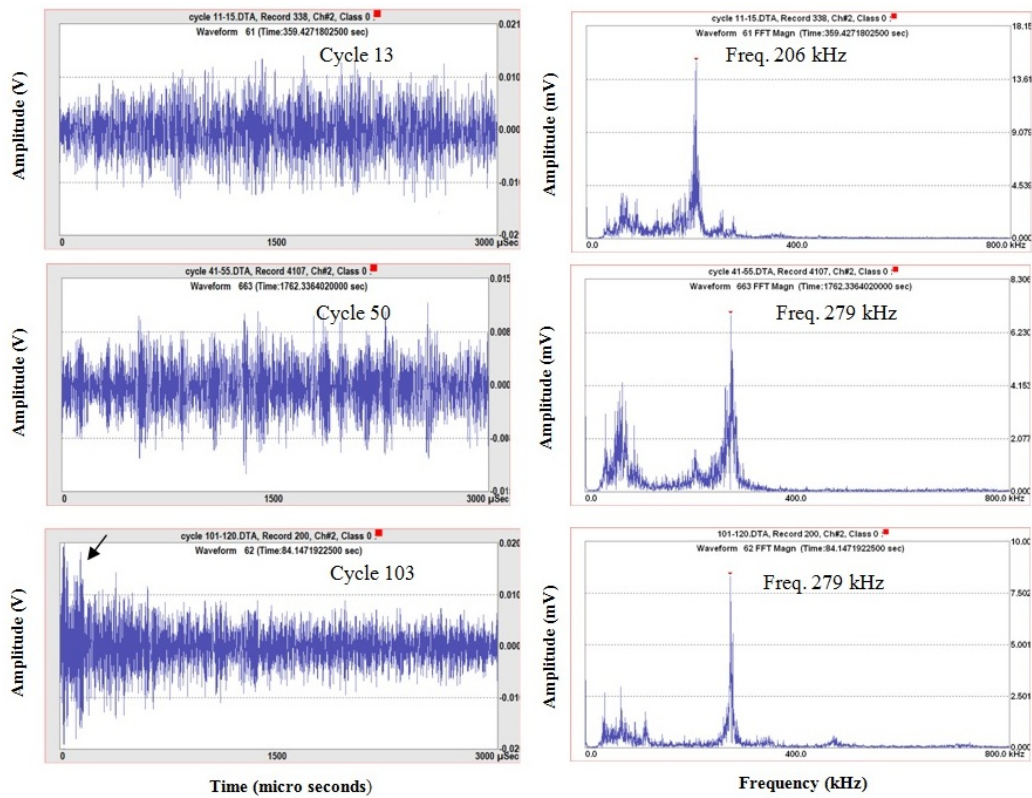


Fig. 11. AE waveforms and frequency spectra generated during various fatigue cycles (13, 50 and 103) of elbow 4.

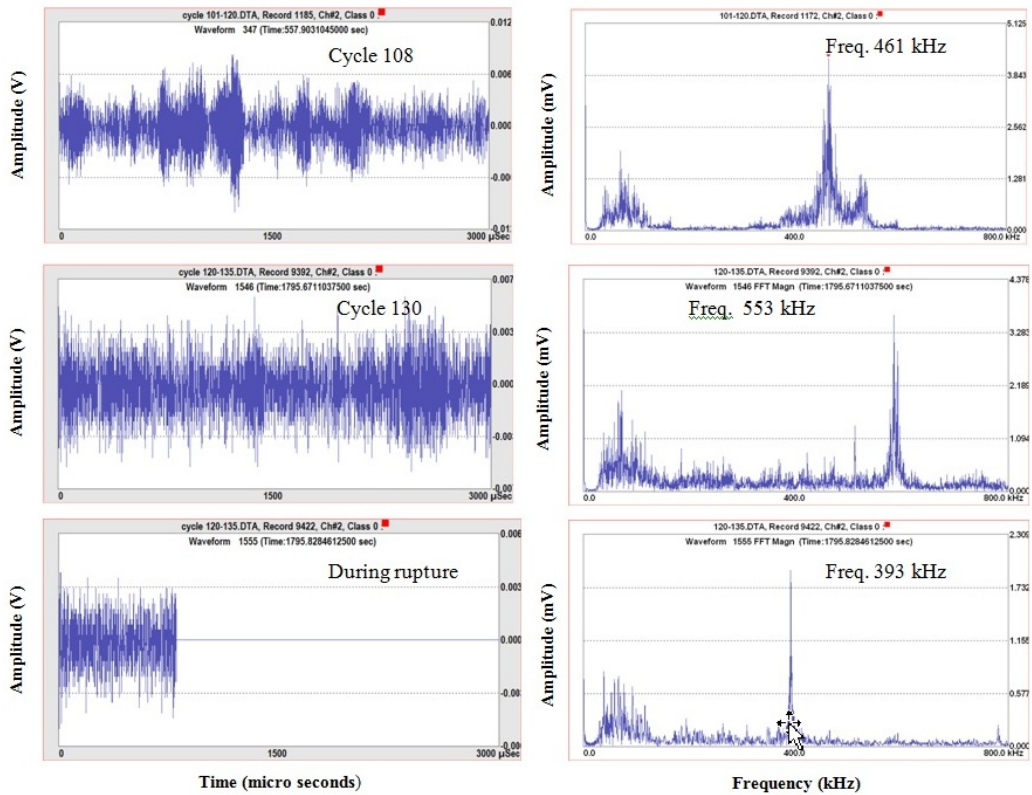


Fig. 12. AE waveforms and frequency spectra generated during various fatigue cycles (108, 130 and during rupture) of elbow 4.

FFT analysis of the waveforms was carried out to extract the frequency of the signals which are also shown in Figs. 9-12. The variation in statistics from multiple events generated in the same cycles has been studied. The results are given in Tables 4a and b. The statistics in these tables are based on multiple events for the different cycle numbers shown. Load ranges corresponding to the fatigue cycles and waveform numbers used to create the statistical results are also shown in Tables 4a and 4b. The load ranges in Tables 4a and b are the difference between maximum load (Pmax) and minimum load (Pmin), i.e., Pmax - Pmin in the specified cycle, which the elbow experienced corresponding to the applied load-line displacement. The average (mean) values of the dominant frequencies of AE signals for different cycles for the two elbows are shown. The values of standard deviation (Sd) and 95% confidence interval (CIL and CIU) associated with the average values of the dominant frequency for different cycles are also shown in Table 4a-4b. It is seen that dominant frequency increases with fatigue cycles for both the elbows. For elbow 3, the average dominant frequency increases from 192 kHz (at 50 cycles) to 554 kHz (at 214 cycle, i.e., probable crack initiation detected by AE) and to 700 kHz (250 cycles). For elbow 4, the average dominant frequency increases from 218 kHz (at 13 cycles) to 278 kHz (at 103 cycle, i.e., probable crack initiation detected by AE) and to 518 kHz (at 130 cycles). During final rupture, the average dominant frequency shifts to a lower frequency (368 kHz for elbow 3 and 408 kHz for elbow 4). Whenever there is a change in AE source mechanism, rise time (not the rise time measured by the AE system) of the source function can change and this leads to change in the dominant frequency of the AE signal. The study of acoustic emission generation during tensile deformation of nuclear grade AISI type 316 stainless steel has shown that the frequency of the AE signal increases with increasing strain [7]. In the case of elbows in the present study, with increasing the number of cycles, in addition to deformation and crack initiation, growth of a crack also takes place. Crack growth may produce signals with higher frequency content. The increase in the dominant frequency with increasing cycles can thus be associated with an increase in strain due to deformation and cracking phenomena. Increase in the frequency of AE signals due to microcracking has been reported during deformation of compact tension specimens of austenitic stainless steel and this explains the higher frequency signals generated before rupture [18]. The lower predominant frequency during rupture can be associated with the occurrence of fracture in a ductile manner [23].

Table 4a: Load range, dominant frequency range, waveform No. and statistical results for different cycles of elbow 3.

Fatigue cycle No.	Load range (kN)	Frequency range (kHz)	Waveform No.	Mean (kHz)	Sd (kHz)	CIL (kHz)	CIU (kHz)
50	275.6	182-203	172, 175, 180, 185, 190	192	11	166	218
150	272.8	273-300	195,198, 205, 210, 213	285	14	250	319
200	270.6	273-315	217, 220, 225,230, 235	293	21	241	346
214	270.2	526-571	114, 120, 124, 131, 139	554	24	493	615
250	267.2	682-722	3, 10, 20, 25, 30	700	20	651	751
Rupture		355-387	550, 560, 570, 580, 600	368	17	325	410

Table 4b: Load range, dominant frequency range, waveform No. and statistical results for different cycles of elbow 4.

Fatigue cycle No.	Load range (kN)	Frequency range (kHz)	Waveform No.	Mean (kHz)	Sd (kHz)	CIL (kHz)	CIU (kHz)
13	291.9	206-225	61, 81, 100, 123, 135	218	11	192	245
50	289.8	279-309	3, 14, 22, 32, 37	291	16	252	330
103	290.6	270-290	62, 77, 91, 100, 105	278	11	251	304
108	290.8	461-497	187, 192, 197, 201, 205	477	18	431	523
130	287.6	490-553	411, 419, 427, 428, 435	518	32	438	598
Rupture		393-421	600, 630, 650, 670, 680	408	14	373	444

Wavelet analysis of AE waveforms generated during different cycles has been carried out. Wavelet analysis was carried out using AGU-Vallen freeware software program. This software program uses Gabor wavelet as mother wavelet. Ten kHz frequency resolution and 200 samples wavelet size are used to obtain sufficient resolution of the wavelet transform. The results from one of the elbows (elbow 4) are shown here. Figures 13a-13c show wavelet coefficients of AE waveforms generated during different cycles of 13, 103 and 130 of elbow 4. Figure 13a shows wavelet coefficients of AE waveform generated during 13th cycle of loading. This shows that during the initial loading cycle, multiple peaks are active throughout the signal around the frequency 200 kHz and it is attributed to the deformation process. During 103th cycle (probable crack initiation region detected by AE), wavelet shows a single dominant peak around 270 kHz with high wavelet coefficient amplitude. It shows the considerable difference from initial loading cycles, and it is clear that dominant frequency component is active only during the initial portion of the signal as shown by the arrow in Fig. 13b. Wavelet coefficients of AE signals at 130th cycle of loading (final stage of loading) are given in Fig 13c. Wavelet coefficient shows that two dominant peaks around 80 and 530 kHz are active during the final stage of loading. Wavelet shows a shift of dominant frequency from 270 kHz to around 530 kHz from the probable crack initiation region to crack propagation. Formation of higher dominant frequency during the final stage of loading is due to faster crack growth, and it results in high energy release. Second lower dominant frequency around 80 kHz in the wavelet plot (Fig. 13c) is absent in the FFT results, and it is active throughout signals with multiple peaks as shown in Fig 13c. AE frequency peak around 80 kHz throughout the signal could be due to minute leaks during the final region of loading which generates continuous signals. AE signals generated during leaks are continuous type. The continuous wave is a summation of multiple waves with the same or different frequency but with a different rise, arrival and decay time [24].

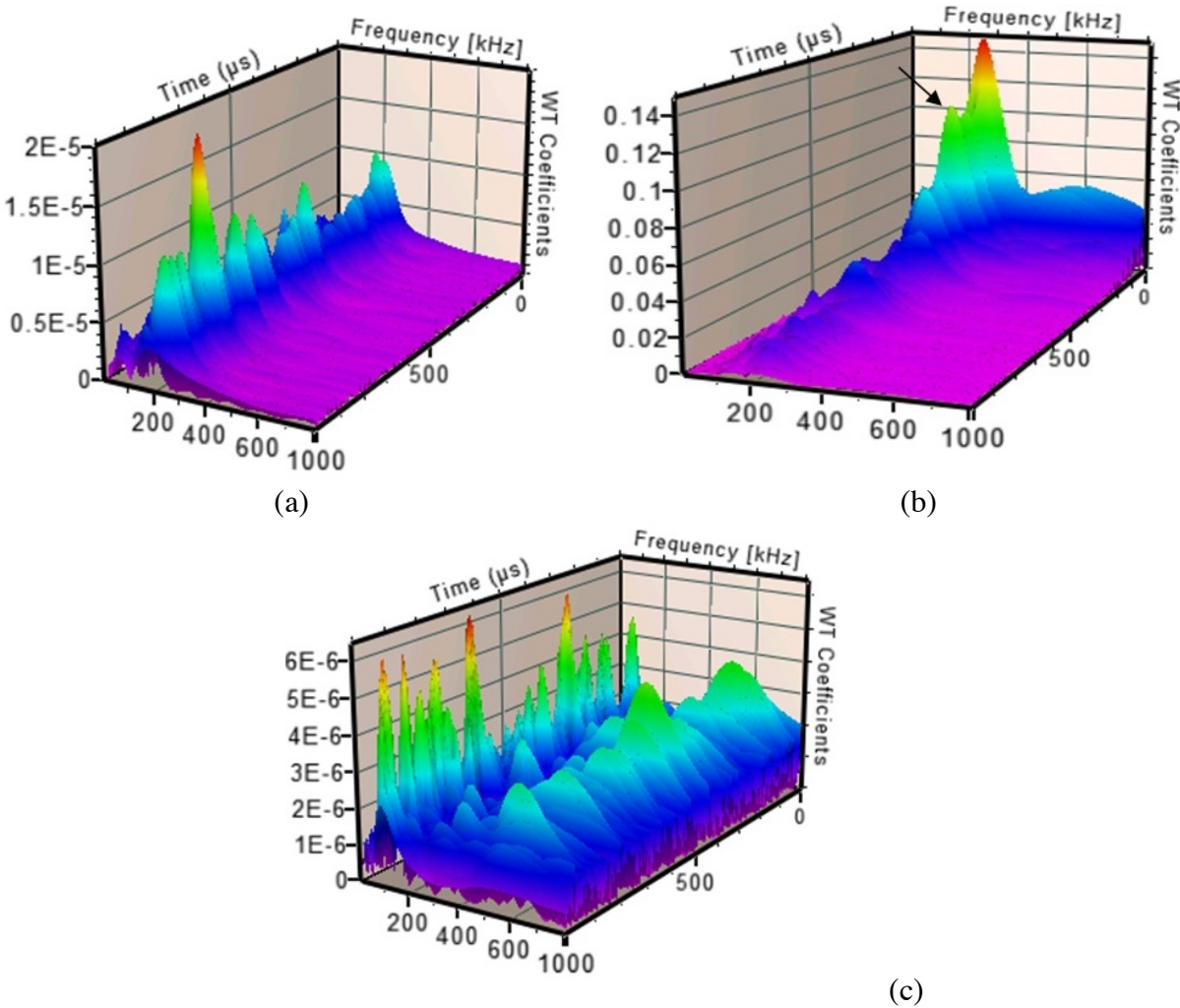


Fig. 13(a) Wavelet coefficient of AE signal generated during cycle 13. (b) Wavelet coefficient of AE signal generated during cycle 103. (c) Wavelet coefficient of AE signal generated during cycle 130.

The variation of circumferential strain and % ballooning as a function of fatigue cycles for the two elbows are plotted in Figs. 14a and 14b. Ballooning or ratchet swelling was measured as an increase in circumferential length. Comparison of Figs. 14a, b with Figs. 5, 6 shows that while the increase in circumferential strain and ballooning shows saturation tendency with the number of cycles, AE cumulative count, and cumulative energy increases continuously. This can be attributed to the generation of acoustic emission due to crack growth in addition to that generated by the circumferential change in strain. The saturation of circumferential strain and ballooning is shown more clearly in Figs. 15a, b where circumferential strain rate and ballooning rate are plotted with a number of cycles. These were determined by differentiating circumferential strain and % ballooning respectively, with respect to fatigue cycles. Ratcheting strain rate in a ratcheting test refers to the increment of ratcheting strain in each cycle [4]. The ratcheting strain in the present study was measured by using rosette strain gauges mounted in the curved portion at grid locations in Intrados, Crown and Extrados. This shows that the circumferential strain rate and ballooning rate decreases rapidly up to around 65-70 cycles for both the elbows, and after that decreases slowly. This is due to decrease in the rate of ovalization beyond 65-70 cycles. The decrease in ratcheting rate with increasing fatigue cycles is known [4]. However, AE is generated continuously during the ratcheting test and indicates the occurrence of damage, and the cracking

process. Figures 14 and 15 also show that circumferential strain and strain rate and % ballooning and ballooning rate are higher for elbow 4 as compared to elbow 3 resulting in early crack initiation and rupture. This is due to higher amount of damage by cyclic displacement, i.e., bending load for elbow 4.

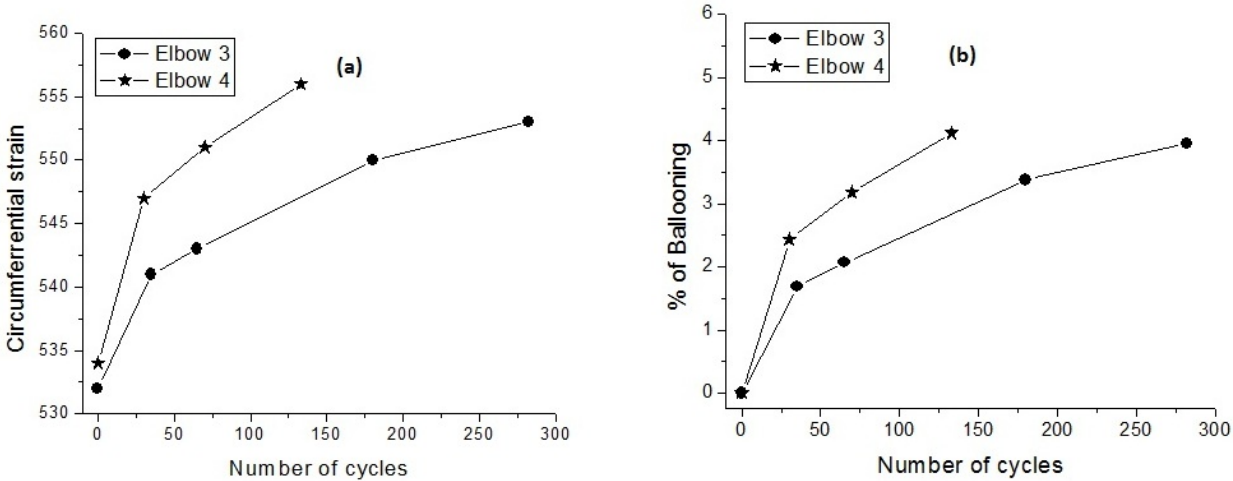


Fig. 14(a). Circumferential strain vs. number of cycles. (b) % of ballooning vs. number of cycles.

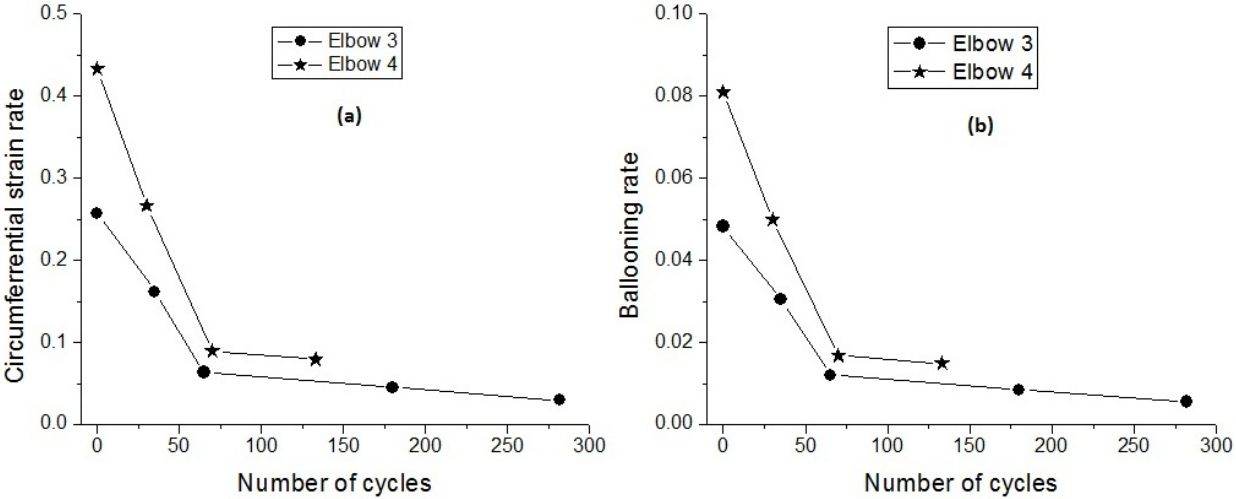


Fig. 15 (a) Circumferential strain rate vs. number of cycles. (b) Ballooning rate vs. number of cycles.

It can thus be concluded that the first significant increase in AE at around 214th cycle for elbow 3 and 103rd cycle for elbow 4, which is 76% and 77% of the total cycle up to failure, can be attributed to crack initiation and is much before their final rupture. Significant AE is generated beyond these cycles, and this can be attributed to crack growth.

**4. Conclusions**

- Acoustic emission (AE) signals generated during ratcheting tests of two elbows made of AISI type 304LN stainless steel were monitored. AE generated during the ratcheting tests has been attributed to cracking caused by simultaneous application of internal pressure and

fatigue cycling.

- The first significant increase in AE at around 214 cycles and 103 cycles which are 76% and 77% of the total cycle up to failure, has been attributed to crack initiation in the two elbows. Beyond these cycles, generation of higher acoustic emission activity and also the generation of higher amplitude signals are attributed to crack propagation.
- With increasing the number of cycles, frequency of the signal increases while rupture of the elbows produced signals with lower frequency.
- AE signals due to deformation in early loading cycles are characterized by wavelet coefficients of multiple peaks whereas AE signals generated during probable crack initiation cycle are characterized by a single peak of higher wavelet coefficient amplitude.

### **Acknowledgement**

Authors are thankful to Dr. A.K. Bhaduri, Indira Gandhi Centre for Atomic Research (IGCAR), and Dr. G. Amarendra, Metallurgy and Materials Group (MMG), IGCAR for support. Authors are thankful to Prof. Santosh Kapuria, CSIR-Structural Engineering Research Centre (CSIR-SERC), Chennai for support. Authors also thank the technical staff of Fatigue & Fracture Laboratory (FFL), CSIR-SERC, Chennai for all the help during the ratcheting tests.

### **References**

1. Gupta Suneel K, Goyal Sumit, Bhasin Vivek, Vaze KK, Ghosh AK and Kushwaha HS (2008) Prediction of ratcheting fatigue crack initiation in carbon steel. Proc. 4<sup>th</sup> Indo-German Theme Meeting on Structural Integrity of Pressure Retaining Components, Sept. 22 -23, Mumbai, India, organized by BARC, NPCIL and IGCAR, pp. 1-19.
2. Gupta SK, Goyal S, Bhasin V, Vaze KK, Ghosh AK and Kushwaha HS (2009) Ratcheting-fatigue failure of pressurised elbows made of carbon steel. Proceedings of 20<sup>th</sup> International Conference on Structural Mechanics in Reactor Technology, SMiRT 20, Finland; pp. 110–112.
3. Xia Z, Kujawski D and Ellyin F (1996) Effect of mean stress and ratcheting strain on fatigue life of steel. *Int. J. Fatigue* 18: 335-41.
4. Kang GZ, Li YG, Zhang J, Sun YF and Gao Q (2005) Uniaxial ratcheting and failure behaviours of two steels. *J. Theo. Appl. Fract. Mech.* 43: 199-209.
5. Yahiaoui K, Moffat DG and Moreton DN (1996) response and cyclic strain accumulation of pressurised piping elbows under dynamic in-plane bending. *J. Strain Anal* 31: 135–151.
6. Hasegawa K, Miyazaki K and Nakamura. I (2008) Failure mode and failure strengths for wall thinning straight pipes and elbows subjected to seismic loading. *ASME J. Pressure Vessel Technol.* 130: 011404.
7. Baldev Raj and Jayakumar T (1990) Acoustic emission during tensile deformation and fracture of austenitic alloys, *Acoustic Emission: Current Practices and Future Directions*, ASTM STP 1077, pp. 218-41.
8. Jayakumar T, Baldev Raj, Bhattacharya DK, Rodriguez P and Prabhakar O (1992) Influence of coherent  $\gamma'$  on acoustic emission generated during tensile deformation in Nimonic alloy PE16". *Mater. Sci. Engg.* A150: 51-58.

9. Mukhopadhyay CK, Ray KK, Jayakumar T and Baldev Raj (1998) Acoustic emission from tensile deformation of unnotched and notched specimens of AISI type 304 stainless steels. *Mater Sci. Engg.* A255: 98-106.
10. Bassim MN and Houssny-Emam M (1984) Acoustic emission during the low cycle fatigue of AISI 4340 steel. *Mater Sci. and Engg.* 68: 79–83.
11. Jiang L, Liaw PK, Brooks Somieski CRB and Klarstrom DL (2001) Nondestructive evaluation of fatigue damage in ULTIMET® superalloy. *Mater Sci. and Engg* A313: 153–159.
12. Capelle J, Predan J, Gubeljak N and Pluvinage G (2012) The use of cyclic  $\Delta J_q$  as a parameter for fatigue initiation of X52 steel. *Engg. Frac. Mech.* 96: 82–95.
13. Camerini CS, Rebello JMA and Soares SD (1992) Relationship between acoustic emission and CTOD testing for a structural steel. *NDT& E Int.* 25: 127-133.
14. Blanchette Y, Dickson JI and Bassim MN (1984) The Use of acoustic emission to evaluate critical values of  $K$  and  $J$  in 7075-T651 aluminum alloy. *Engg. Fract. Mech.* 20: 359-371.
15. Mukhopadhyay CK, Sasikala G, Jayakumar T and Baldev Raj (2012) Acoustic emission during fracture toughness tests of SA333 Gr.6 steel. *Engg. Fract. Mech.* 96: 294-306.
16. Augustyniak B, Chmielewski M, Piotrowski L and Sablik MJ (2002) Designing a magnetoacoustic emission measurement configuration for measurement of creep damage in power plant boiler tubes. *J. App. Phys.* 91: 8897–8899.
17. Qiong Ai, Liu Cai-Xue, Chen Xiang-Rong, He Pan, Wang Yao (2012) Acoustic emission of fatigue cracking pressure pipe under cyclic pressure. *Nucl. Eng. Des.* 240: 3616-3620.
18. Ennaceu C, Laksimi A, Herve C and Cherfaoui M (2006) Monitoring crack growth in pressure vessel steels by the acoustic emission technique and the method of potential difference. *Int. J. Pressure Vessels Piping* 83: 197-04.
19. Mukhopadhyay CK, Jayakumar T, Haneef TK, Suresh Kumar S, Rao BPC, Goyal Sumit, Gupta Suneel K, Bhasin Vivek, Vishnuvardhan S, Raghava G and Gandhi P, (2014) Use of acoustic emission and ultrasonic techniques for monitoring crack initiation/growth during ratcheting studies on 304LN stainless steel straight pipe. *Int. J. Pressure Vessels Piping* 116: 27-36.
20. Vishnuvardhan S, Raghava G, Gandhi P, Saravanan M, Goyal Sumit, Punit Arora, Gupta Suneel K and Bhasin Vivek (2013) Ratcheting failure of pressurised straight pipes and elbows under reversed bending. *Int. J. Pressure Vessels Piping* 105-106: 79-89.
21. ASTM A-312/A-312M, Standard Specification for Seamless, Welded and Heavily Cold Worked Austenitic Stainless Steel Pipes, ASTM Int, USA, 2009.
22. Vishnuvardhan S, Raghava G, Gandhi P, Saravanan M, Pukazhendhi DM, Goyal Sumit, Gupta Suneel K, Bhasin Vivek and Vaze KK (2012) Ratcheting studies on type 304LN stainless steel elbows subjected to combined internal pressure and in-plane bending moment. *ASME J. of Pressure Vessel Technology* 134: 041206.
23. Raj B, Jha BB and Rodriguez P (1989) Frequency spectrum analysis of acoustic emission signal obtained during tensile deformation and fracture of an AISI 316 type stainless steel. *Acta Metallurgica* 37: 2211-2215.
24. Yalcinkaya, H, MS Thesis, Reliable Monitoring of Leak in Gas Pipelines Using Acoustic Emission Method, University of Illinois at Chicago, 2013.

**Appendix A**

The frequency of loading for the elbows for different cycle ranges are shown in Table A1. The tests were carried out at a very low frequency during the initial fatigue cycles and the test frequency was gradually increased toward the end of the tests. The frequency of loading was varied from one cycle in 8 min (0.0021 Hz) to one cycle in 90 s (0.0111 Hz).

Figure A1 shows the details of axial and circumferential grid lines on elbows. The circumferential and axial lengths of the bent portion of the elbows were divided into 12 (pitch varied at 4°, 9° and 12°) and 24 (pitch varied at 10° and 20°) segments, respectively and grid lines were marked. The circumferential grid lines were numbered in sequence from “A” to “M”; where “A” denotes the top and “M” denotes the bottom of the bent portion. Similarly, the axial grid lines (1 to 24) were marked; where the grid lines 1 and 13 pass through the intrados and extrados respectively, and grid lines 7 and 19 pass through the two crown locations respectively.

Table A1. Details of test frequency for the two elbows

Elbow 3		Elbow 4	
Cycle No.	Frequency (Hz)	Cycle No.	Frequency (Hz)
1-15	0.0028	1-5	0.0021
16-25	0.0042	6-15	0.0028
26-35	0.0056	16-30	0.0042
36-160	0.0083	31-40	0.0056
161-282	0.0111	41-133	0.0083

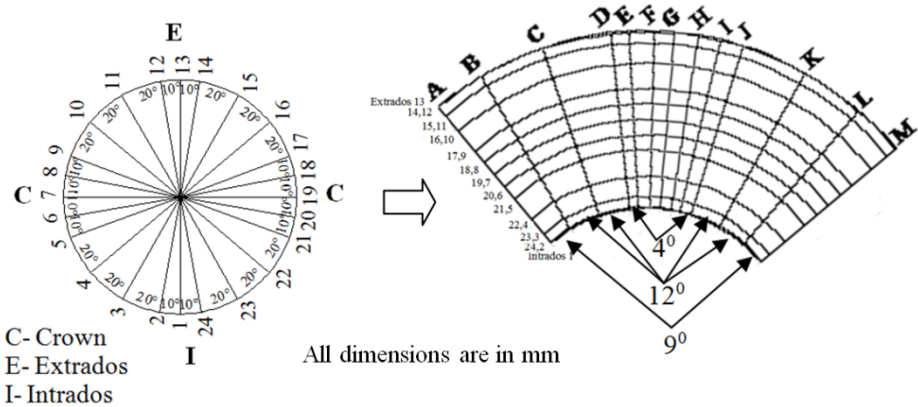


Fig. A1 Details of axial and circumferential grid lines on elbows.

# Far-field Wave Propagation Signals from Pencil Lead Breaks on the Open End of a Thick-Walled Layered Cylinder: Part 1 Amplitudes and frequency content

M. A. Hamstad

Department of Mechanical and Materials Engineering  
University of Denver, Denver, CO 80208, USA

## Abstract

Relative to potential use of acoustic emission (AE) to monitor pressure testing of large steel pressure vessels, in-plane pencil lead breaks (PLBs) were carried out on the open end of a remnant of such a vessel. This remnant had an inner diameter of 58 in. (1473 mm), a wall thickness of 3.3 in. (84 mm) and a total cylindrical length of 125 in. (3175 mm) ending in a head welded to the cylindrical section. The cylindrical section did not have a monotonic wall, but instead it was made of 11 layers (10 at about 0.277 in. [7 mm] thick, and the inside one of about 0.47 in. [11.9 mm] thick) to create a layered pressure vessel (LPV). Due to the presence of the multiple interfaces between layers, a question arose as to whether a sensor mounted on the outer layer was relatively less sensitive and had different frequency content for sources on the inner layers compared to sources on the outer layers? The PLB study used four pairs of different types of AE sensors. The sensor types included: i) strong resonance at a single frequency region; ii) multiple resonance frequencies; iii) and iv) broadband response with different frequency responses. Each sensor pair was acoustically coupled, one on the outside surface and one directly below on the inside surface. The sensor pairs were located at 66 in. (1676 mm) (20 times the wall thickness) from the PLB points. This distance was considerably less than the helical path of about 214 in. (5436 mm). Considering PLBs on the ends of the different layers, Part 1 focused on changes in the character of the AE signals from the four sensor types. Comparisons for each sensor type were made of the amplitudes of the outside sensor relative to those of the inside one. In addition, as the PLB was moved to different layers, the changes in the signals and frequency content of the different sensor signals were studied. Except for one sensor type, the outer sensor peak signal amplitudes relative to the inner sensor peak signal amplitudes changed significantly as the PLB layer moved from the outer layers to the inner layers. In addition, the signals and frequency content also varied with changes in the PLB layer. The results represent a lower bound due to the potential for some increased transmission between layers when an LPV is pressurized to significant levels.

**Keywords:** Thick-walled layered cylinder, pencil lead breaks, four sensor types, inside and outside sensors, acoustic emission wave propagation, amplitudes and frequency content.

## Introduction

Acoustic emission (AE) testing has been used for many years to monitor pressurization of pressure vessels as evidenced by the ASTM standards (E569 first version 1976 and E1419 first version 1991 [1]). These standards do not specifically address the steel vessel of current interest, namely a type of vessel made up of layers of steel rather than a monotonic vessel wall. Several hundred similar layered vessels were manufactured starting in the late 1950's and early 1960's for use by the National Aeronautics and Space Administration (NASA) and other commercial organizations. In the current time frame, to enhance the analysis of AE results from a monitored pressure test of such a vessel, an important step is to understand the wave propagation of AE-like waves. An opportunity was available to carry out wave propagation studies on a remnant of such a vessel, which had been cut from a large layered pressure vessel (LPV). Thus, the overall goal of this study was to examine far-field AE signals from in-plane pencil lead breaks (PLBs) using four different AE sensor types as the PLB layer was changed. The specific goal in Part 1 was to examine the sensor signals as a function the four sensor types to determine the amplitudes, frequency content and propagation characteristics resulting from PLBs on different layers

of the exposed open end of the remnant. In addition, the results may guide the best choice of sensor type(s). Besides the uniqueness of the layered construction, a further unique aspect was the use of pairs of like AE sensor types located back-to-back on the outside and inside of the vessel wall.

**Wave Propagation Specimen**

An overall view of the LPV remnant is shown on the left side of Fig. 1. On the right side the sensor location on the inside is shown. The remnant has a total length of about 157 in. (3990 mm) (note in this paper all dimensions are first given in their measured units and then converted to S.I. units, if they were not originally measured with those units) and an inside diameter of 58 in. (1470 mm). It is made up of a layered cylindrical section of about 125 in. (3175 mm) in length, which was welded to a steel head with a monotonic wall. Based on the manufacturer’s fabrication data, the wall thickness is about 3.3 in. (84 mm), and it is made up of 11 layers. The inner layer was about 0.47 in. (11.9 mm) thick, and the remaining layers were about 0.277 in. (7 mm) thick. The open end where the PLBs were carried out was locally machined where the PLBs were done to smooth out the roughness resulting from water jet cutting. At the 66 in. (1676 mm) distance (20 times the wall thickness), where the sensors were located, flats were machined/ground on the inside and outside so that good contact could be made between the sensor faces and the vessel wall. These flats were about 0.01 in. (0.3 mm) deep. The inside flat was of the most



Fig. 1. Showing the remnant on the left and the inside sensor on the right, along with the trigger sensor (PICO) on the open end. The arrowhead pointing to PICO sensor is the region of close-up in Fig. 3.

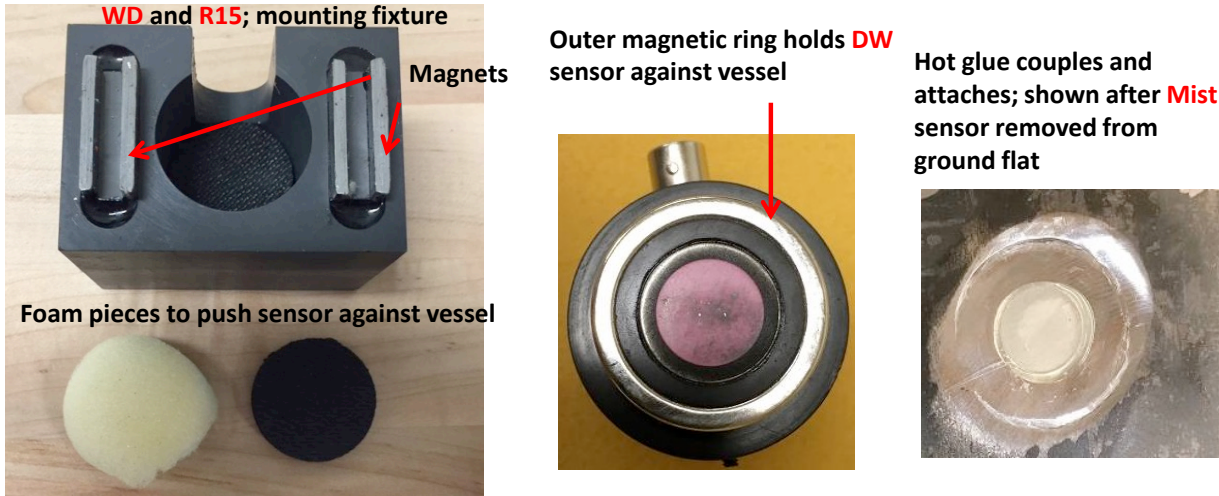


Fig. 2. Showing attachment fixtures and methods of attachment for the sensors.

importance due to the curvature of the vessel wall, which would have offset the central part of the sensor face from the wall. The paint on the outer surface had been removed. The alignment of the wave propagation path from the PLB location to the sensors was selected so that no nearby axial welds were present.

### Acoustic Emission Sensor Types/Attachment/Coupling

Four different types of AE sensors were used; a pair of the same type at a time. Each sensor had an internal DC powered preamp. The manufacturer’s information about the sensors/preamps is shown in Table 1. As shorthand for the rest of this paper, from the first column of the table moving down, the shorthand labels are: DW, Mist, WD and R15. One sensor the R15 has a strong resonance in a single frequency region. Another resonant sensor, the WD has more than one resonance due to its design with more than one sensing element. The other two sensors Mist and DW are broadband, but the frequency response characteristics of the Mist sensor were altered due to the couplant used, as will be shown later in this paper. Three of the sensor types were held in place by the force from a magnetic fixture or magnetic ring on the sensor’s outer diameter, as shown in Fig. 2. The other sensor type, Mist, was both held in place and acoustically coupled by hot melt glue (residual glue layer shown in Fig. 2 was about 0.03 in. [0.8 mm] thick). The other three sensor types were acoustically coupled by Apiezon M grease.

Table 1. Sensor characteristics

Sensor ID	Mfr. electronic frequency specification, kHz	Preamp gain, dB	Resonance characteristics from mfr.	Outer diameter, mm
Digital Wave, B454 - IPP	20 - 1500	20	Broadband, not strongly resonant	14
Mistras, PKBBI	20 – 600	26	Broadband, not strongly resonant	18
Mistras, WDI	200 – 900	40	Resonant at several frequencies	27
Mistras, R15I	50 - 400	40	Resonant at about 150 kHz	26

### Experimental Details

The PLBs were generated by the fracture of about a 3 mm length of 2H lead held in contact with the open end of the remnant. The lead diameter was selected to be 0.7 mm to create better signal-to-noise (S/N) ratios so that the wave propagation characteristics could be determined with greater confidence. To provide a nearly constant trigger time (relative to the time of the PLB) for waveform recording a small diameter (5 mm) PICO sensor (resonant at about 500 kHz) was coupled and held in place by Tacky Wax on the same layer where the different PLBs were made. The center of this sensor was only about 0.48 in. (12 mm) from the PLB points. It was attached to a standard external preamp with 40 dB gain and a high pass 100 kHz filter. The use of the trigger sensor allowed all the sensor signals resulting from the PLBs on different layers to be correlated to the same time base. Figure 3 shows a close-up photograph of the location of the PICO sensor on layer 10 as well as the red labeling of the layer numbers. The PLBs were carried out near the middle of the end of each layer. Figure 3 also shows by black marks the top and bottom of the different layers. At least five PLBs were done for each selected layer. Most of the selected layers were from near the outer or inner layers, since the comparative transfer of the waves to sensors farther or nearer the PLB layer was of the most interest. All sensor preamps were powered using a decoupling circuit. After the decoupler the signals from the back-to-back sensors were high pass filtered with a five-pole passive Butterworth filter at 10 kHz. The inputs at the waveform recorder were terminated by 50 ohms. All testing was done inside at nominal room temperatures.

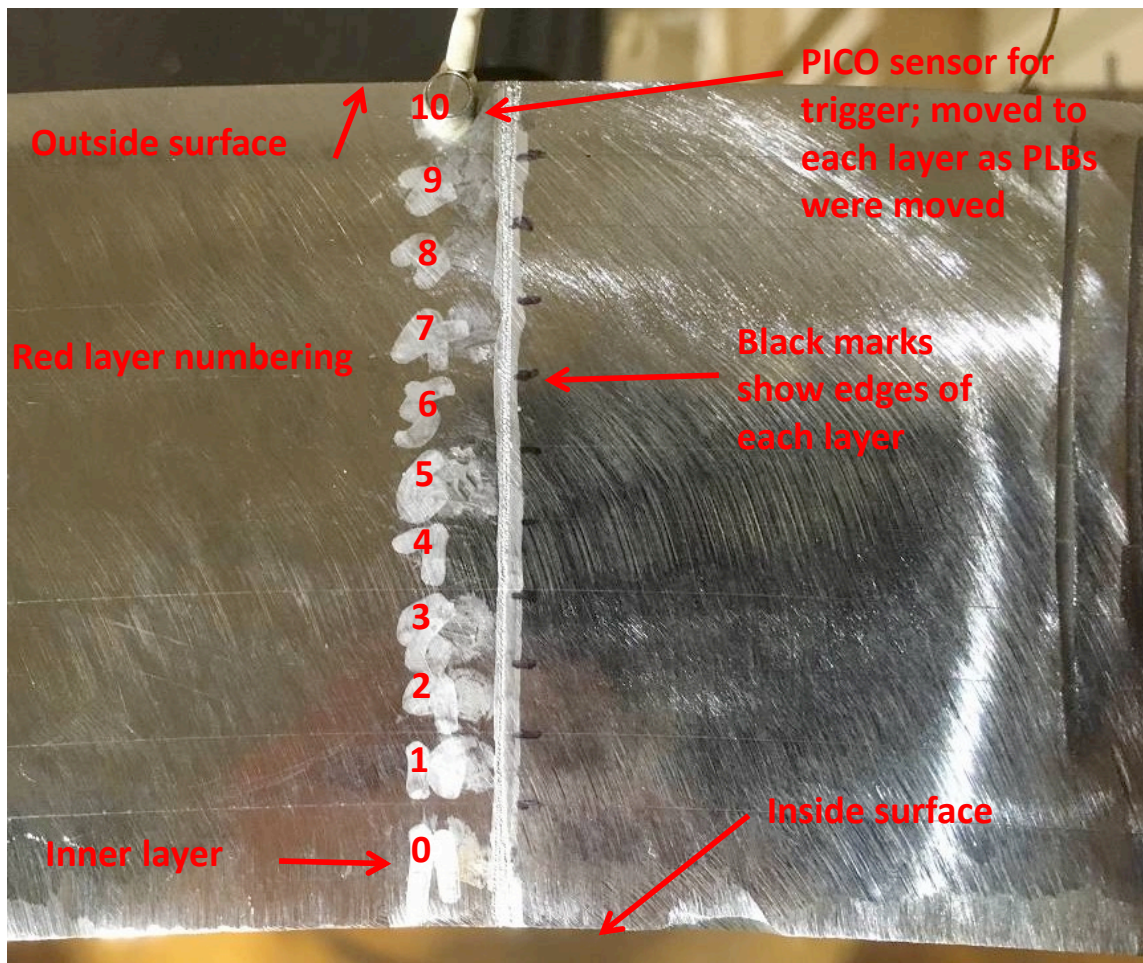


Fig. 3. Shows close-up of layers and position of PICO sensor for PLBs on layer 10. Faint lines are the layer interfaces as marked in black.

The waveforms from the trigger sensor as well as those from the back-to-back sensor pair were simultaneously recorded by a PicoScope at 5 MHz when the voltage threshold for the PICO channel was exceeded. A 500  $\mu$ s pretrigger was used along with a total digitized length of 25000 points for each of the three signals. The waveforms were recorded with 12 bits resolution. The recorded signals were exported as txt files and then imported to a software package for processing. In the presentation of the results, the figures and discussion are biased towards the outer sensor signals, since those are the only sensor signals available in a real AE test of an LPV.

## Experimental Results

### A. Contrasts in the outer sensor signals between sensor types for PLBs on the same layer

Since there were four significantly different sensor types, it is of interest to compare the signals from the different types for PLBs on the same layers. From the five or more PLBs on each selected layer for each sensor type, typical signals were selected. The choice of the typical signals was not made based on peak amplitudes; instead it was made on visually viewing the waveform characteristics (all five waveforms at once for each case) in the signal time increment prior to any arrival of helical path signals. Figure 4 shows the selected typical outer sensor signals from the four sensor types for PLBs on the middle of the ends of the outer layer 10 and inner layer 0. Unless stated, all the signals in this paper were not altered by the gains of the various preamplifiers. In Fig. 4 and subsequent figures of signals, two vertical red reference lines (or partial lines for clarity) are included. These lines are the calculated first

arrival times of fundamental extensional ( $S_0$ ) and flexural ( $A_0$ ) modes of Lamb waves. Initially, the time of arrival of the peak of the first positive half cycle in the PICO trigger signal was obtained. From this time the propagation time from the PLB point to the center of the PICO sensor location was subtracted. This calculation provided the PLB time. To this time, the propagation times of the extensional and flexural first arrivals to the sensors were added. The velocities from Kolsky [2] used for these calculations were bulk velocity  $5.94 \text{ mm}/\mu\text{s}$  to the PICO sensor and  $5.42 \text{ mm}/\mu\text{s}$  and  $3.22 \text{ mm}/\mu\text{s}$  respectively for the extensional and flexural modes to the distant sensors. The calculated times are an extensional mode first arrival at about  $813 \mu\text{s}$  and a flexural mode first arrival at about  $1024 \mu\text{s}$ . The presented signals (Fig. 4) are shown from  $0.75 \text{ ms}$  (to provide some signal representing background noise prior to the AE signal arrival) to  $1.45 \text{ ms}$ , which corresponds to 3500 points. The termination at  $1.45 \text{ ms}$  was before the extensional wave first arrival time from the two helical paths which was calculated to be about  $1.50 \text{ ms}$ . For the Mist and R15 sensors, the signals were low pass software filtered respectively at  $500 \text{ kHz}$  and  $400 \text{ kHz}$  with a eight-pole Butterworth filter to remove some of the background electromagnetic noise that was unavoidably present at certain times due to other activities going on in the test facility building. The Mist sensor signals were most affected by this noise due to the use of the sensor manufacturer supplied  $1 \text{ m}$  sensor cable that had the required SMA connector to attach to the sensor. This cable did not have high shielding. After this sensor cable, a well shielded RG58  $50 \text{ ohm}$  cable with BNC connectors was used. This cable type was used to directly connect to the other three sensors. The above low pass filtering did not alter the key results with these sensors, as will be shown later, since the primary frequency content was well below these low pass frequencies.

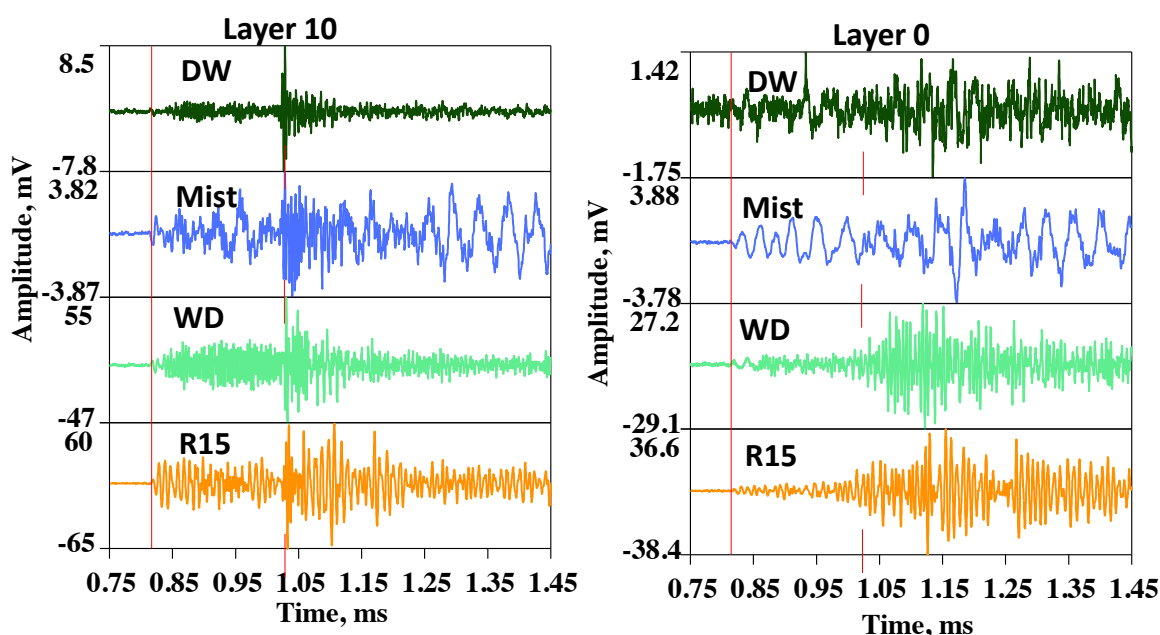


Fig. 4. Typical signals from all four sensor types located outside for PLBs on the ends of the outer layer 10 and inner layer 0.

Some clear observations can be made from Fig. 4. First, for the PLBs on layers 10 and 0, the first arrivals of the signals correspond reasonably well with the calculated first extensional arrival for all the sensors, except one sensor type, when viewed with a shorter time scale and more sensitive vertical scale in Fig. 5. In the case of the DW sensor, for a PLB on layer 0, there was no correspondence. This result seems to be related to a poor S/N ratio. The poor S/N ratio can be the result of either less low frequency response and/or higher preamp noise. Since these layers represent the extremes, as expected for PLBs on all the intermediate layers, for all the sensor types except the DW, the sensor signal arrivals were found to correspond to the calculated extensional arrival (this result is not shown here, but some results are shown in later figures in part E). In the case of the DW sensor only for PLBs on layers 10 and 9 was a correspondence present. Second, for all of the sensor types for PLBs on the end of layer 10 (the outer

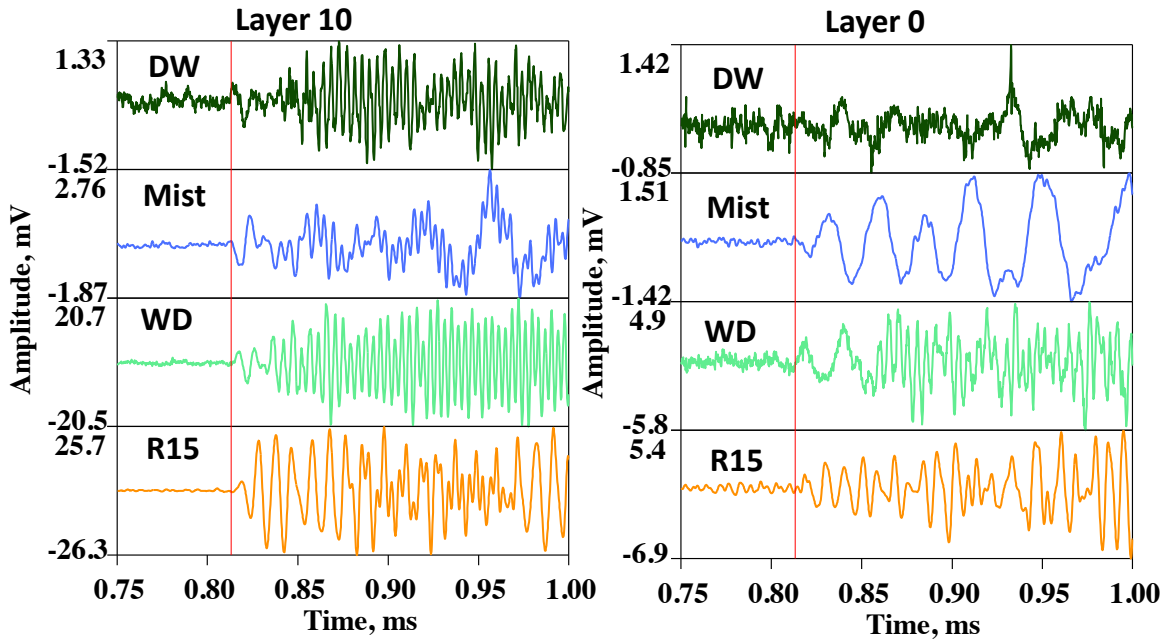


Fig. 5. The same waveforms as in Fig. 4 with a shorter time scale to better define the first arrivals of the extensional mode.

layer) there are clear indications in the signals of the flexural first arrival near the calculated value. The presence of higher frequencies at the initial arrival of the flexural mode is as expected. Third, for the PLB on the end of the inside layer 0 the correspondence of the signals to the calculated flexural mode arrival is not clear for all of the sensor types. Fourth, there are large differences in the character of the signals for the different sensor types for both PLB layer cases shown. The signals from sensor types WD and R15 were the most similar to each other, and the broadband sensor signals DW and Mist differed substantially from each other in their low frequency character.

#### *B. Contrasts in the outer sensor frequency content between sensor types for PLBs on the same layer*

Figure 6 illustrates the differences in the frequency content in the signals shown in Fig. 4 for the PLBs on the ends of layers 10 and 0. These results were developed using the same time portion of the signals from 0.75 ms to 1.45 ms. The fast Fourier transform (FFT) was calculated with a fill with zeros routine that extended the number of points from 3500 to 4096 to provide the results with increments of 1.22 kHz. Clearly, there are very significant differences even though the source is essentially the same for the results from the different sensor signals. Both the frequency range of content and the peak regions differ. The differences between the sensor types are the largest for the PLBs on the outer layer 10. In this case, the DW sensor results show that a very wide range of frequencies were excited as would be expected for a broadband sensor. The Mist sensor results also show a broad range, but the frequency content is dominated by very low frequencies. This dominance, which is related to the use of hot melt glue as the couplant, will be discussed later in this paper. The resonant outer sensors for the PLBs on layer 10 show some differences related to their resonant behavior. The R15 signals have a dominant peak at about 100 kHz, while the WD signals have more than one dominant region with content up to even about 600 kHz due to the design with two different sensing elements. Turning to the frequency content in the signals for the PLBs on the inner layer 0, there is a shift to lower frequency content particularly for the DW and WD sensors. On the other hand the peak regions for the Mist and R15 sensor signals remains quite similar to the frequency content for the PLBs on layer 10.

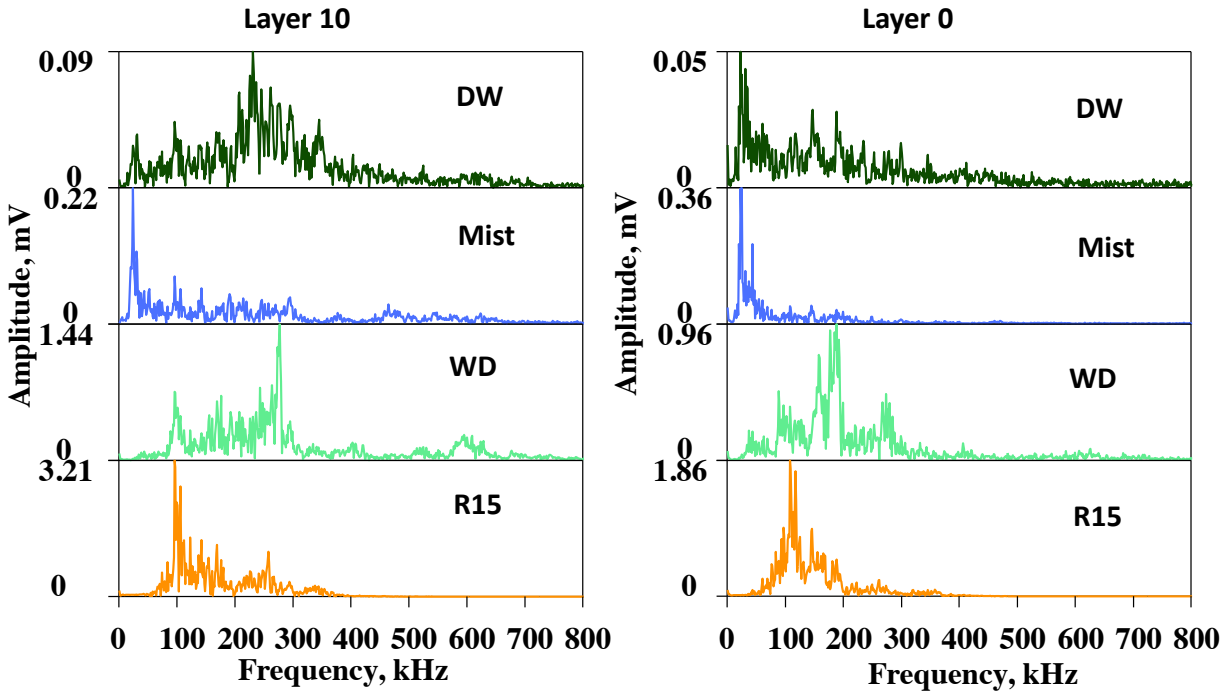


Fig. 6. Frequency content results for the signals in Fig. 4 for all four sensor types located outside for PLBs on the ends of the outer layer 10 and inner layer 0.

### C. Changes in the signals from the individual outer sensors types as the PLB layer changes

The observations in this section are confined to the flexural arrivals as the correspondence to the extensional arrivals has already been presented in the previous section. In Fig. 7, the outer sensor signals as a function of the PLB layer are shown for the two broadband sensors, DW (left) and Mist (right). The DW sensor signals for the PLBs on layers 5, 2, 1 and 0 (sequence of layer numbers will be ordered from the outer to inner in this paper since the outer sensor is the only one that can be used in an actual test) have a different character than the signals from the PLBs on the outer layers 10, 9 and 8. For the PLBs on the outer three layers, the signals show a clear first arrival of the flexural mode and correspondence with the calculated value, and the signals are similar to each other in both modal regions (“extensional region” from first arrival to the arrival of the flexural mode with the following “flexural region”). For the PLBs on the four layers (5, 2, 1, 0) some distance further below the outside, the outside sensor signals are similar to each other, but the flexural mode first arrival is not clearly defined and does not clearly correspond to the calculated arrival. Also, for these four PLB layer cases, it seems the high amplitude portion of the flexural region extends for a longer time period than for the three PLB layers (10, 9, 8) close to the outer surface. This difference is primarily due to the scaling for the three outer PLB layer cases, as a result of the large initial amplitude of the flexural arrival. The peak amplitude of the signals in all the PLB layer cases is either the flexural mode first arrival or at a later time in the region of dominant flexural mode.

As shown on the right side of Fig. 7, the Mist sensor signals again show that the signals from the PLBs on the outer three layers are reasonably similar to each other, and the arrival of the flexural mode, indicated by a short region of higher frequency, corresponds to the calculated value. This correspondence for the flexural mode is not clear for the four lower layer PLB cases. The four lower layer signals are quite similar to each other in character with mostly low frequency content. In contrast to the DW sensor signals, the Mist sensor signals have some similarity to each other for all the PLB layer cases. This similarity is in their lower frequency content in both the extensional mode region and the latter part of the flexural mode region.

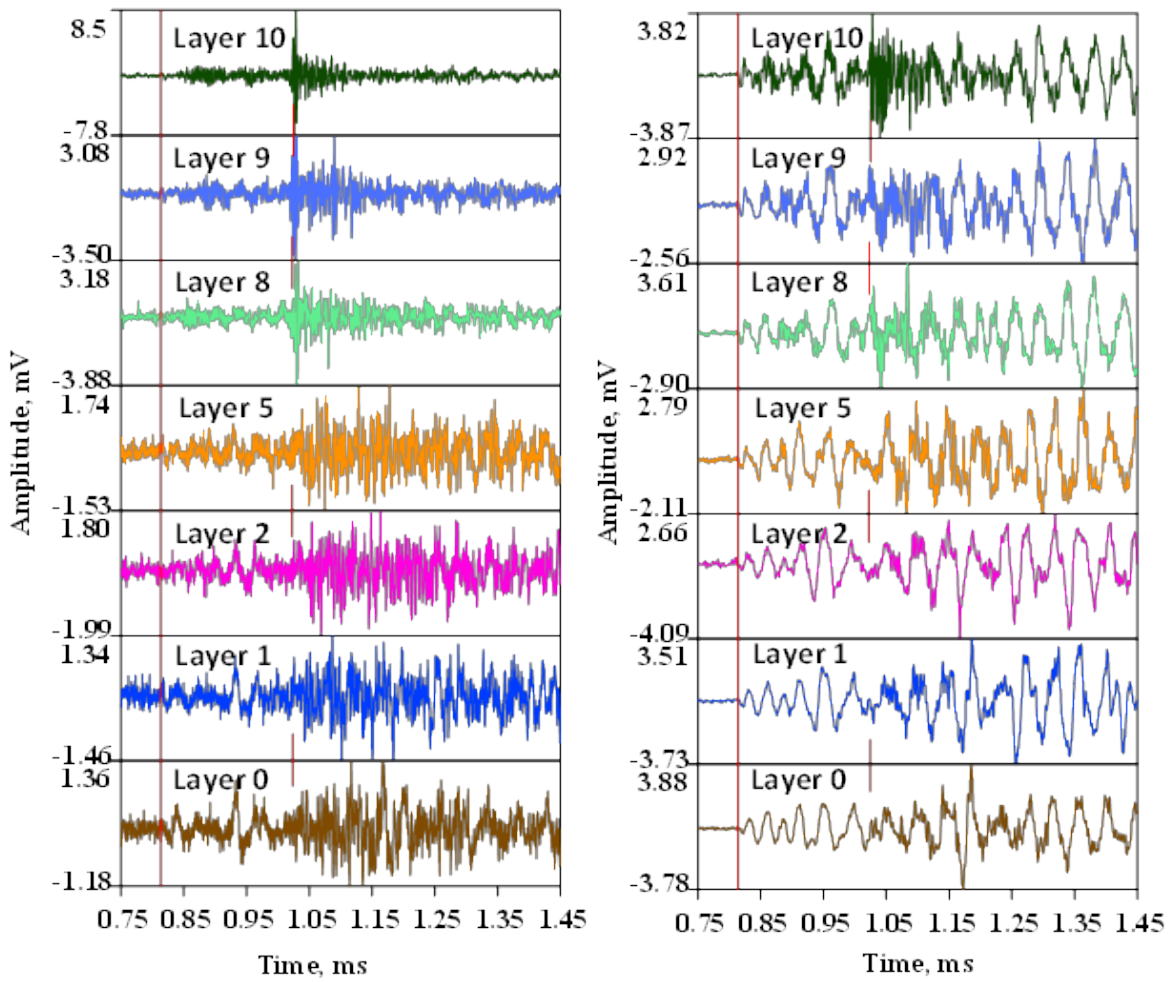


Fig. 7. Signals versus end of PLB layer for DW sensor (left) and Mist sensor (right).

In Fig. 8, the outer sensor signals are shown for the two resonant sensors the WD (left side) and R15 (right side) for PLBs on the same set of seven layers. For both sensors types the first arrivals of the flexural mode correspond reasonably well with the calculated values for PLBs on the ends of layers 10, 9 and 8. In the case of the WD and R15 sensors, this behavior possibly also extends to some of the layers 5, 2 and 1. Also, for both sensor types, the flexural mode's distinct first arrival seems to be missing for PLBs on layer 0. As with the Mist sensor signals, there is some signal similarity for each sensor type as the PLB layer changes. For both of these sensor types, the signals for PLBs on layers 5, 2, 1 and 0 also have an extended portion of high amplitude in the flexural region. This difference is again primarily due to the scaling for the three outer layer cases as a result of the large initial amplitude of the flexural arrival. Again for both of these sensor types, the location of the peak amplitude is in the flexural region.

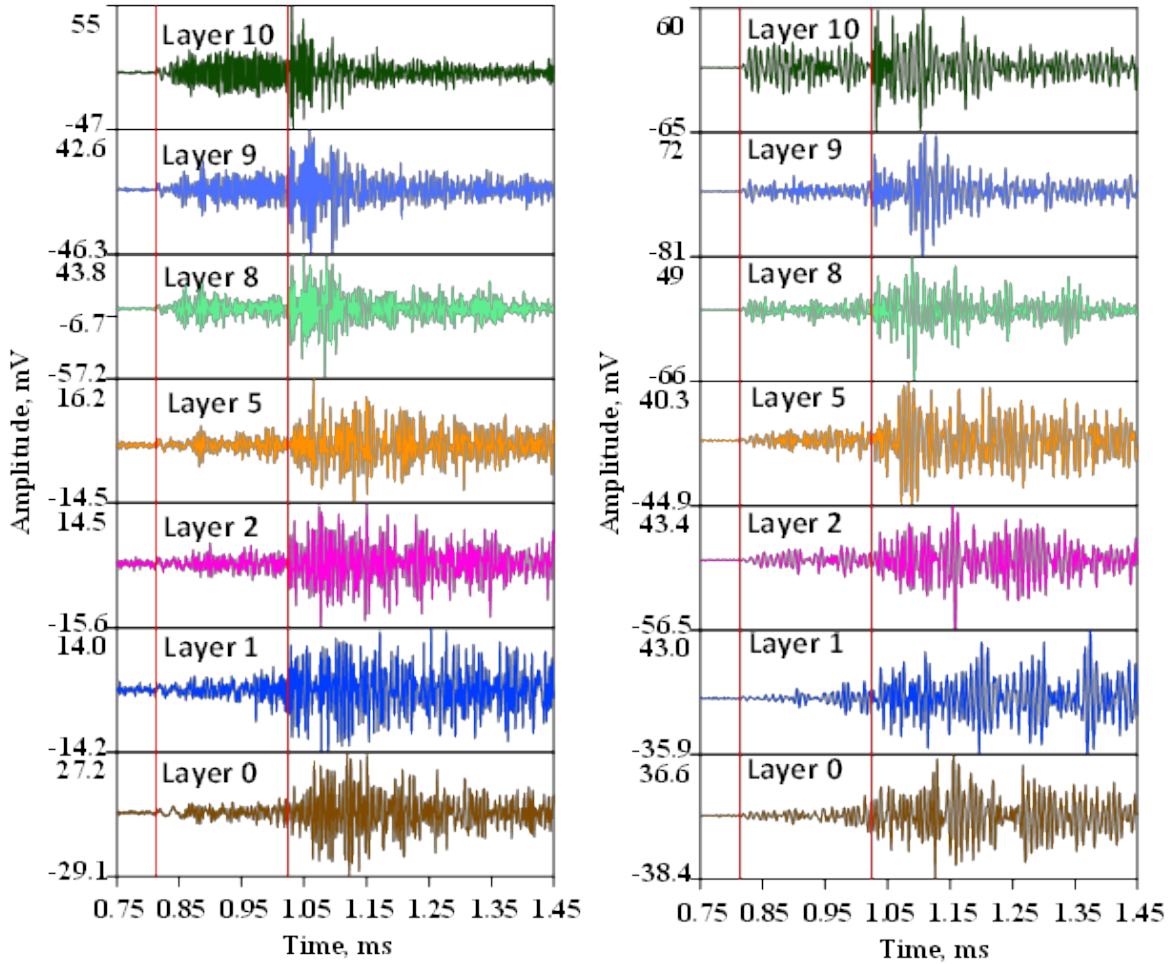


Fig. 8. Signals versus end of PLB layer for WD sensor (left) and R15 sensor (right).

*D. Changes in frequency content of the individual signals of the outer sensor types as the PLB layer changes*

The same approach for the calculation of the frequency content was used as described previously. Figure 9 for the DW and Mist outer sensor signals and Fig. 10 for the WD and R15 outer sensor signals show the FFT results as a function of the PLB layer. To show a similar frequency region for all four sensor types, the FFT results are shown out to 800 kHz even though that range is not applicable to all the sensor/preamp types and to the previously described low pass filtering. Several aspects are clearly observed in these figures. First, as the PLB layer moves closer to the inner layer, there is a reduction in the presence of higher frequencies. This is particularly evident in the signals from the DW and WD sensors. Second, it is now clear that the Mist sensor signals have been altered by the use of the hot melt glue as the couplant, which acts as a filter to prevent high frequencies from reaching the sensing element. The primary frequency content of this sensor's signal is low at less than 200 kHz, and the peak intensities are well below 100 kHz. A reference that examined this material as a coupling agent [3] showed a drop-off in sensitivity at frequencies above 200 kHz. Additional work with the same sensor, showed much higher frequency content up to about 600 kHz [4] in the signals from PLBs on a steel plate using vacuum grease couplant. Third, the sensors that primarily have low frequencies in their FFT results, R15 and Mist, do not show a large change in the FFT frequency region of highest intensity, as the PLB layer moves from the outer layers to the inner layers. Fourth, for the DW and WD sensors with significant high frequencies present, there is a distinct change in the peak frequency region for PLBs on inner layers as

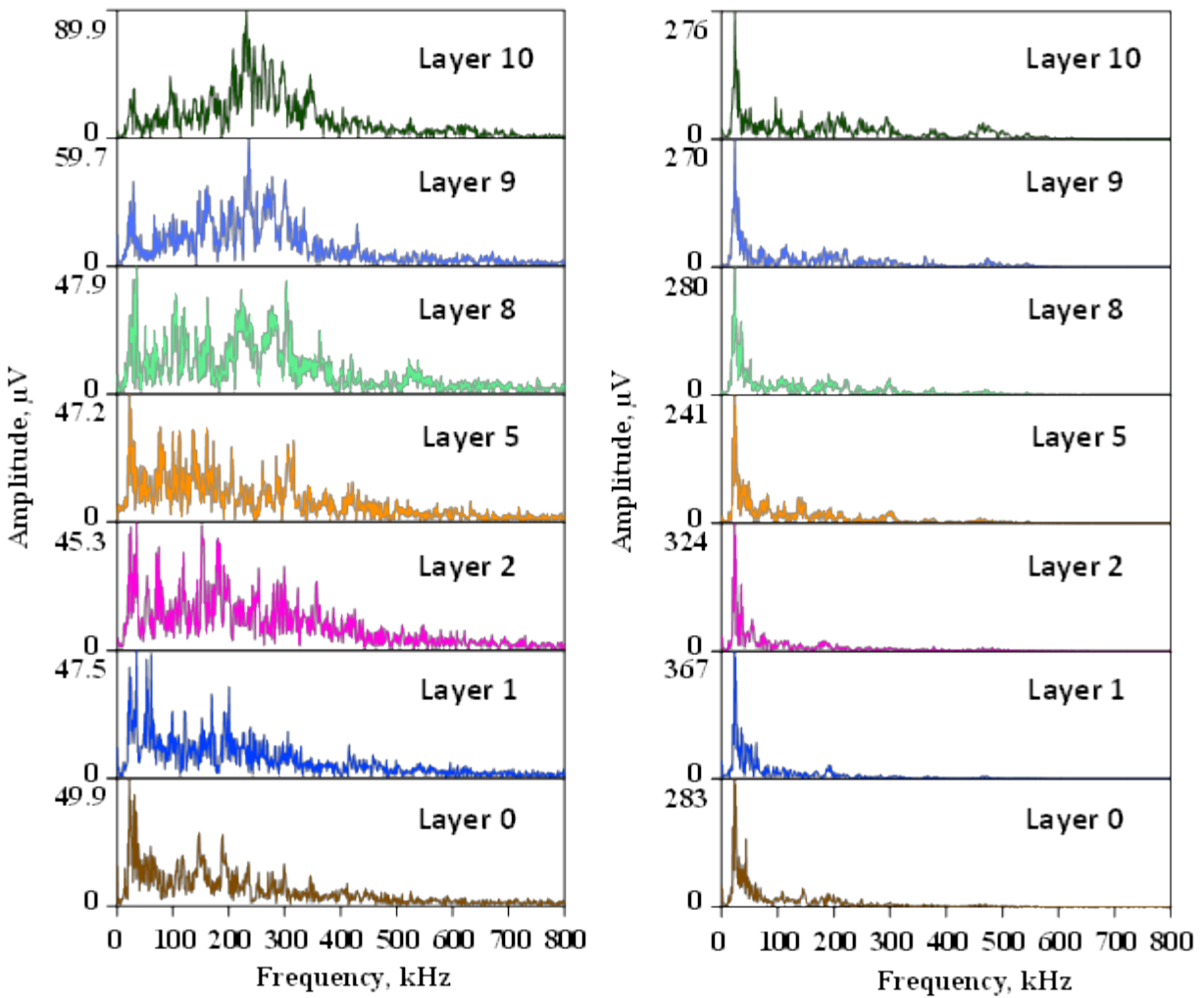


Fig. 9. Frequency content versus end of PLB for DW left and Mist right.

compared to the PLBs on the outer layers. For example, the DW sensor signal has a peak at about 230 kHz for the outer layer 10 PLB, and already for the PLB on layer 8 the peak region is centered at about 35 kHz. For the PLBs on the remaining lower layers the peak region remains somewhat similar, along with less and less intensity above 100 kHz. The peak frequency of the WD sensor signals changes from about 270 kHz for PLBs on layers 10, 9 and 8 to about 180 kHz for PLBs on layers 5, 2, 1 and 0. The peak frequency of the Mist signals is about 25 kHz for all the PLB layers shown. Similarly for all the PLB layers shown, the peak frequency for the R15 sensor signals varies from about 100 kHz to 120 kHz.

#### E. Comparisons of the outer and inner sensor signals for PLBs on the same layers

Since the PLBs were done with the same type sensor coupled on the inside as on the outside, direct comparisons could be made of the signals from PLBs on the layers. Rather than show a comprehensive set of figures, representative cases were selected for each sensor type. Thus, the figure for each sensor type shows the outer and inner sensor signals as a direct comparison of PLBs on layers 10 and 8 near the “level” of the outer sensor and on layers 2 and 0 near the “level” of the inner sensor. In each of these comparisons of the signals, a shorter time increment from 0.75 ms to 0.85 ms is shown as an inset to focus on the initial arrival of the extensional region with more sensitive scales. As before in these figures vertical red lines (for the flexural mode in the longer time increment signal and for the extensional mode in the shorter time increment signal) show the calculated first arrival times of the fundamental modes. Also, the two sensor locations are labeled out and in. It should be kept in mind when viewing these comparisons, that the thicknesses of the layers on which the two sensors are mounted are different. The

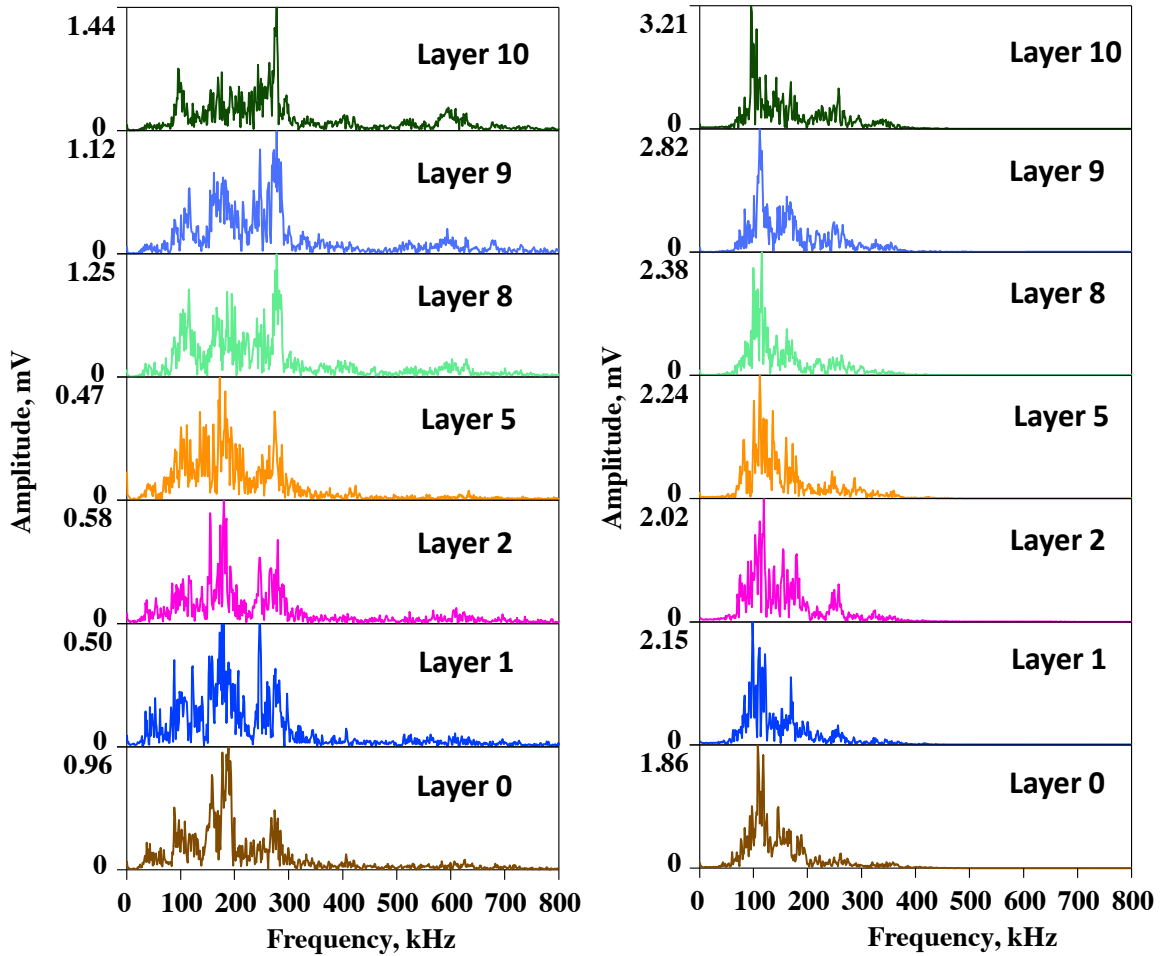


Fig. 10. Frequency content versus end of PLB for WD left and R15 right.

outer sensor is mounted on a layer with thickness of about 7 mm thickness while the inner sensor is mounted on a layer of thickness of about 11.9 mm thickness. Thus, if the signals are dominated by or in part made up of Lamb wave propagation confined to just the layers upon which the sensors are mounted, the frequency content in the waves will vary due to the thickness differences. Figures 11 – 14 show the comparisons respectively for the DW, Mist, WD and R15 sensor pairs.

From examination of the insets in the figures, it is clear, as has been pointed out earlier, that the calculated extensional first arrival corresponds quite well with the signal arrivals for both the outer and inner sensors for all four PLB layers and for all the sensors except the DW sensors. For the DW sensors, the figures imply that the primary issue is the S/N ratio. Also, an important observation of this correspondence is the relatively low frequencies at the initial extensional arrivals, which corresponds to the theory of Lamb waves.

Next the potential correspondence of the calculated first arrival of the flexural mode is examined relative to the signal characteristics of the outside and inside sensor signals for the PLBs nearest the layers the sensors are mounted on. First, for all four sensor types, the outer sensor signal corresponds to the calculated flexural mode arrival time for PLBs on the ends of the outermost layers 10 and 8. By eye, this correspondence is due to identifying a small time increment of “dense” high frequency at the calculated arrival time. This behavior is consistent with the theory-based expectation that the initial arrival frequencies of the flexural mode are from higher frequencies. Second, contrary to the observation for the flexural mode arrivals for PLBs on layers near the outer sensors, the correspondence to the calculated flexural arrival time of the inner sensors signals for PLBs on the nearby layers 2 and 0 does not apply. In fact, what the inner sensor signals show in some sensor cases is a delayed “dense” high frequency time

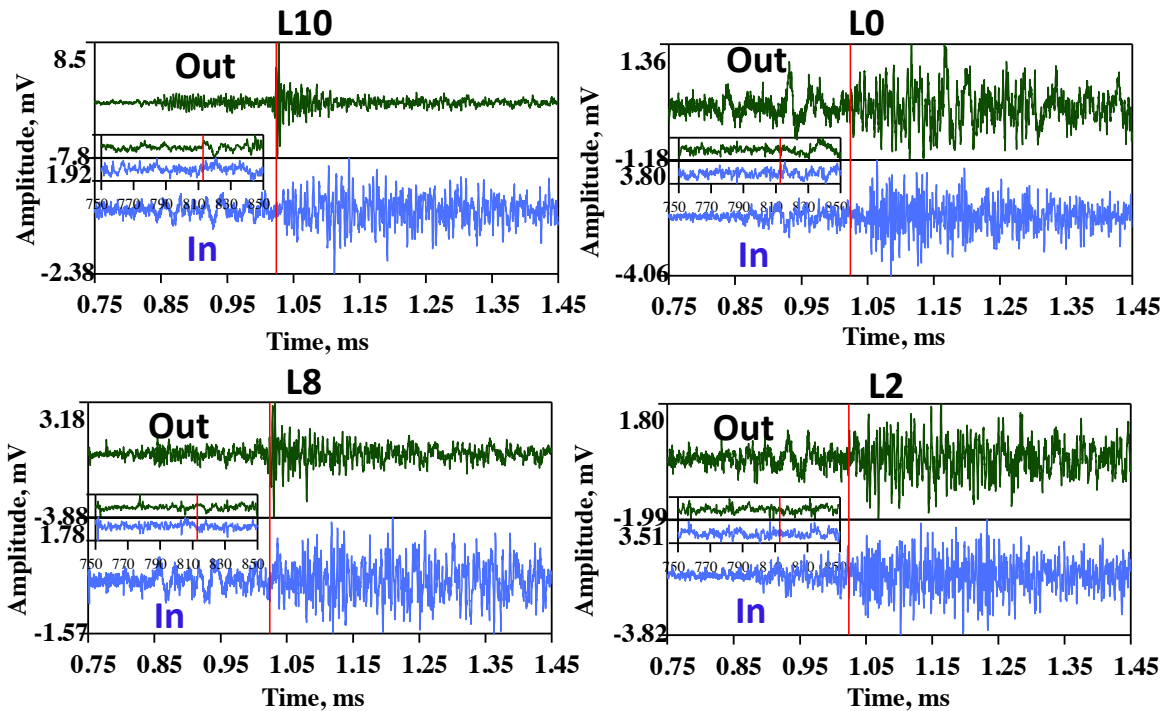


Fig. 11. Comparisons of signals from the outside and inside DW sensors versus end PLBs on different layers.

increment that is best shown in the signals from the DW and Mist inner sensor signals (less for the Mist case for the PLB on layer 2). The delay is typically about  $70 \mu\text{s}$ , which at a bulk shear velocity of  $3.22 \text{ mm}/\mu\text{s}$  corresponds to a distance of about 225 mm. This distance is much greater than any small measurement error made in locating the inner sensor flat directly below the outer sensor flat. A possible explanation for this delay may be the presence of a full-thickness inner layer circumferential weld located about 9 in. (230 mm) prior to the center of the inner sensor flat. The width of this weld was on the order of 0.8 to 1 in. (20 to 25 mm). Other than this possible explanation, the author is not aware of any other possible explanation. For the WD and R15 inner sensor signals from PLBs on layers 2 and 0, the signals do not clearly show even these delayed arrivals, except possibly the WD sensor for the PLB on layer 0.

When the potential correspondence of the calculated flexural mode arrival time was compared to the signals from the sensors located at a “level” well away from the PLB “level,” the correspondence of the calculated flexural arrival is not clearly apparent in all the PLB cases and all the sensors. The potential reason for this fact may be a loss of transfer of higher frequencies between the layers due to imperfect contact (asperity-to-asperity) between the layers. Some work has been published relative to the transfer of ultrasonic signals between layers with imperfect contact. For example reference 5, shows decreasing transfer between two aluminum plates as the frequencies increased from about 2 or 3 MHz to 7 or 9 MHz and increasing transfer of frequencies as the compressive load between the plates increased from 9 MPa to 79 MPa (1305 psi to 11460 psi). The surfaces of these plates had been machined to a root-mean-square (RMS) finish of  $0.68 \mu\text{m}$ . This study included both normal incidence and oblique incidence as well a model that was fitted to the experimental results. No references were located for the kHz frequency range relevant to this work. Also, no references were found that addressed the very large number of interfaces that are encountered in full-thickness propagation of waves in an LPV. Further, the roughness of the interface surfaces of the steel layers in the LPV is unknown. Since it is the higher frequencies that are present at the first arrival region of the flexural mode, this potential loss of higher frequencies with their smaller wavelengths seems to be a plausible explanation. This imperfect contact did not create an issue with the extensional mode since low frequencies with their larger wavelengths make up the initial portion of the arrival of this mode.

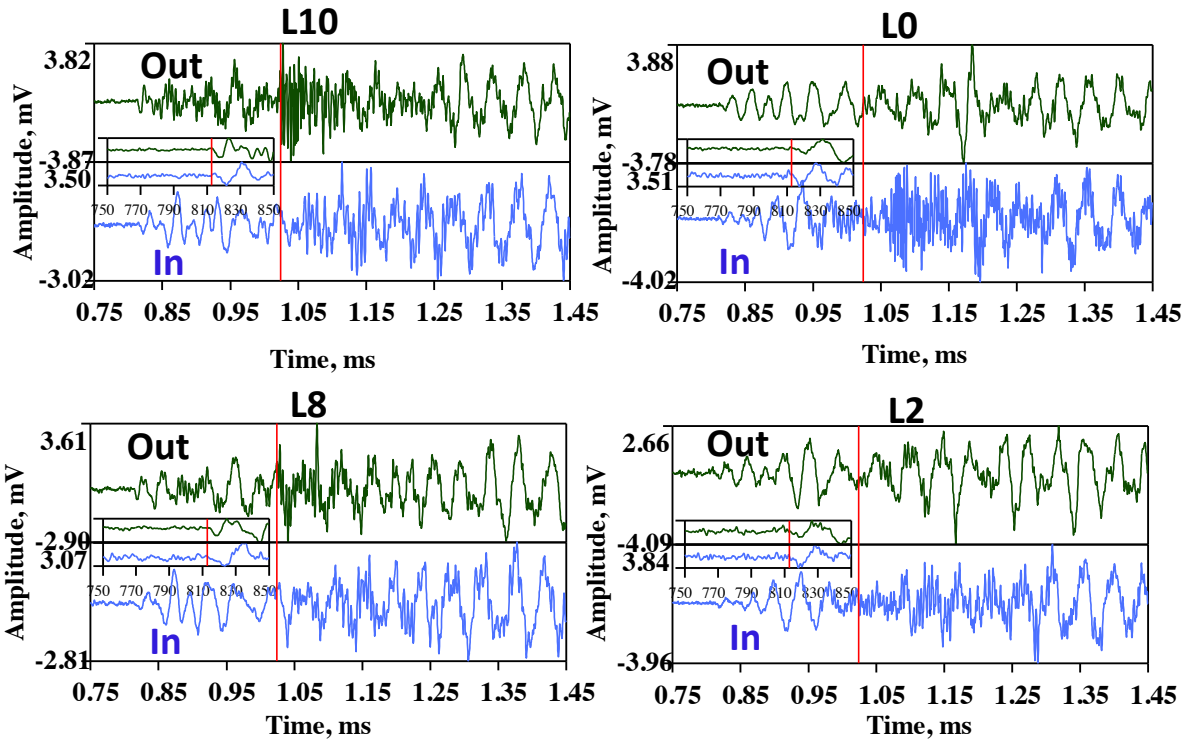


Fig. 12. Comparisons of signals after low-pass 500 kHz from the outside and inside Mist sensors versus end PLBs on different layers.

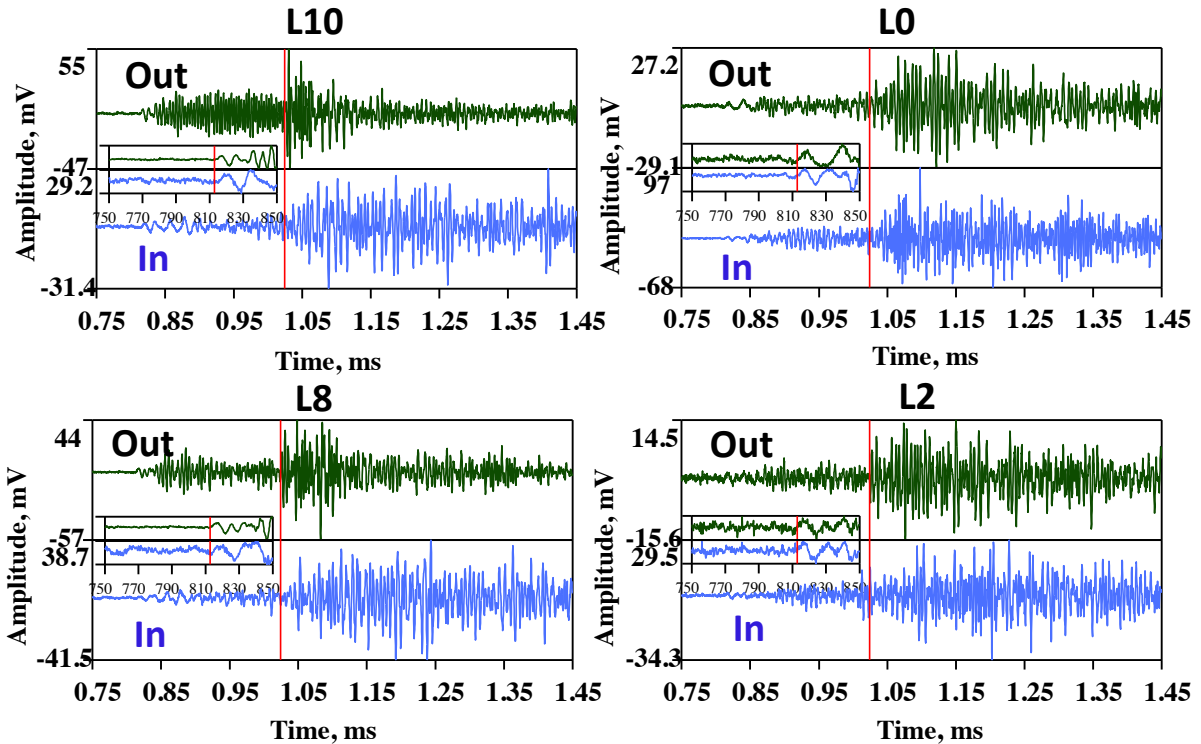


Fig. 13. Comparisons of signals from the outside and inside WD sensors versus end PLBs on different layers.

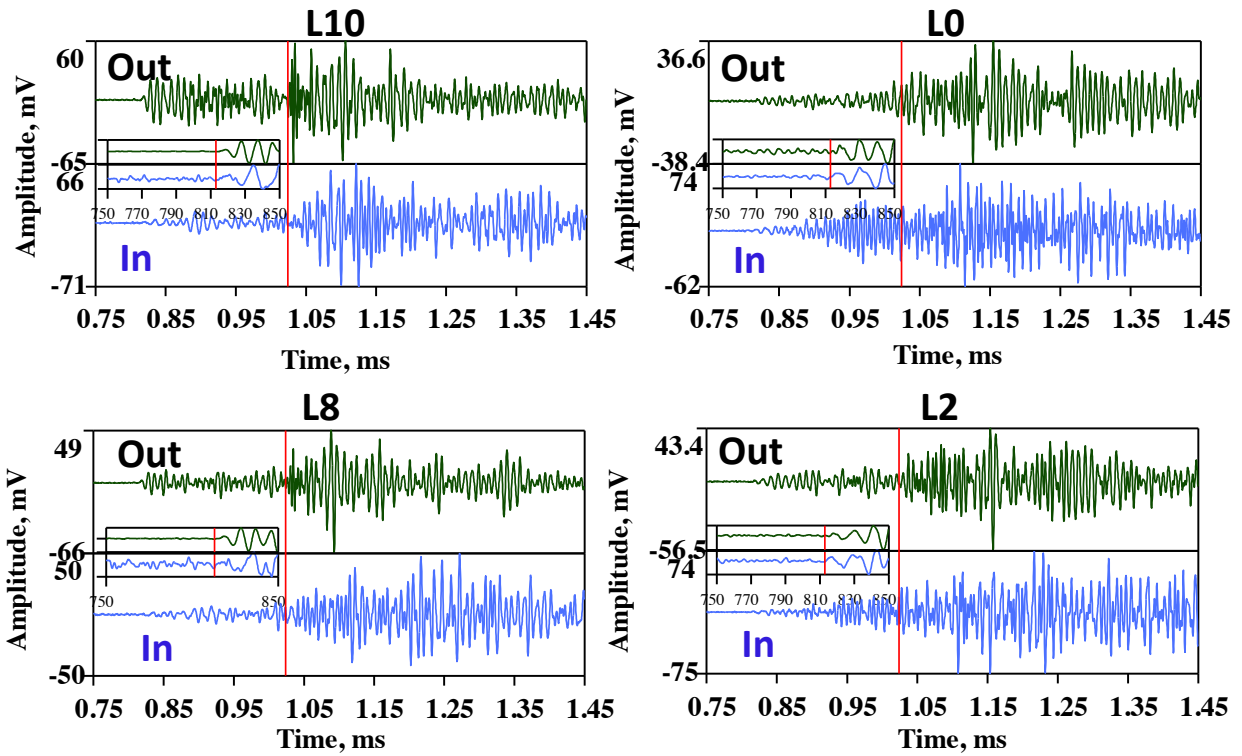


Fig. 14. Comparisons of signals after low-pass 400 kHz from the outside and inside R15 sensors versus end PLBs on different layers.

#### F. Comparisons of the outer and inner sensor FFT results for PLBs on the same layers

The direct comparisons of outer sensor signal FFT results with inner sensor signal FFT results were also done for these same four PLB layers for each sensor type. Figure 15 shows these FFT results for the DW sensor signals shown in Fig. 11. Using above 200 kHz as a comparison frequency range, it is clear for PLBs on layers 10 and 8 that the nearer outer sensor has a larger portion of the signal above this frequency compared to the inner sensor. For PLBs on layers 2 and 0, the nearer inner sensor signal is dominating with a larger portion of the signal above 200 kHz.

Figure 16 provides results for the Mist sensor signals for PLBs on the same set of layers as in Fig. 12. Again using the frequency range above 200 kHz, a single result applies. Namely the nearby sensors have comparatively more signal in this higher frequency range, and the far sensors have less. Due to the strong loss of high frequencies as a result of the couplant the difference is not as large as with the DW sensor signals.

Figures 17 and 18 respectively for the WD and R15 sensors (waveforms respectively in Figs. 13 and 14), also show similar results with respect to higher frequencies. In the case of the WD sensor the results are similar to the DW sensor, and in the case of the R15 sensor the results are similar to those from the couplant-modified Mist sensor, since both (Mist and R15) primarily are sensitive to frequencies below 200 kHz. Thus, as a general conclusion for all four sensor types, the frequency range above 200 kHz has more intensity from the sensor signal on the closer layer to the PLB layer and less from the sensor signals that are farther away from the source PLB layer.

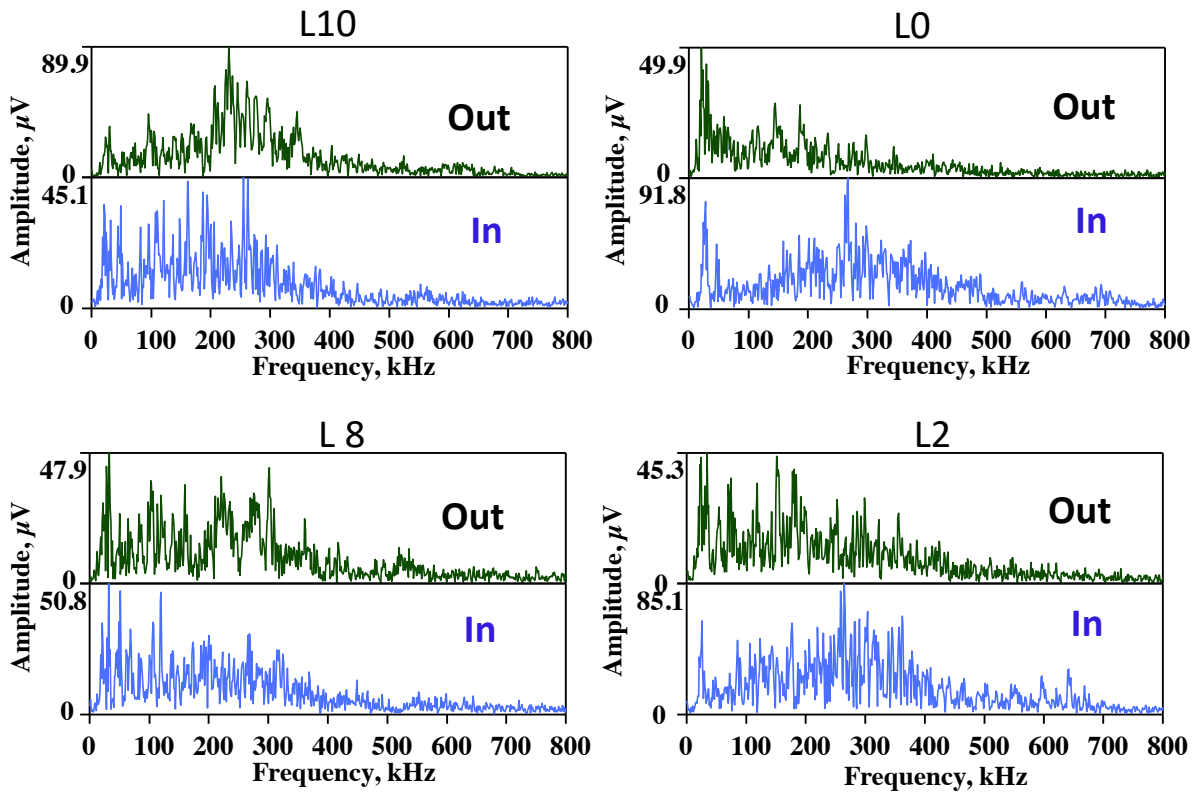


Fig. 15. Comparisons of FFTs of signals from the outside and inside DW sensors versus end PLBs on different layers. Sensor signals shown in Fig. 11.

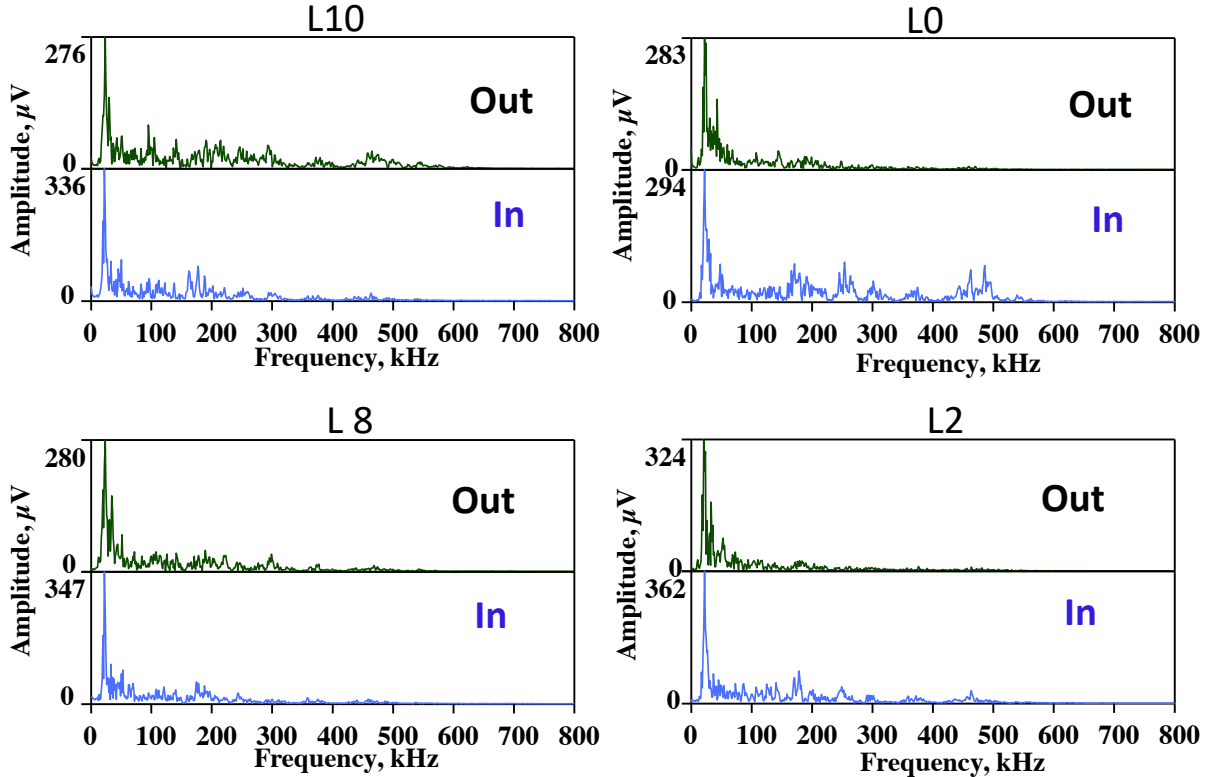


Fig. 16. Comparisons of FFTs of signals from the outside and inside Mist sensors versus end PLBs on different layers. Sensor signals shown in Fig. 12.

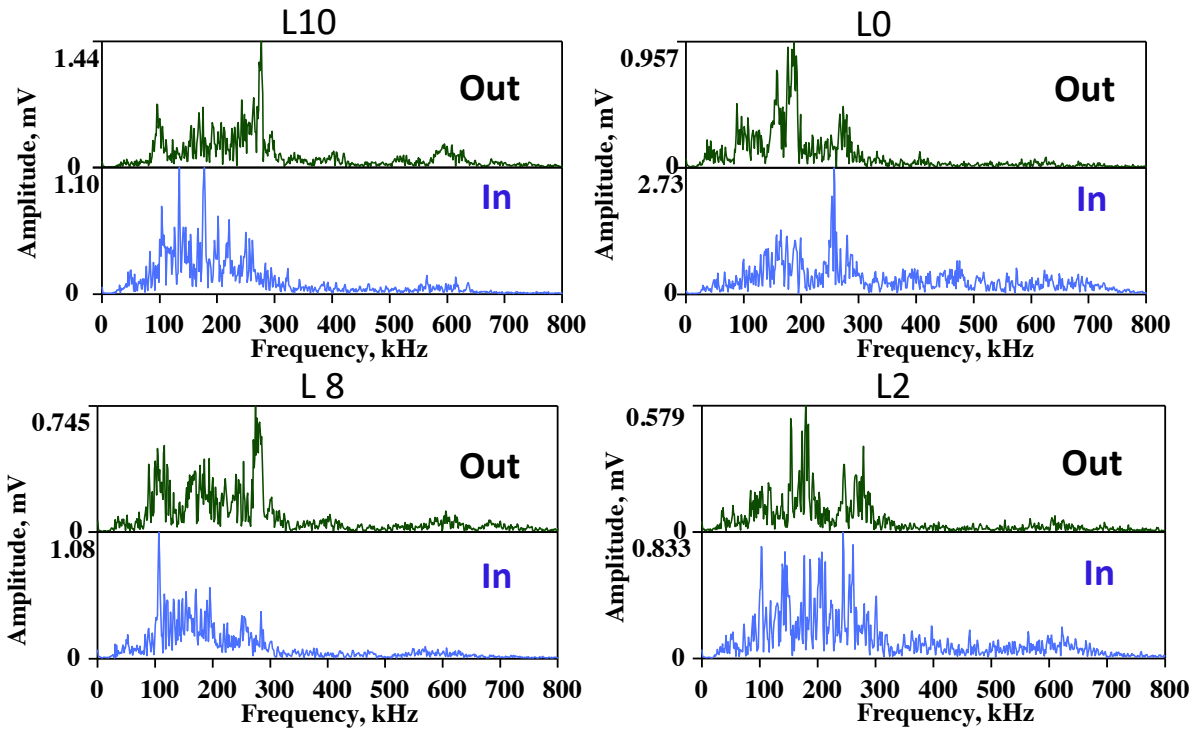


Fig. 17. Comparisons of FFTs of signals from the outside and inside WD sensors versus end PLBs on different layers. Sensor signals shown in Fig. 13.

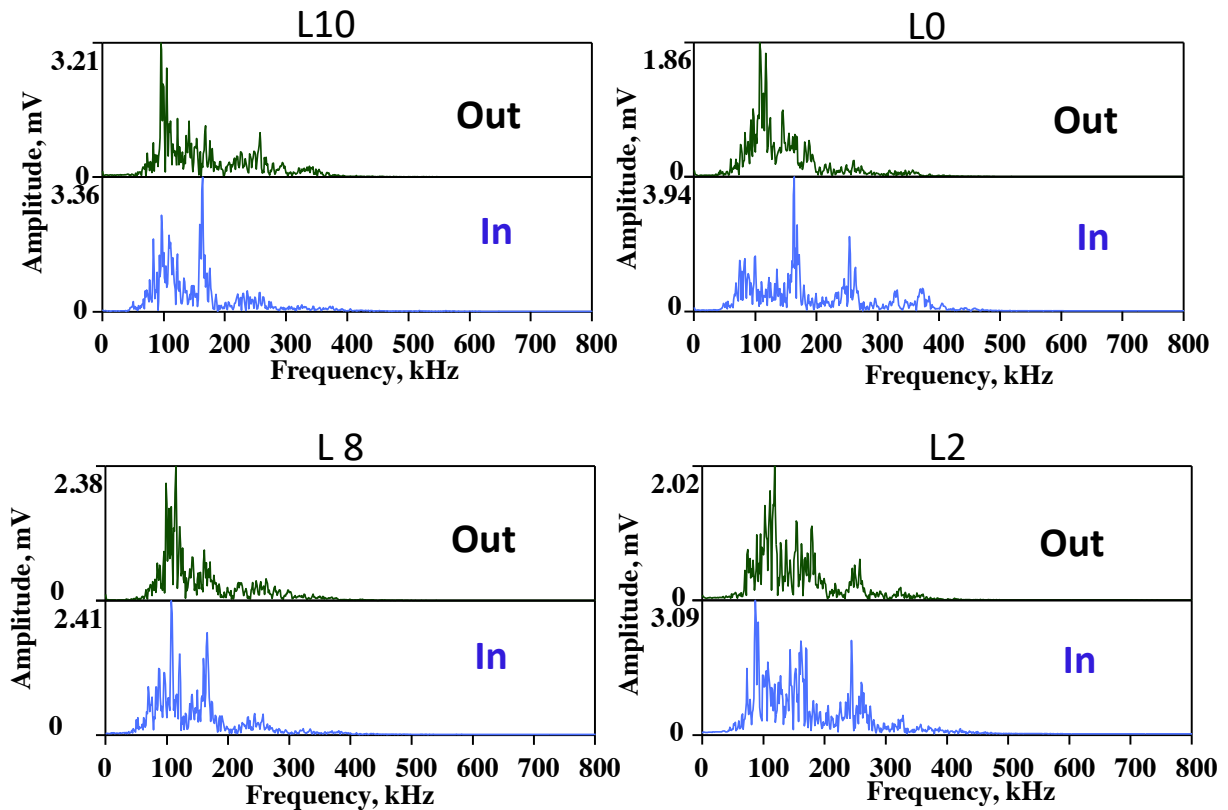


Fig. 18. Comparisons of FFTs of signals from the outside and inside R15 sensors versus end PLBs on different layers. Sensor signals shown in Fig. 14.

### G. Peak amplitudes of outer and inner sensor signals versus the PLB layer

In an application of AE to monitor pressurization of LPVs, it is important that the sensitivity of the outer sensor not be heavily biased toward sources that originate in the outer layers. Thus, an examination of the relative peak amplitude difference of the outer sensor signal was obtained relative to the inner sensor peak amplitude for the same PLB layer. All the peak amplitudes occurred in the flexural region. To provide this comparison the ratios of the peak amplitude of the outer sensor signal to the peak of the inner sensor signal were averaged for five PLBs on each relevant layer and expressed as a dB difference relative to the inner sensor signal. This analysis is not a perfect one, since the thickness is different for the two layers the sensors are mounted on. Thus, as mentioned before, the frequency content will change to the extent there is propagation that is confined to those individual layers. Table 2 provides these results with positive values when the outer sensor peak average is larger than the inner peak average for the different PLB layers and vice versa for negative values. For this table the DW and WD sensor signals were also low pass filtered at 500 kHz to provide a better comparison to the filtered Mist and R15 results. Clearly, the Mist sensor provides the most uniform sensitivity as a function of the PLB layer. This outer sensor varies by at most 2.3 dB (ignoring signs) from the inner one. As mentioned before, this desirable aspect of the Mist sensor signals is due to the loss of higher frequencies as a result of the hot melt glue used for attachment and couplant. The expectation is that, if this sensor was coupled by vacuum grease, the relatively uniform sensitivity would not be maintained. On the other hand the maximum differences for the other three sensors, respectively for the DW, WD and R15 sensor signals, are (ignoring signs) 10.6 dB, 10 dB and 6.3 dB. Thus, except for the Mist sensor, there is a lack of uniform sensitivity in the outer sensor signals as the PLB layer changes.

Table 2. Average peak amplitude of outer sensor with reference to inner sensor peak amplitude.

Layer of PLB/Sensor	DW LP @ 500 kHz, dB	Mist LP @ 500 kHz, dB	WD LP @ 500 kHz, dB	R15 LP @ 400 kHz, dB
10, outer	10.6	-0.2	5.9	-0.9
9	5.5	-1.0	2.2	3.5
8	5.4	1.7	2.9	2.2
2	-5.0	-1.2	-5.8	-3.0
1	-5.8	-2.3	-8.8	-4.6
0, inner	-9.4	-0.1	-10	-6.3

### H. Comparisons of the outer sensor peak amplitude at zero gain for PLBs on different layers

After subtracting the relevant gains from the signals from each sensor/preamp type, the average peak amplitude (five PLBs on each layer) of the different outer sensor signals as a function of the PLB layer was obtained. These results are expressed in  $\text{dB}_{\text{AE}}$  in Table 3. Clearly, except for the Mist sensor, the trend is a decrease in peak amplitude as the PLB moves further below the outer layer where the sensors were mounted. The Mist sensor shows very small changes until the PLB was done on layer 0. For this case there is an unexpected increase in the amplitude. An explanation for this behavior is not apparent. The next to last row of the table provides the difference in peak amplitude from the PLB on layer 10 relative to the value from PLB on layer 0. The large value of 14.1 dB for the DW sensor is due to the high amplitude of the Rayleigh wave for the PLB on layer 10. From PLBs on layers 9 to 0, the difference for the DW sensor is about 8 dB. As a potential measure of relative outer sensor response sensitivity for PLBs on the layers near the inside, the average peak amplitude values for the PLBs on layers 2, 1 and 0 were calculated. The values respectively for the DW, Mist, WD and R15 sensors in  $\text{dB}_{\text{AE}}$  are 42.3, 45.8, 46.1 and 53.1 as shown in the last row of Table 3.

Table 3. Average peak amplitude in dB<sub>AE</sub> for the different outer sensors versus PLB layer.

Layer of PLB/Sensor	DW LP @ 500 kHz, dB <sub>AE</sub>	Mist LP @ 500 kHz, dB <sub>AE</sub>	WD LP @ 500 kHz, dB <sub>AE</sub>	R15 LP @ 400 kHz, dB <sub>AE</sub>
10, outer	56.2	43.6	54.7	55.2
9	50.4	42.8	52.7	56.9
8	50.7	43.6	52.6	57.1
2	42.3	45.6	46.1	55.1
1	42.6	44.7	44.4	53.2
0, inner	42.1	47.0	47.7	51.0
Amplitude peak difference in dB from outer to inner layer PLBs	14.1	-3.4	7.0	4.2
Average peak in dB <sub>AE</sub> for PLBs on layers 2, 1 and 0	42.3	45.8	46.1	53.1

Relative to the approach of using the first arrival of the extensional mode to obtain an arrival time, the average peak amplitude (for five PLBs) for the outer sensor signals was determined for the PLBs on the same set of layers, and it is shown in Table 4. All the determinations of the location in time of the first arrival were done by “eye” when viewing each individual waveform. These results are shown in dB<sub>AE</sub> after correcting the values by the relevant gains of the preamps. The choice of the amplitude to use was based on the amplitude of the first half cycle above the background noise level. This first half cycle amplitude was negative for all the sensor signals. In the case of the DW sensor, the poor S/N ratio only allowed determination of these amplitudes for PLBs on layers 10 and 9, and even in these cases knowing where the arrival was supposed to be in time helped determine a value. Clearly, as with peak amplitude, the Mist sensor provides the most uniform results as the layer of the PLB varies, as can be observed in the next to last row of Table 4. As a potential measure of relative outer sensor response sensitivity for PLBs on the layers near the inside, the average peak amplitude values (first half cycle) for the PLBs on layers 2, 1 and 0 were calculated. The values in the last row are respectively for the Mist, WD and R15 sensors were in dB<sub>AE</sub> 26.7, 20 and 18.7.

Table 4 Average peak amplitude of the first arrival (half cycle peak) of the extensional mode for outer sensor signals

Layer of PLB/Sensor	DW LP @ 500 kHz, dB <sub>AE</sub>	Mist LP @ 500 kHz, dB <sub>AE</sub>	WD LP @ 500 kHz, dB <sub>AE</sub>	R15 LP @ 400 kHz, dB <sub>AE</sub>
10, outer	32.7	30.4	30.3	30.6
9	29.7	29.6	28.9	28.1
8	-	27.5	26.4	24.8
2	-	25.7	21.6	18.0
1	-	26.5	18.0	18.6
0, inner	-	27.9	20.4	19.4
Amplitude peak difference in dB from outer to inner layer	-	2.5	9.9	11.2
Average peak in dB <sub>AE</sub> for PLBs on layers 2, 1 and 0	-	26.7	20	18.7

In order to obtain an estimate of the S/N ratio relative to the peak amplitude (for the flexural region) and the extensional first arrival (half cycle) amplitude for the different sensor/preamps, the time increment from 0 to 750  $\mu$ s (before the signal arrival) was used for the outer sensor signals for 30 different PLBs to obtain a noise estimate. This choice meant that a total time of 22.5 ms was examined. Choosing 30 different cases was expected to provide a more representative value than one for a continuous time period of the same length. Since peak amplitudes of noise are what is important in

choosing an AE threshold, the maximum observed peak amplitude over the 22.5 ms was used. Then, using the respective preamp gains the  $dB_{AE}$  peak noise estimates were obtained. Table 5 shows the noise results in the first row. It should be noted that the noise level for the Mist sensor is a few dB higher due to the noise spikes (previously mentioned) that were not completely eliminated by the low pass filtering.

The S/N examination was based on using the average amplitude for PLBs on the inner layers 2, 1 and 0. From the second row of the table, the S/N ranking can be observed of the average flexural region peak amplitude from highest to lowest to be R15, WD, Mist and DW. The same process was repeated for the average peak amplitude of the first half cycle extensional arrival. The final row of Table 5 shows the extensional S/N ranking from highest to lowest to be R15, WD and Mist. It is important to note that all the values in the last row are negative meaning that a threshold based on the peak noise amplitudes would not have detected the first arrival of this mode for PLBs on the inner layers. Thus, the use of the “eye” technique to determine the location of the time of the first half cycle was a key.

Table 5 Electronic noise peak amplitude estimates for the different sensor/preamps and S/N estimates

Sensor/preamp	DW LP @ 500 kHz	Mist LP @ 500 kHz	WD LP @ 500 kHz	R15 LP @ 400 kHz
Electronic noise level in $dB_{AE}$	35.9	31.6	24.4	22.1
Peak amplitude difference in dB from average peak in flexural region for PLBs on layers 2, 1 and 0	6.4	14.2	21.7	31
Peak amplitude difference in dB from average peak (half-cycle) first extensional arrival for PLBs on layers 2, 1 and 0	-	- 4.9	-4.4	-3.4

*I. Discussion of current results relative possible sensor choices for the potential application of AE monitoring during pressurization of LPVs*

Three aspects need to be discussed: (i) detection of AE signals; (ii) locating AE sources and (iii) identification of the source type of located sources.

(i) In typical AE testing, detection of AE signals fundamentally depends on the amplitude of a particular signal compared to a set voltage threshold. Thus, based on the current S/N results, one might conclude that the best choice is the R15 sensor, but there is another important consideration. That consideration is that sensors mounted on the outer surface should have near equal sensitivity to sources no matter what “level” in the wall thickness the AE source originates. Relative to this requirement, the Mist sensor with the hot melt glue coupling is the best at having the most uniform amplitudes versus the layer region where the source originates.

(ii) With the background view that typically the calculation of a source location depends on the determination of signal arrival times that correspond to the same propagation velocity for each of the sensors in an array of at least three sensors, three location calculation approaches are considered relative to the results of this investigation. First, in typical commercial-service AE testing of pressure vessels the propagation velocity used is the Rayleigh velocity or the close-by shear velocity. Ignoring the possibility of arrival times being obtained from the extensional region before a potential Rayleigh wave arrival, the current results indicate a possible problem in that as the layer of the PLB moved to inner layers the distinct Rayleigh wave/flexural mode arrival no longer appeared in the case of each of the four sensor types. This aspect, due to a loss of higher frequencies transmitting to the outer surface, would result in errors when using the assumption of the mentioned single velocity for the location calculations when the

layer of the AE source changes. Second, another technique used for determination of arrival times at a fixed velocity is to detect the very first arrival of the extensional mode and use that velocity for the calculation of the source location. The current results indicate that three of the four sensor types do have a correspondence of the first arrival with the calculated arrival based on the extensional velocity for all the different PLB layers. Further and more important, when this correspondence was examined in detail, it was found that the background noise level would preclude this determination with the standard approach of using a fixed threshold to determine arrival times. Thus, a more sophisticated approach would be required (discussion of this is beyond the scope of this work) for the detection of the time of the first arrival of this mode. Alternatively, a significant reduction in the propagation distance to the sensors would increase the S/N ratio and potentially allow detection of the first extensional arrival. Third, the cross-correlation technique of determining an arrival time at a fixed frequency of a particular mode is also a possible approach provided the frequency is relatively low so that sources located in the inner layers can be located. This technique does depend on the use of a broadband sensor without strong resonances. For the current considerations that would mean the DW sensor or the Mist sensor, in the latter case depending on the selected correlation frequency alternate coupling may be necessary.

(iii) There are at least two primary AE source types that are present during an AE monitored pressurization of an LPV. These two are crack-tip region sources and friction-based sources at the interfaces between layers. Thus, successful AE testing requires the identification of these two types so that the irrelevant friction events can be eliminated. Friction-based sources tend towards lower frequencies, while crack-tip region sources during an overload beyond the maximum loads of prior cycling have a frequency range that extends to higher frequencies. Testing of LPV steel base material with sharpened cracks demonstrated that crack tip region events during a 10% overload had frequency content well above 200 kHz and up to at least 600 kHz with the same types of broadband sensors used in this study (with vacuum grease coupling), while friction extraneous sources had frequency content below 200 kHz with these same sensors [4]. Since, in the current work, the PLBs on the ends of the lower layers did not produce these higher frequencies at the outer sensors, this frequency distinction between the source type of interest and the source type that is extraneous presents a problem. Potentially, under pressure the frequencies transmitted to the outer surface may show some increase. To determine the increase in higher frequencies transmitted under pressure requires other experiments that are beyond the scope of this work.

## Conclusions

- At the outer sensors, the calculated first arrival of the extensional mode corresponds to the signal arrival for all but one sensor type for all PLB layers. For the calculated flexural mode arrival, only for PLBs on the outer three layers does the actual signal arrival correspond for all the outer sensor types.
- Two outer sensor types (DW and WD) experienced significant loss of higher frequencies for PLBs on layers lower than layer 8, while two types (Mist and R15) that do not have higher frequency sensitivity did not show this significant change.
- As the PLBs moved to the inner layers the peak amplitudes of the outer sensor signals decreased significantly relative to the peak amplitudes of the inner sensors for all the sensor types, except for the couplant/modified Mist sensor.
- In  $\text{dB}_{\text{AE}}$  the average peak amplitudes (flexural region) of the different outer sensor types for PLBs on the inner three layers ranged from 53.1 to 42.3, and for the extensional first arrival from 26.7 to 18.7.
- The background electronic noise levels of the different sensor/preamps varied significantly.
- For PLBs on the inner three layers the S/N ratios of the outer sensors for the peak amplitude and the first half cycle peak amplitude are influenced by the differences in background noise levels of the different sensor/preamps as well as the differences in response of the different sensor types.

- The choice of the appropriate sensor type is not straightforward, as there were significant differences in the signals, frequency content and S/N ratio of the four different sensor types.
- The current results might be considered a lower bound relative to the lack of transfer of higher frequencies to outer-surface mounted sensors. The upper bound being the case of a monotonic wall of the same total thickness. The situation during a pressurization with imperfect interfaces will be somewhere in between and may be “tilted” towards the lower bound as the surfaces with asperity-to-asperity contact will remain imperfect to a large degree. Further, the waves must interact with the imperfect interfaces a very large number of times in the development and propagation of full-thickness Lamb waves to distant sensor positions.

## Acknowledgements

The author gratefully acknowledges project funding, facilities and excellent experimental support, as well as purchasing of sensors and instrumentation, provided by NASA Marshall Space Flight Center, Huntsville, AL, USA.

## References

1. ASTM Standard E569, "Acoustic Emission Monitoring of Structures During Controlled Simulation," 2013 and ASTM Standard E1419, "Examination of Seamless, Gas-Filled, Pressure Vessels Using Acoustic Emission," 2015a, ASTM International, West Conshohocken, PA.
2. Kolsky, H., *Stress Waves in Solids*, Dover, New York, 1963.
3. Wu, Bill S. and Gregory C. McLaskey, “Broadband Calibration of Acoustic Emission and Ultrasonic Sensors from Generalized Ray Theory and Finite Element Models,” *Journal of Nondestructive Evaluation*, Vol. 37, No. 8, pp. 1 – 16, 2018.
4. Hamstad, M. A., personal communications, NIST, Boulder, CO, January 2019.
5. Baltazar, Arturo, Stanislav I. Rokhlin and Claudio Pecorari, “On the Relationship between ultrasonic and Micromechanical Properties of Contacting Rough Surfaces,” *Journal of Mechanical and Physics of Solids*, Vol. 50, pp. 1397 – 1416, 2002.

# Far-field Wave Propagation Signals from Pencil Lead Breaks on the Open End of a Thick-walled Layered Cylinder: Part 2 Modes of wave propagation

**M. A. Hamstad**

Department of Mechanical and Materials Engineering  
University of Denver, Denver, CO 80208, USA

## Abstract

Relative to potential use of acoustic emission (AE) to monitor pressure testing of large steel pressure vessels, in-plane pencil lead breaks (PLBs) were carried out on the open end of a remnant of such a vessel. This remnant had an inner diameter of 58 in. (1473 mm), a wall thickness of 3.3 in. (84 mm) and a total cylindrical length of 125 in. (3175 mm) ending in a head welded to the cylindrical section. The cylindrical section did not have a monotonic wall, but instead it was made of 11 layers (10 at about 0.277 in. [7 mm] thick, and the inside one of about 0.47 in. [11.9 mm] thick) to create a layered pressure vessel (LPV). Due to the presence of the multiple interfaces between layers, a question arose as to whether a sensor mounted on the outer layer was relatively less sensitive and had different frequency content for sources on the inner layers in comparison to sources on the outer layers? The PLB study used four pairs of different types of AE sensors. The sensor types included: i) strong resonance at a single frequency region; ii) multiple resonance frequencies; iii) and iv) broadband response with different frequency responses. Each sensor pair was acoustically coupled, one on the outside surface and one directly below on the inside surface. The sensors were located at 66 in. (1676 mm) (20 times the wall thickness) from the PLB points. This distance was considerably less than the helical path of about 214 in. (5436 mm). Considering PLBs on the ends of the different layers, Part 2 focused on identification of Lamb modes of wave propagation in the AE signals from the four sensor types. In addition, by use of superimposed group velocity curves on frequency versus time results, the peak intensity in the frequency versus time domain for the outside sensor types was studied relative to determination of the presence of dominant full thickness propagation or dominant single layer propagation. For PLBs on the outer most layers, both single layer propagation and full thickness propagation were present in some of the outer sensor signals.

**Keywords:** Thick-walled layered cylinder, pencil lead breaks, four sensor types, inside and outside sensors, acoustic emission wave propagation and Lamb modes

## Introduction

Acoustic emission (AE) testing has been used for many years to monitor testing of pressure vessels as evidenced by ASTM standards (E569 first version 1976 and E1419 first version 1991) [1]. These standards do not specifically address the steel vessel of current interest, namely a vessel made up of layers (11 in this research) of steel rather than a monotonic vessel wall. Several hundred similar layered vessels were fabricated starting in the late 1950's and early 1960's for use by the National Aeronautics and Space Administration (NASA) and other commercial organizations. In the current time frame to more knowledgeably examine AE results from potential pressure testing of such vessels, an important step is to understand the wave propagation of AE-like waves in such a vessel. An opportunity was available to carry out wave propagation studies on a vessel remnant, which had been cut from a large layered pressure vessel (LPV). Thus, the overall goal of the study was to examine pencil lead break (PLB) AE signals in the far field using four different AE sensor types as the layers of the PLBs changed. Besides the uniqueness of the layered construction a further unique aspect was the use of pairs of like AE sensors located back-to-back on the outside and inside of the vessel wall.

In Part 1 of this research, analysis was done of the waveforms and fast Fourier transform (FFT) spectra of the signals received in the far-field at 66 in. (1,676 mm; in this paper, the first listing of units

refers to the actual measured value, if not in S.I. units then the converted units are added), which is 20 times the vessel wall thickness. Four different types of AE sensors were used for in-plane PLBs on the open ends of different layers. As described in Part 1, the large remnant was of sufficient size so that the signals from the direct path could be examined prior to the arrival of the waves from the two helical paths.

In the research reported here in Part 2, the purpose was to determine, for the outer sensor position, the dominant region present in the intensity of frequency versus time data and the possible modes of Lamb wave propagation that were present. An additional goal was to determine if dominant Lamb-wave propagation was full-thickness (like for a monotonic wall) or single-layer propagation for the layer the sensor was mounted on. The variables were: (i) the PLB layer and (ii) sensor type. Four approaches were used. First, the intensity of frequency versus time plots of the signals was examined by use of the Choi Williams distribution (CWD) [2] along with superposition of the appropriate group velocity curves (transformed to frequency versus time for the current propagation distance) as a function of the layer on which the PLB was done and the sensor type. Second, the same CWD data was used to compare the four different sensors types for PLBs on the same layers. This comparison examined the area patterns of the intensity. Third, the waveforms from one sensor with good non-resonant low frequency response were used to compare the phase relationships of the signals for PLBs on layers near the outside and near the inside of the remnant wall. Fourth, the CWD results were considered at the very beginning of the outside sensor signals as a function of the PLB layer. In the application of these approaches, two regions of the signals were examined. The first region was the so-called “extensional region” for the portion of the signal from just before the first arrival of the fundamental extensional mode (lowest symmetric Lamb mode) to an end shortly before the arrival of the fundamental flexural mode (lowest antisymmetric Lamb mode). The second region the so-called “flexural region” added the additional portion of the signal beyond the arrival of the flexural mode to the examination. It is worthwhile to note that the peak amplitudes of the signals were always in the “flexural region.”

### **Group Velocity Curves, Choi Williams Distribution and Experimental Conditions**

The primary required group velocity (GV) curves were calculated using freeware software from Vallen [3]. The GV results are shown in Fig. 1 respectively (left to right) for the outer layer of nominal thickness 0.277 in. (7 mm) and the full nominal thickness of 3.3 in. (84 mm). The thickness values are from the original manufacturing information. Note all the layers except the inner one had this same nominal thickness. The inner layer had a thickness of 0.47 in. (11.9 mm). The properties used for the GV calculations were for steel using the bulk velocities from Kolsky [4] (longitudinal at 5.94 mm/ $\mu$ s and shear 3.22 mm/ $\mu$ s). The group velocity curves are shown to 500 kHz for the smaller thickness (based on a preliminary analysis of frequency versus time results) and 120 kHz for the full nominal wall thickness (also based on a preliminary analysis of frequency versus time results). These limitations on the maximum frequency range facilitate viewing the GV results that correspond to Lamb waves most appropriate for each potential thickness. The modes shown in these figures are limited to those most likely to be present in the signals. When these two thickness cases are compared, it is clear that the frequencies are much lower for the 84 mm case at similar velocities. Further, in the 84 mm case upon approaching 120 kHz, the  $A_0$ ,  $S_0$  and  $A_1$  curves are all becoming asymptotic to the Rayleigh velocity for steel. In contrast, for the 7 mm case at 500 kHz only the  $A_0$  mode is approaching the Rayleigh velocity.

The frequency versus time intensity was obtained by use of Vallen freeware, specifically using the CWD [3]. These calculations were made using the default values for the number of terms in the damping summation and the exponential damping parameter along with choosing of a frequency increment of 1.22 or 2.44 kHz. In addition, the out-of-plane intensity (color scale) of the CWD results used the default 100 % range based on the peak value.

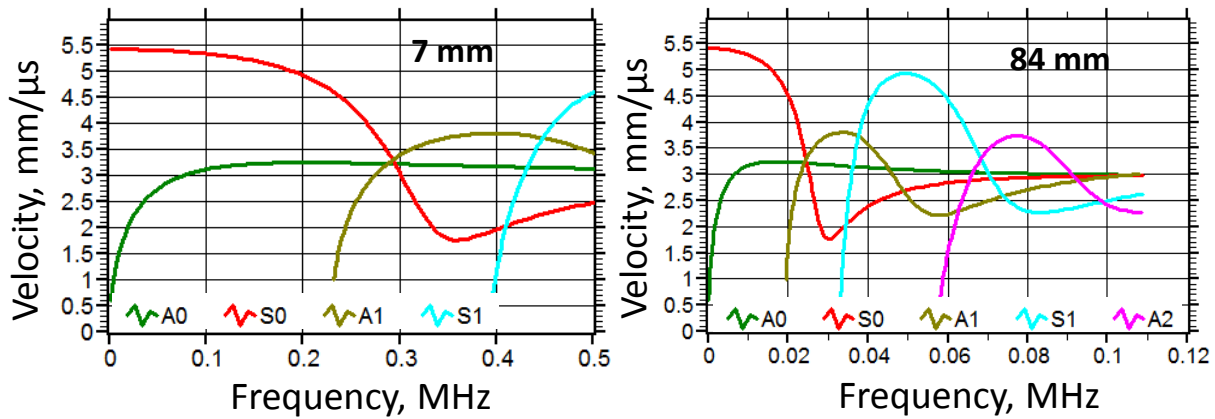


Fig. 1. Group velocities for steel plate thicknesses of 7 mm left and 84 mm right.

The reader of Part 2 is referred to Part 1 [5] for the experimental details including: remnant specimen details, sensor types, layer numbering, trigger sensor (relocated to be very close to the PLB points on the different layers), sensor attachment, instrumentation and acoustic coupling, etc., so as to not unnecessarily repeat this lengthy information. The shorthand notation for the four sensor types remains the same, as used in Part 1: Digital Wave (DW) broadband sensor; Mistras (Mist) broadband sensor; Mistras WD (WD) resonant sensor and Mistras R15 (R15) resonant sensor. Due to unidentified intermittent electromagnetic noise from other activities in the test building, as in Part 1, when certain sensor types were being used, low pass software filtering was used for the Mist and R15 sensor signals respectively at 500 kHz and 400 kHz. This filtering did not alter the key range of frequency response for these sensors. All the original data was taken using a passive high pass filter at 10 kHz.

#### A. Modal examinations by use of the CWD as the PLB layer changes for each sensor type

All the analysis of the sensor signals in Part 2 used the same 700  $\mu\text{s}$  signal increment used in Part 1. For convenience in the multiple steps to import the signals into the CWD software and setting up the computations there, the 700  $\mu\text{s}$  time increment was extracted, and the initial time was set to zero  $\mu\text{s}$ . The key result to keep in mind with this adjustment is that the calculated first arrival times (from Part 1) of the fundamental Lamb modes changed to 63  $\mu\text{s}$  for the extensional mode and 274  $\mu\text{s}$  for the flexural mode. Also, it is important to keep in mind that the initial portion of up to 63  $\mu\text{s}$  represents background noise, and the termination of the signal at 700  $\mu\text{s}$  is about 50  $\mu\text{s}$  before the initial signal arrivals of the two helical paths to the sensors. Note that the peak amplitudes of the signals occurred prior to the end of this 700  $\mu\text{s}$  time increment.

Before specific results for each sensor type are presented, the layout of the pairs of figures, for all the sensor types in this section, needs some explanation. First, since the superposition of the GV curves tends to “hide” the maximum intensity region (red color) when the GV curve closely matches the intensity data, the relevant GV results are shown above (7 mm case) and below (84 mm case) the CWD results. This placement facilitates the reader’s comparisons GVs versus CWD results. In order to align the transformed GV curves in time, an offset time is required. The value selected was based on the following considerations. The 7 mm  $S_0$  mode GV was aligned with the initial intense portion of the CWD result to 500 kHz in the extensional region for the outer DW sensor for a PLB on the end of outer layer 10, which resulted in an offset value of  $-245.2 \mu\text{s}$ . Then, the 11.9 mm  $S_0$  mode GV was aligned with the initial intense portion of the CWD result to 250 kHz in the extensional region for the inner DW sensor for a PLB on the end of inner layer 0, which resulted in a value of  $-246.2 \mu\text{s}$ . The average offset value of  $-245.7 \mu\text{s}$  was used for all cases. This value is very close to the value based on the PLB time, which was  $-246.6 \mu\text{s}$ . Since this value (based on assumed propagation velocities) did not result from an actual comparison with CWD results, it was not used. Figure 2 illustrates (using the selected offset) with the DW sensor the close “fit” of the  $S_0$  mode with the outer sensor for a PLB on layer 10 on the left and a PLB on layer 0 with the DW inner sensor on the

right. Second, the most relevant GV curves are shown in each case as a minimum, and in some cases for reference, some not relevant are shown to demonstrate they are not relevant. Third, the left column in each figure provides frequency results to 120 kHz to more clearly show cases where the intensity at low frequency potentially corresponds to the GVs for 84 mm thickness case. The far-right column provides frequency results to 500 kHz to give a better view of potential correspondence to the GVs for the 7 mm thickness case. Also, the color scale, provided in the figures, shows the range of colors of the out-of-plane intensity. In each case, the peak of the color scale, red color, represents the maximum intensity. Fourth, in the middle column, the waveforms on which the CWD results were based are shown along with vertical red cursors at the calculated first arrival times of the fundamental modes. The PLB layers are also indicated in these waveform plots. Fifth, for each sensor type there is a pair of figures. The first is for a time increment to 260  $\mu\text{s}$  to allow a focus on the “extensional region,” and the second figure for a time increment to 700  $\mu\text{s}$  to provide a focus additionally on the “flexural region.” Sixth, frequencies and time values that are provided in the text and tables were determined from the large size view on the computer monitor. These values were based on results using a computer mouse in conjunction with the software to point to key regions. Seventh, in this section, the focus is on determining the correspondence of the GV mode curves with the most intense portion in frequency and time within the CWD results. Finally, for this section of the paper, all the data is for the outer sensors, since the results for that sensor are of the most importance. The obvious reason is that the outer sensor is the only sensor position that is available in a typical pressure test of an LPV with AE monitoring.

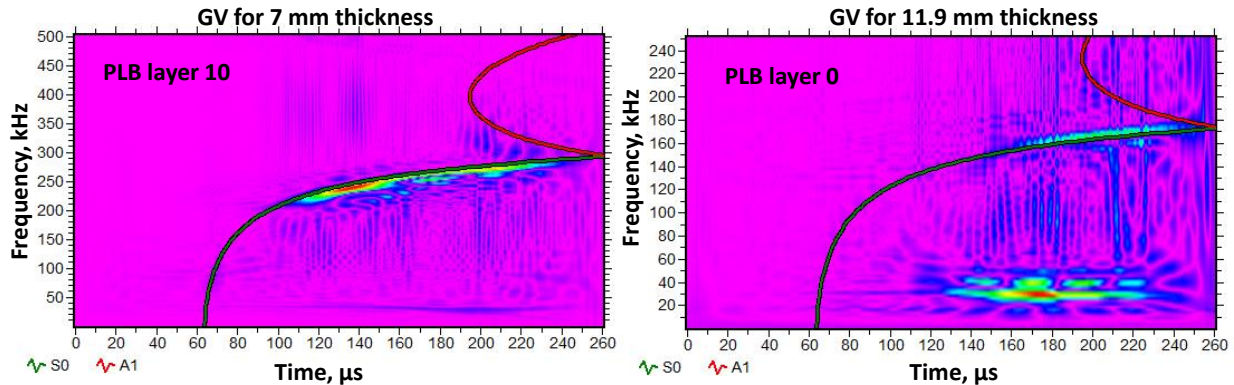


Fig. 2. Illustration of the “fit” of CWD in the intense portion with the  $S_0$  mode for the two relevant GV curves using the outer DW sensor on the left and the inner DW sensor on the right.

#### *i) DW sensor signal CWD results*

In Figs. 3 and 4, the CWD results are shown for the DW sensor signals (note in this paper, as shorthand, “sensor signals” is shortened to “sensor” in some cases). When the DW sensor CWD results are examined in the extensional region (Fig. 3) for the range up to 120 kHz, the most intense region, for all the PLB layer cases, is close to the  $S_0$  mode from the 84 mm GV thickness. The peak intensity arrival time varies for the different layers from about 188  $\mu\text{s}$  to 210  $\mu\text{s}$ . The frequency at the peak intensity varies for the different layers from about 28 kHz to 32 kHz. When the focus for the extensional region changes to a frequency range up to 500 kHz, the layer 10 PLB most intense region corresponds very well to the 7 mm  $S_0$  mode. This long-time region of intensity is above 200 kHz. The peak intensity arrives at about 136  $\mu\text{s}$  with a frequency of about 239 kHz. As the PLB source moves to layers further into the wall thickness, the most intense region moves to the frequencies and arrival times already discussed above for the frequency range to 120 kHz and the 84 mm GVs.

In Fig. 4, when the time range is extended to 700  $\mu\text{s}$  to include the flexural region for the frequency range to 120 kHz, the peak intensity varies from about 100 kHz to 107 kHz for PLBs on layers 10, 8, and 5 (as in Part 1 of this paper, the sequences of layers are numbered as Layer 10 for the outside and Layer 0 for the innermost layer, while the sensor is on the outer surface) corresponding to the 84 mm GVs for the  $A_0$ ,  $S_0$  and  $A_1$  modes as the PLB layer changes. It is worth noting that the frequencies from 100 kHz to 107 kHz may be as high as they are due to some contribution from single layer propagation for 7 mm GVs.

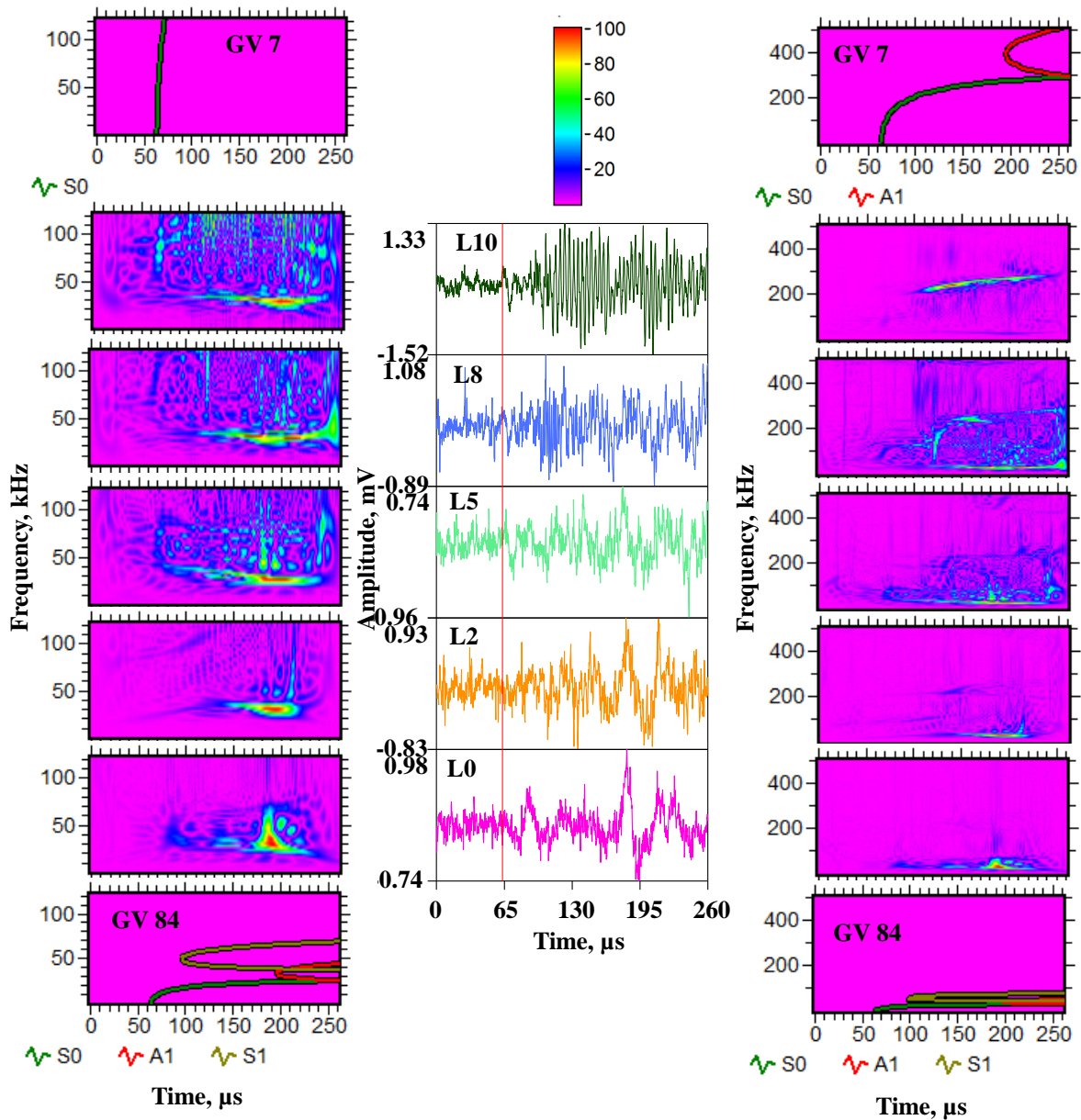


Fig. 3. Shows the CWD results for the DW outer sensor signals for a time increment of 0 to 260  $\mu$ s (extensional region). Left column frequencies to 120 kHz and right column frequencies to 500 kHz. Middle column shows the signals used. GV results for two thicknesses shown.

For the layer 2 PLB, there is no direct match with 84 mm GV modes due to a scatter in the most intense points in the frequency range of about 78 kHz to 120 kHz for the above three modes. In the case of layer 0 PLB, it is clear that the 84 mm  $S_0$  modes corresponds with peak intensity at both 31 kHz and 45 kHz with respective arrival times of about 428  $\mu$ s and 436  $\mu$ s.

When the frequency range for the CWD increases to 500 kHz, it is clear that the peak intensity corresponds to 7 mm  $A_0$  for PLBs on layers 10 and 8 for respective frequencies at about 248 kHz and 254 kHz with arrival times at about 277  $\mu$ s and 280  $\mu$ s. For the PLB on layer 5, the peak intense region drops to about 122 kHz arriving at about 322  $\mu$ s and the modes are for 84 mm GV  $S_0$  and  $A_0$  modes. For PLBs on layers 2 and 0 the comments are the same as for the frequency range to 120 kHz, except that the scattered points for layer 2 PLB cover a frequency range from 156 kHz to 203 kHz. Again the previous comment about the frequencies in the broad 100 kHz range potentially having some contribution from the single layer propagation may apply.

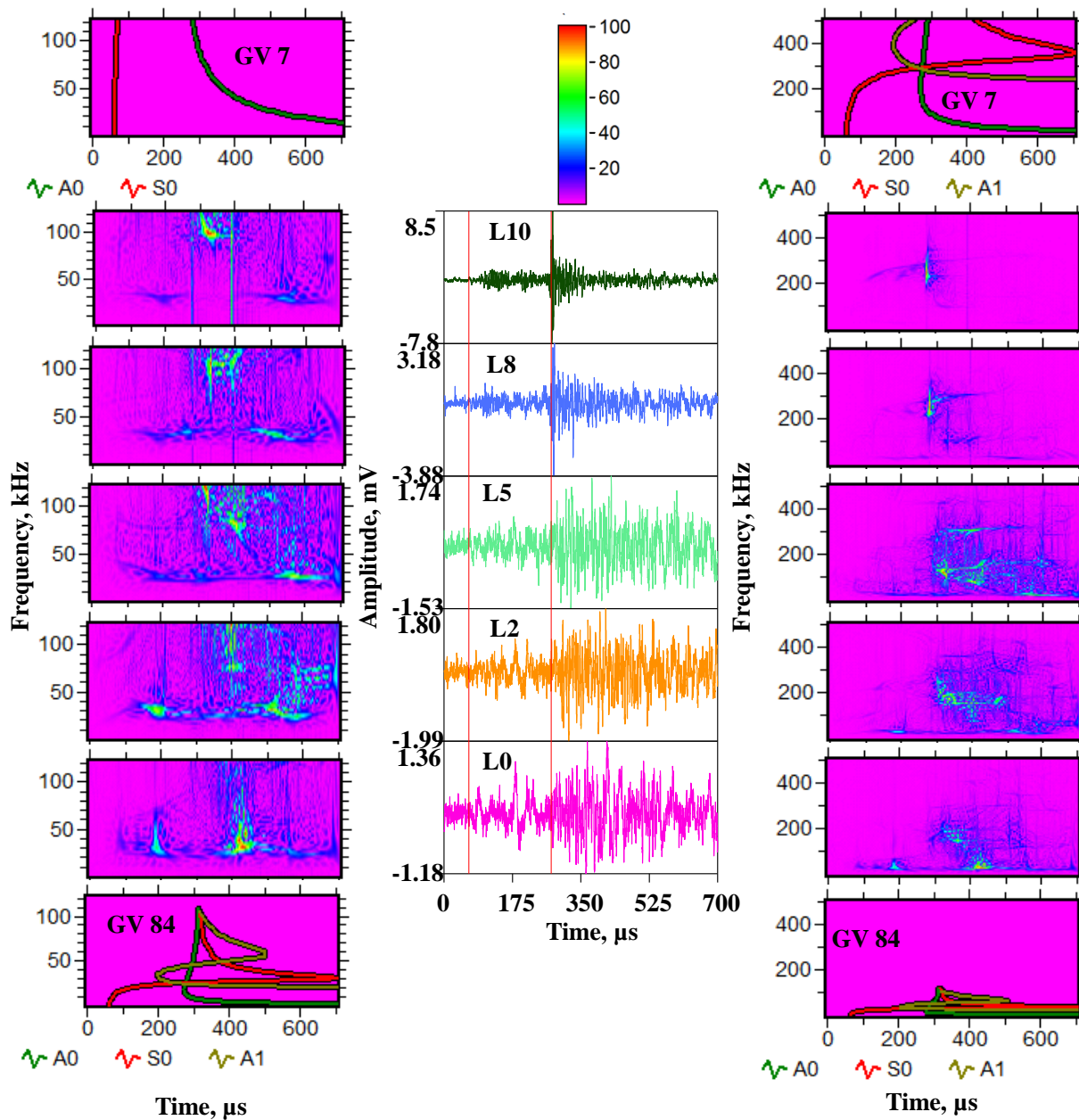


Fig. 4. Shows the CWD results for the DW outer sensor signals for a time increment of 0 to 700  $\mu\text{s}$  (flexural region). Left column frequencies to 120 kHz and right column frequencies to 500 kHz. Middle column shows the signals used. GV results for two thicknesses shown.

#### ii) Mist sensor signal CWD results

Figure 5 provides the CWD results up to 120 kHz for the Mist sensor signals in the extensional region. For this frequency range, the correspondence of the peak intensity is with the 84 mm  $S_0$  mode for PLBs on layers 10, 8, 2 and 0. The frequency range varies from about 26 to 27 kHz with arrival times varying from about 196  $\mu\text{s}$  to 215  $\mu\text{s}$ . In the case of the PLB on layer 5, the peak intensity correspondence is with 84 mm  $S_0$  mode with the peak frequency at about 32 kHz with an earlier arrival time (possibly influenced by the  $S_1$  mode) at about 160  $\mu\text{s}$  as compared to the other layers. When the CWD frequency range is increased to 500 kHz, the most intense region for all the PLB layers continues to be the same as for the 120 kHz results. When the CWD time range is extended in Fig. 6 to include the flexural region, the 84 mm GV modes again dominate for both the 120 kHz and 500 kHz frequency ranges. The peak frequencies are in the range of

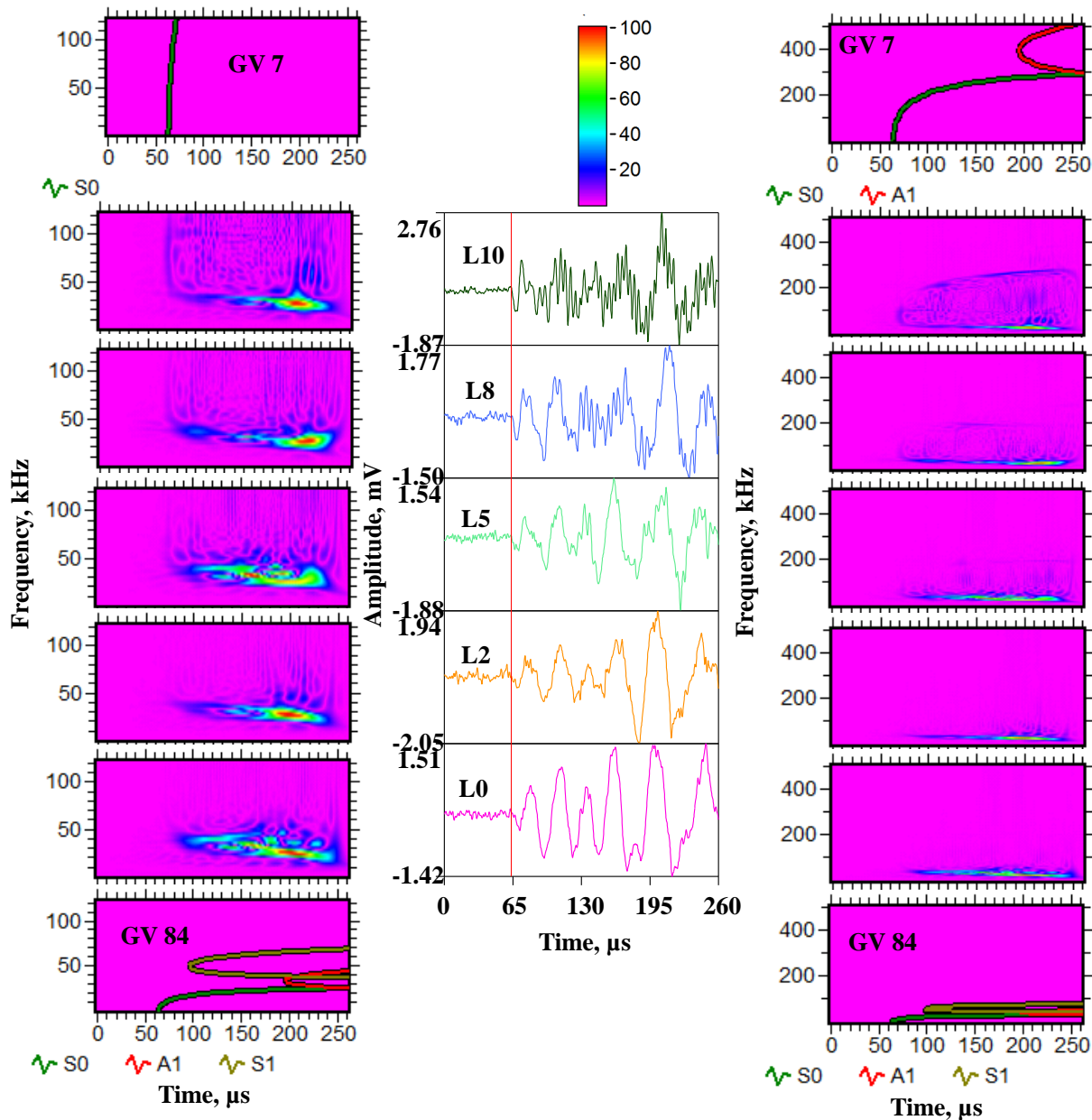


Fig. 5. Shows the CWD results for the Mist outer sensor signals for a time increment of 0 to 260  $\mu\text{s}$  (extensional region). Left column frequencies to 120 kHz and right column frequencies to 500 kHz. Middle column shows the signals used. GV results for two thicknesses shown.

24 to 32 kHz, and the arrival times of these peaks varied from 571 to 619  $\mu\text{s}$  (well into the flexural region) for layers 10, 8, 5 and 2 PLBs. The mode is  $S_0$  for these layers. For layer 0 PLB, the peak time is earlier at about 426  $\mu\text{s}$ , and the modes seem to be a combination of  $S_0$ ,  $A_1$  and  $S_1$  with a peak frequency of about 32 kHz. As was pointed out in Part 1, the dominance of low frequencies for the Mist sensor is a result of the use of hot melt glue to couple the sensor, which resulted in significant attenuation of the higher frequencies prior to reaching the sensor's sensing element.

### iii) WD sensor signal CWD results

In the case of the WD sensor, due to the resonant behavior, only limited CWD peak intensity matches to the GV curves were observed. Figure 7 shows the results for the extensional region. For the CWD frequency range up to 120 kHz, there are no clear matches of the CWD intensity and the GV curves.

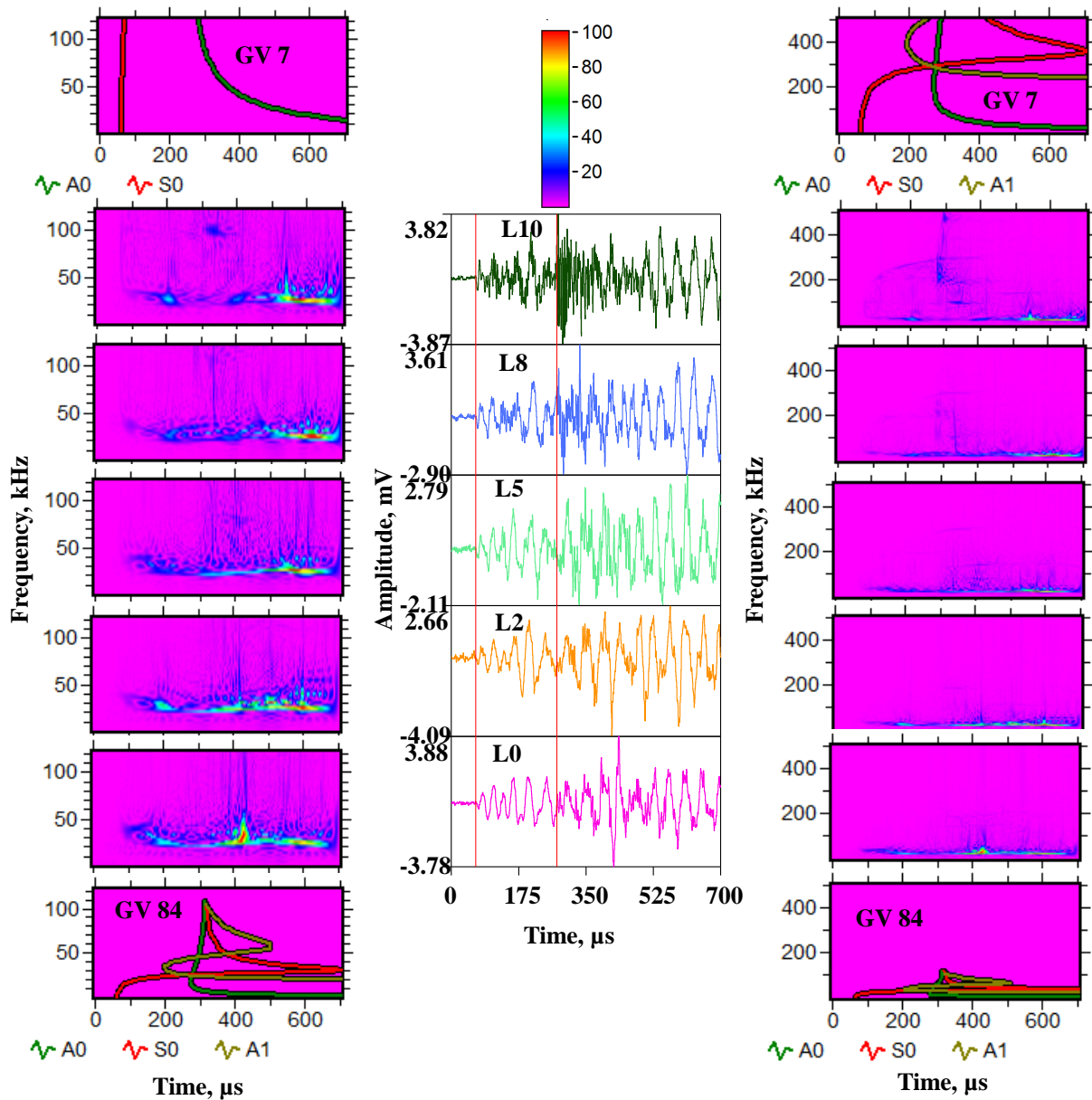


Fig. 6. Shows the CWD distribution results for the Mist outer sensor signals for a time increment of 0 to 700  $\mu\text{s}$  (flexural region). Left column for frequencies to 120 kHz and right column for frequencies to 500 kHz. Middle column shows the signals used. GV results for two thicknesses shown.

When the frequency range was expanded to 500 kHz, a correspondence of the peak intensity was found for 7 mm  $S_0$  mode at a peak frequency of about 269 kHz for layer 10 PLB with an arrival time of 203  $\mu\text{s}$ .

For the other PLB layers no clear matches were found. Upon expansion of the time range (0 to 700  $\mu\text{s}$ ) to include the flexural region, as shown in Fig. 8, there seems to be correspondence of the GV curves with the peak intensity regions for the PLBs on layers 10 and 8 in the CWD results up to 120 kHz for 84 mm where modes  $A_1$  and  $A_2$  cross each other at frequencies of about 100 kHz and 107 kHz with respective times of 344  $\mu\text{s}$  and 335  $\mu\text{s}$ . For PLBs on layers 5, 2 and 0 the peak intensities are in the 84 mm GV region, but there are no apparent matches of the CWD peak intensity to the GV curves.

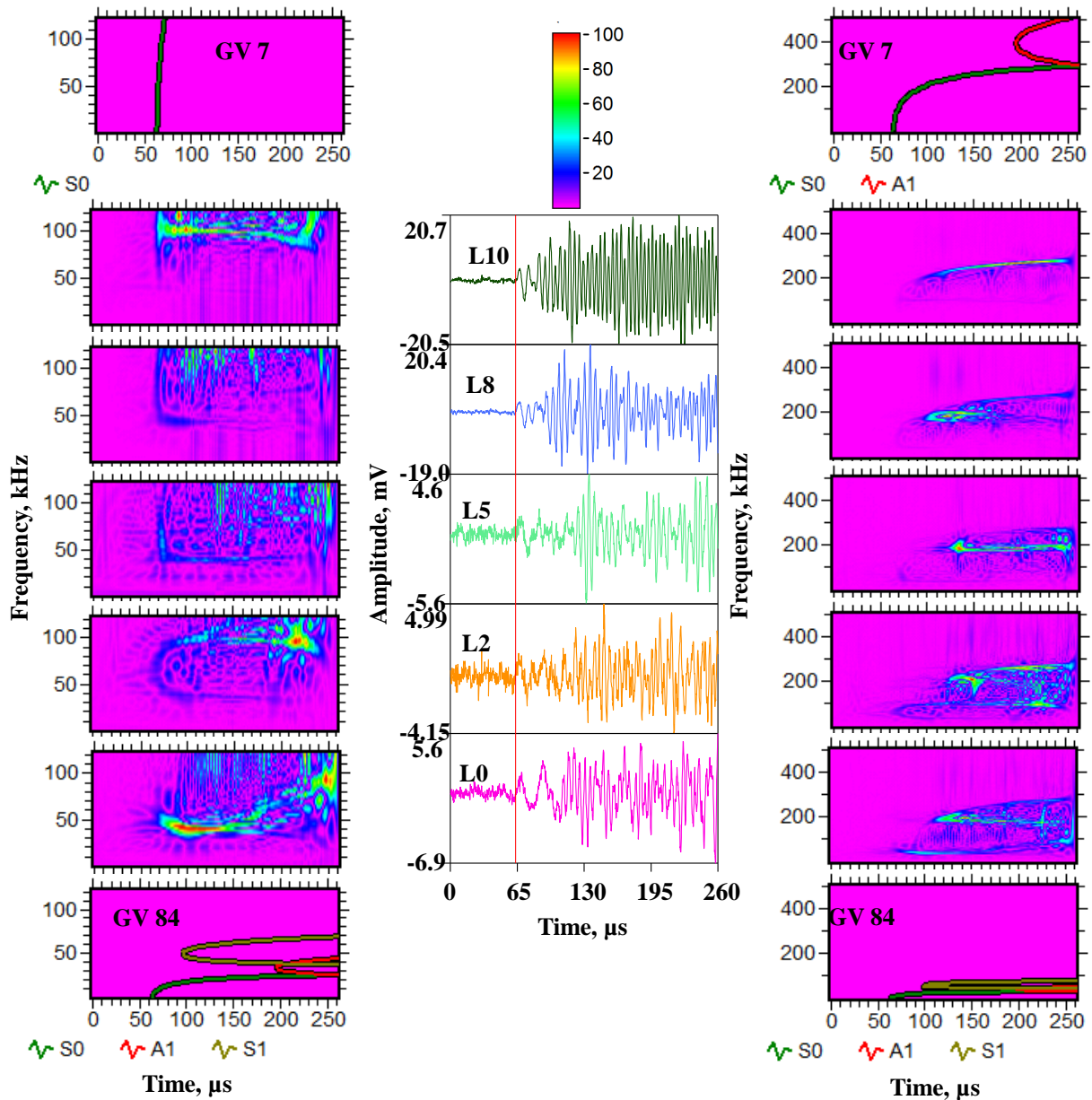


Fig. 7. Shows the CWD results for the WD outer sensor signals for a time increment of 0 to 260  $\mu\text{s}$  (extensional region). Left column frequencies to 120 kHz and right column frequencies to 500 kHz. Middle column shows the signals used. GV results for two thicknesses shown.

When the CWD results in the flexural region are expanded to 500 kHz, there is close correspondence of peak intensity for layer 10 PLB where modes  $A_0$  and  $A_1$  cross each other for the 7 mm GV curves. The peak frequency and time is 278 kHz and 281  $\mu\text{s}$ . For layer 8 PLB there is a potential correspondence to 7 mm GVs with a peak frequency of 283 kHz between the close-by  $S_0$  and  $A_1$  curves at a time of about 337  $\mu\text{s}$ . When the PLBs are on the ends of layers 5, 2 and 0, the intense peaks are approximately in the range of 178 to 186 kHz. These are above the frequencies of the 84 mm GV modes, but they do not match the 7 mm modes. In summary, for this resonant sensor, the matches that were observed may be happenstances of sensor resonant frequency ranges corresponding to certain intense modal regions for the current thicknesses, but these matches may not be present for these modes when other thicknesses are present.

#### iv) R15 sensor signal CWD results

Figure 9 shows the CWD results for the R15 sensor in the extensional region up to 260  $\mu\text{s}$ . There does not seem to be any matches for the CWD intense regions and the GVs for either thickness 7 mm or 84 mm

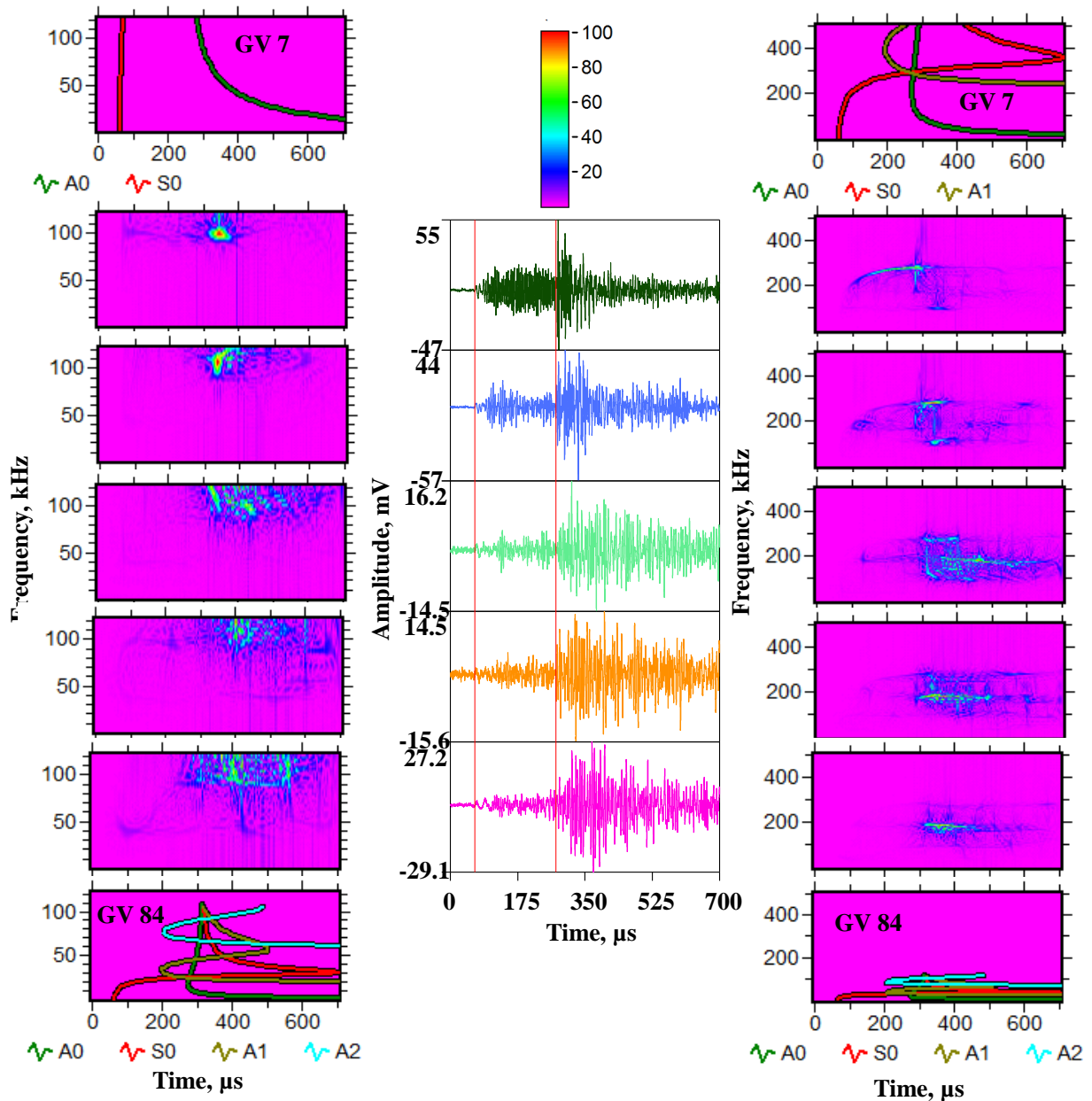


Fig. 8. Shows the CWD distribution results for the WD outer sensor signals for a time increment of 0 to 700  $\mu\text{s}$  (flexural region). Left column for frequencies to 120 kHz and right column for frequencies to 500 kHz. Middle column shows the signals used. GV results for two thicknesses shown.

and for either frequency range to 120 kHz or to 500 kHz. This result is not unexpected, since this sensor has a relatively strong resonance at about 150 kHz, according to the manufacturer. The interesting fact is that all the peak intensity frequencies occur in the frequency range of about 101 to 127 kHz (checked by expanding the frequency range to 150 kHz), which is below the manufacturer's value. The time range of the peak frequencies varies over a wide range from 112  $\mu\text{s}$  to 245  $\mu\text{s}$ . Likewise, in Fig. 10, when the time increment is increased to 700  $\mu\text{s}$  to include the flexural region, even when both CWD frequency ranges are considered, only one correspondence was found for PLBs on layer 5. In this case, the GVs for 84 mm and modes  $A_0$  and  $S_0$  matched the peak intensity for both CWD frequency ranges at about 117 kHz and a time of 338  $\mu\text{s}$ . For the PLB layers 18, 8, 2 and 0, the peak frequencies ranged from 101 kHz to 112 kHz with no matches to GV curves.

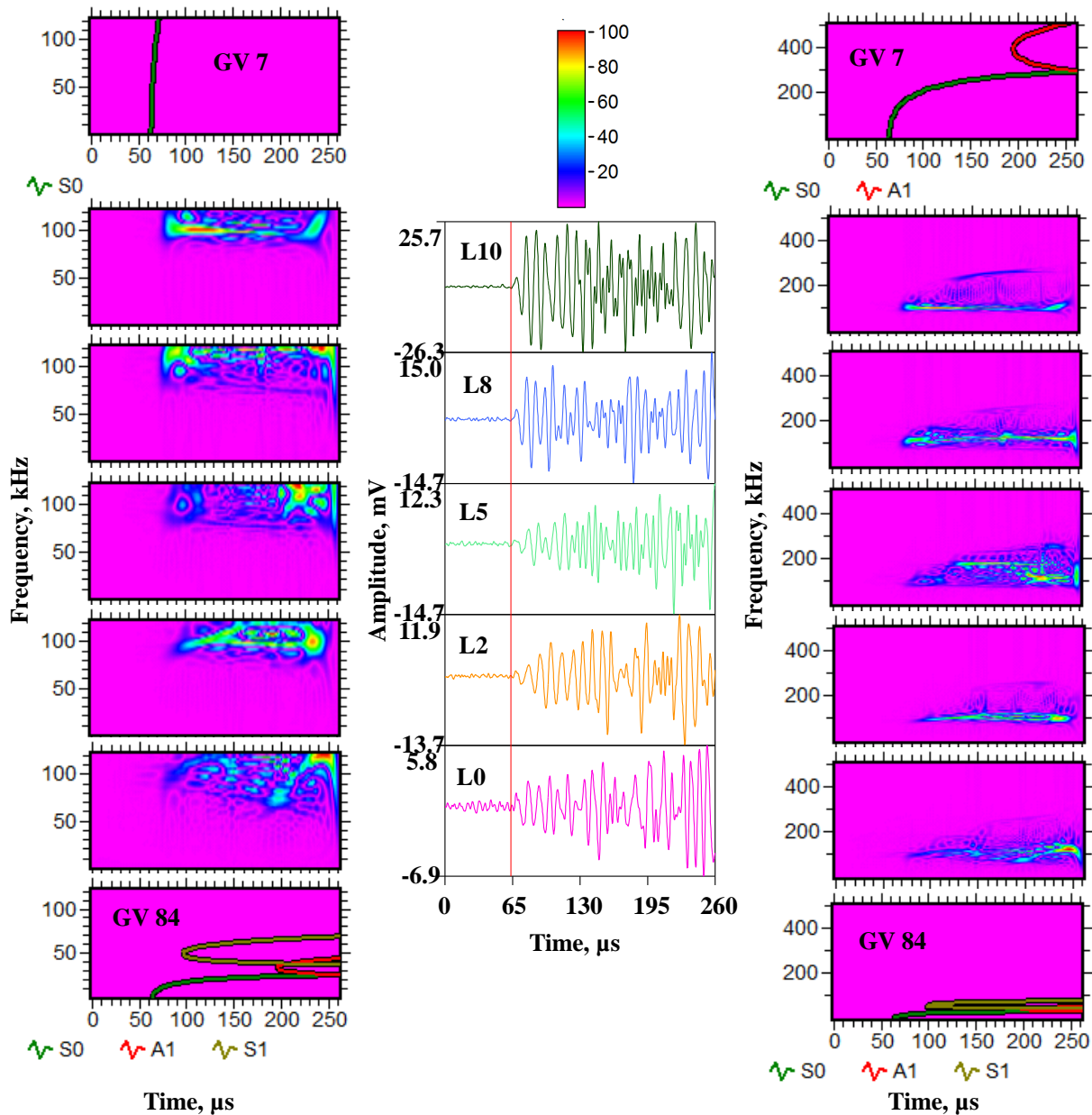


Fig. 9. Shows the CWD results for the R15 outer sensor signals for a time increment of 0 to 260  $\mu$ s (extensional region). Left column frequencies to 120 kHz and right column frequencies to 500 kHz. Middle column shows the signals used. GV results for two thicknesses shown.

To provide the reader with a convenient summary of the CWD peak intensity data for the different sensors and the different PLB layers, two tables are provided. Each “cell” of these tables shows consecutively the most intense frequency, the arrival time of that most intense frequency and, where applicable, the thickness in mm and GV mode(s) that reasonably correspond to that peak intensity. Table 1 shows the CWD peak intensity results for the ranges to 120 kHz and 500 kHz for the extensional region. Table 2 shows the CWD peak intensity results for the ranges to 120 kHz and 500 kHz for the extensional region and flexural region signals.

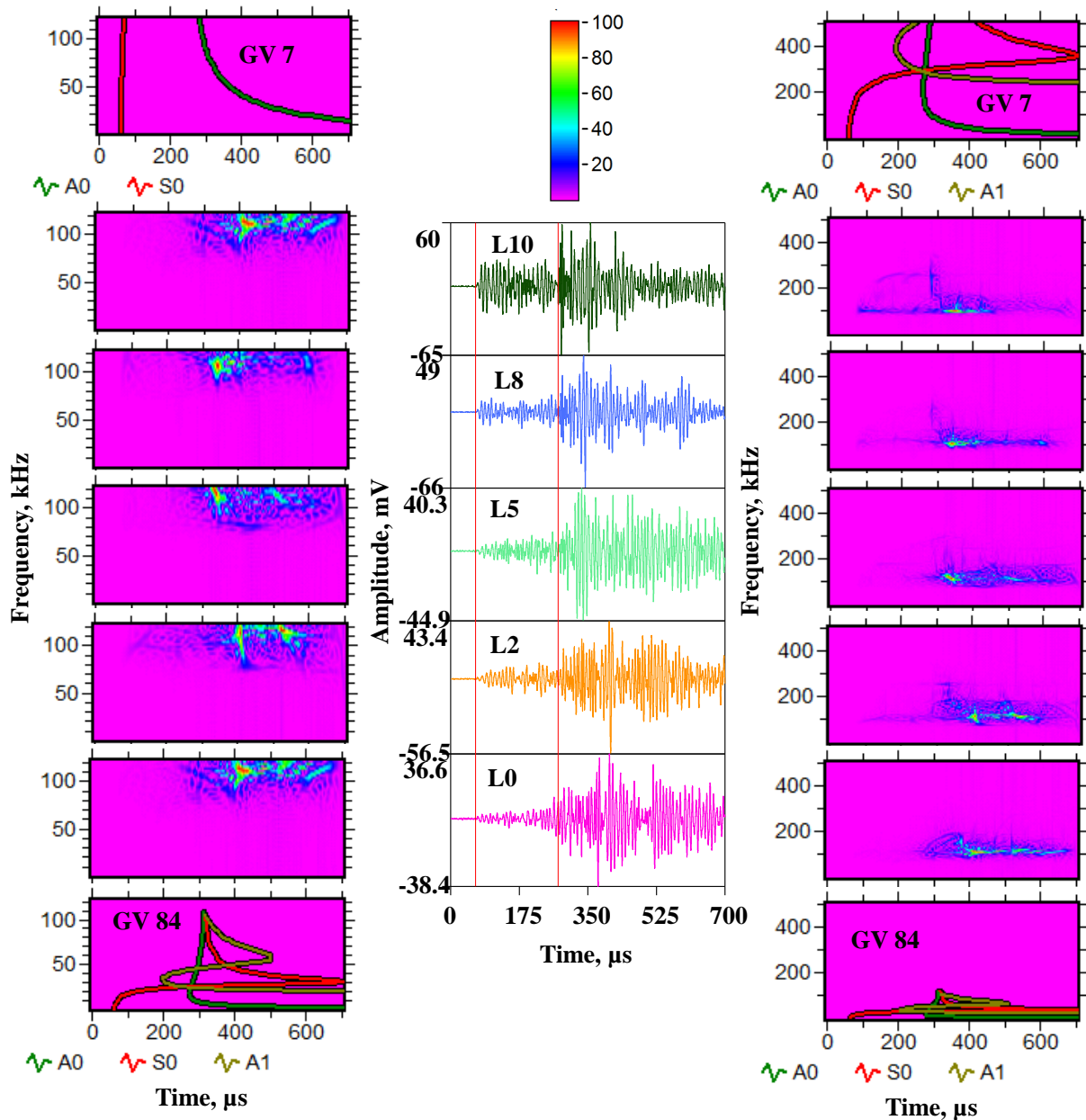


Fig. 10. Shows the CWD distribution results for the R15 outer sensor signals for a time increment of 0 to 700  $\mu\text{s}$  (flexural region). Left column for frequencies to 120 kHz and right column for frequencies to 500 kHz. Middle column shows the signals used. GV results for two thicknesses shown.

From the two tables, the general trend for both broadband sensors was most often correspondence of the highest intensity CWD results with the GVs for the 84 mm full-thickness propagation in both the extensional and flexural regions for all the PLB layers and the two CWD frequency ranges. This result applied to all 20 cases for the Mist sensor. The exceptions for the DW sensor were for PLBs on the outer layers 10 and 8 (only layer 10 in the extensional region). In these cases, the peak intensity CWD correspondence in both the extensional and flexural regions was to the 7 mm GVs when the frequency range was extended to 500 kHz. The general results for the WD and R15 sensors were no correspondence of the intense CWD results and the GV curves. Exceptions for the WD sensor were for PLBs on layers 10 and 8 (only layer 10 in the extensional region). The only peak CWD intensity correspondence for the R15 sensor was in the flexural region for a PLB on layer 5 in the flexural region.

Table 1 Most intense frequency, arrival time and mode(s) in extensional region 0 to 260  $\mu$ s

Frequency range, kHz	PLB layer and sensor	DW: frequency, kHz; time $\mu$ s; GV thickness, mm and mode(s)	Mist: frequency, kHz; time $\mu$ s; GV thickness, mm and mode(s)	WD: frequency, kHz; time $\mu$ s; GV thickness, mm and mode(s)	R15: frequency, kHz; time $\mu$ s; GV thickness, mm and mode(s)
0 to 120	10	29, 197, 84: S <sub>0</sub>	27, 205, 84: S <sub>0</sub>	101, 99, No match	101, 112, No match
	8	28, 210, 84: S <sub>0</sub>	26, 215, 84: S <sub>0</sub>	118, 131, No match	121, 243, No match
	5	28, 195, 84: S <sub>0</sub>	32, 160, 84: S <sub>0</sub>	120, 250, No match	121, 218, No match
	2	32, 188, 84: S <sub>0</sub>	27, 198, 84: S <sub>0</sub>	98, 217, No match	107, 191, No match
	0	29, 190, 84: S <sub>0</sub>	26, 196, 84: S <sub>0</sub>	42, 94, No match	121, 245, No match
0 to 500	10	239, 136, 7: S <sub>0</sub>	27, 205, 84: S <sub>0</sub>	269, 203, 7: S <sub>0</sub>	101, 112, No match
	8	28, 210, 84: S <sub>0</sub>	26, 215, 84: S <sub>0</sub>	183, 121, No match	127, 180, No match
	5	28, 195, 84: S <sub>0</sub>	32, 160, 84: S <sub>0</sub>	186, 134, No match	121, 218, No match
	2	32, 188, 84: S <sub>0</sub>	27, 198, 84: S <sub>0</sub>	212, 147, No match	107, 191, No match
	0	29, 190, 84: S <sub>0</sub>	26, 196, 84: S <sub>0</sub>	195, 143, No match	123, 245, No match

Table 2 Most intense frequency, arrival time and mode(s) in flexural region 0 to 700  $\mu$ s

Frequency range, kHz	PLB layer and sensor	DW: frequency, kHz; time $\mu$ s; GV thickness, mm and mode(s)	Mist: frequency, kHz; time $\mu$ s; GV thickness, mm and mode(s)	WD: frequency, kHz; time $\mu$ s; GV thickness, mm and mode(s)	R15: frequency, kHz; time $\mu$ s; GV thickness, mm and mode(s)
0 to 120	10	100, 325, 84: S <sub>0</sub> , A <sub>0</sub>	24, 581, 84: S <sub>0</sub>	100, 344, 84: A <sub>1</sub> , A <sub>2</sub>	101, 349, No match
	8	107, 331, 84: A <sub>0</sub> , A <sub>1</sub>	24, 612, 84: S <sub>0</sub>	107, 335, 84: A <sub>1</sub> , A <sub>2</sub>	107, 342, No match
	5	100, 322, 84: S <sub>0</sub> , A <sub>0</sub>	27, 571, 84: S <sub>0</sub>	120, 422, No match	117, 338, 84: A <sub>0</sub> , S <sub>0</sub>
	2	78 to 120, scattered in time	24, 593, 84: S <sub>0</sub>	117, 401, No match	112, 329, No match
	0	31 and 45, 428 and 436, 84: S <sub>0</sub>	32, 426, 84: S <sub>0</sub> , A <sub>1</sub> , S <sub>1</sub>	109, 486, No match	112, 407, No match
0 to 500	10	248, 277, 7: A <sub>0</sub>	24, 612, 84: S <sub>0</sub>	278, 281, 7: A <sub>0</sub> , A <sub>1</sub>	101, 349, No match
	8	254, 280, 7: A <sub>0</sub>	24, 619, 84: S <sub>0</sub>	283, 337, 7: S <sub>0</sub> , A <sub>1</sub>	107, 342, No match
	5	122, 322, 84: S <sub>0</sub> , A <sub>0</sub>	27, 612, 84: S <sub>0</sub>	178, 458, No match	117, 338, 84: A <sub>0</sub> , S <sub>0</sub>
	2	156 to 203, scattered in time	24, 593, 84: S <sub>0</sub>	183, 324, No match	112, 407, No match
	0	31 and 45, 428 and 436, 84: S <sub>0</sub>	32, 426, 84: S <sub>0</sub> , A <sub>1</sub> , S <sub>1</sub>	186, 383, No match	112, 421, No match

*B. Comparisons of sensor types based on CWD area-patterns of intensity for PLBs on the exposed end of the same layer*

To provide input as to how all the various intense frequency(s) and time(s) area-patterns relate to each other as a function of the sensor type for PLBs on a single layer at a time, Figs. 11 and 12 were created. These figures used the same CWD results for the outer sensors presented in Figs. 3 through 10 arranged in a different fashion. The layout in these figures is as follows. Figure 11 has the results for the extensional region time from 0 to 260  $\mu$ s for both frequency ranges, and Fig. 12 has the results for the time from 0 to

700  $\mu$ s to include the flexural region for both frequency ranges. In both figures, the top four rows include all four sensor types for the CWD results over the range to 120 kHz, and the bottom four rows include all four sensor types for the CWD results to 500 kHz. Also, in both figures, the PLB layers are in columns from left to right labeled 10, 8, 5 and 0. The CWD results for layer 2 were not included as they did not appreciably add to the sequence of layer-related changes as the PLB source moved from layer 5 to the inner layer 0. Again, the analysis of the results in these figures is centered on area-patterns of the intensity within the frequency versus time results, not the peak intensity, since that was already covered in section A. Further, since area-patterns are the key emphasis, the specific modes are not discussed. It is noted that area-patterns of intensity in frequency versus time results can relate to certain source characteristics (for example rise time [6] with broadband sensors).

From an overall perspective, several results are apparent when the potential area-patterns of intensity in the CWD results are examined for PLBs on a single layer at a time and comparisons of the results are made for the four sensor types. This overall discussion is divided into two parts, first for the extensional region (Fig. 11) and then for the flexural region (Fig. 12).

In the following the comparisons are between the two broadband sensors and between the two resonant sensors. The discussion starts in the extensional region with the frequency of the CWD results limited to 120 kHz, so as to focus on the primary region of GV curves for the full thickness propagation. The results show the broadband sensors do not have similar area-patterns individually by layer for PLBs on layers 10, 8 and 5. In the area-patterns for these layers, the DW results show intensity at higher frequencies not present with the Mist sensor. Both sensors do have intensity at similar low frequencies. Only for PLBs on layer 0 do the intensity area-patterns remain reasonably the same for both sensors. For the resonant sensors in the extensional region to 120 kHz, the two sensors have similar area-intensity patterns only for PLBs on layer 10. For the other three layers, the pattern differs, although both have similar higher frequency regions. The R15 sensor lacks the low frequency region of the WD that increases in intensity as the PLB layer moves from 8 to 0. When the frequency range in the extensional region expands to 500 kHz, the broadband sensors only have matching area-patterns of intensity for PLBs on layers 10 and 0. For the in-between PLBs on layers 8 and 5, the Mist sensor lacks a higher frequency region present in the DW result. In the case of the resonant sensors for this case, there does not seem to be any clear area-pattern matches.

Turning to the flexural region (Fig. 12) and again starting with the maximum frequency to 120 kHz, the broadband sensors are considered first. The area-pattern match is present for PLBs on layers 10 and 8, but the relative intensity of the intense areas varies between the two different broadband sensors for PLBs on these layers. For the other two PLB layers 5 and 0, the pattern similarity is not present due to the DW sensor having a higher frequency region not present with the Mist sensor. When the results for the resonant sensors are compared as a function of the PLB layer for the 120 kHz range, there is some reasonable area-pattern similarity for PLBs on layers 5 and 0. For PLBs on layers 10 and 8, the WD sensor does not have the extended in time intensity region that is present in the R15 case. After extending the frequency range to 500 kHz in the flexural region, the broadband sensors have areas that result in a pattern match for layer 8 PLB with relative intensity differences in the two sensor results. For PLBs on layers 5 and 0, due to the high frequency region in the case of the DW sensor and lower frequency regions for the Mist sensor, there are no area-pattern matches. In the case of the resonant sensors, there are relatively poor area-pattern matches for PLBs on layers 8, 5 and 0. Only for PLBs on layer 10 do the areas have some common intense regions in the results for these two sensors.

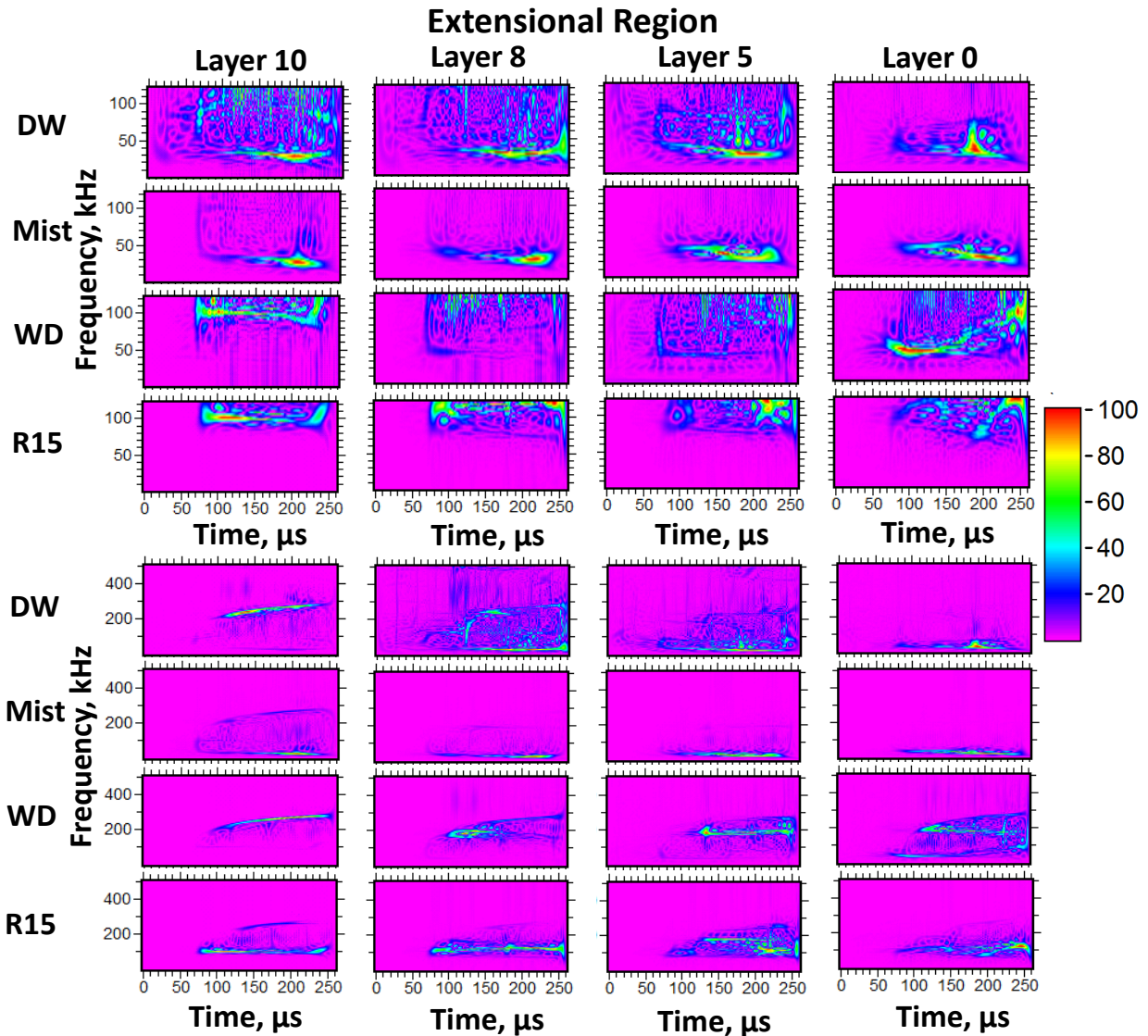


Fig. 11. For the extensional region (0 to 260  $\mu$ s), the CWD results are shown in columns for PLBs on layers 10, 8, 5 and 0 for the four sensor types as labeled on the left for the frequency to 120 kHz in the top four rows. The bottom four rows show the same arrangement of information when the frequency is extended to 500 kHz. A color scale of intensity is shown on the right side.

To provide an explicit summary of the area-pattern similarities in each region, two tables are presented. Table 3 shows both frequency regions of the extensional part, and Table 4 shows for the flexural part of both frequency regions. In the tables, PS stands for area-pattern similarity and IS for incomplete area-pattern similarity. For the broadband sensors, a total of seven area-pattern matches of the CWD results were found. Overall the lack of area-pattern matches (total of 9 out of a possible 16) for the broadband sensors is driven by the relatively higher frequency response of the DW sensor and the relatively lower frequency response of the Mist sensor as a result of the couplant used. If vacuum grease or an equivalent had been used, it is likely that the Mist and DW would be much more similar in all the regions considered. Overall for the resonant sensors, the four area-pattern matches (out of a possible total of 16) were limited by the differences in their resonant frequencies.

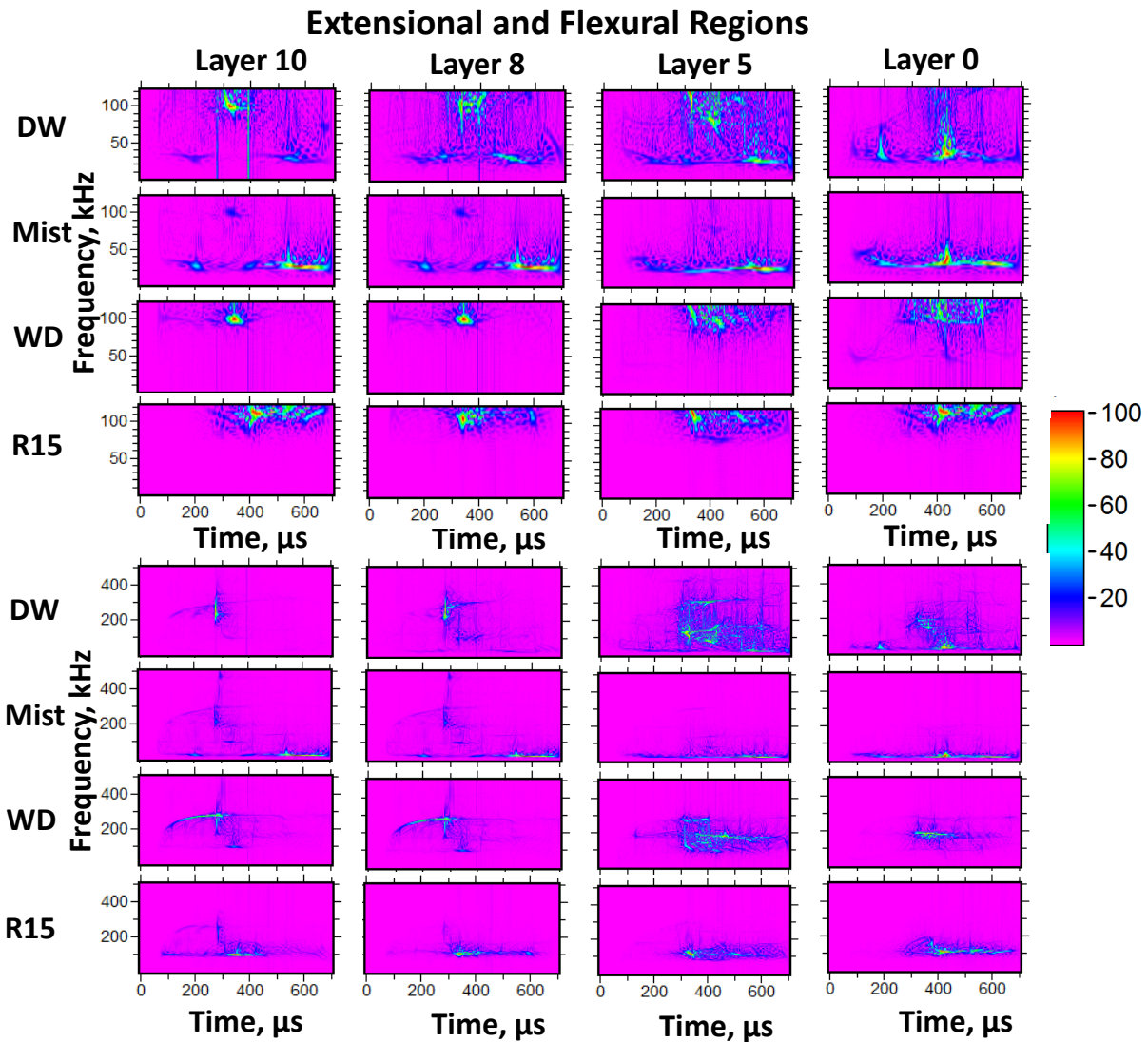


Fig. 12. For the extensional and flexural regions (0 to 700  $\mu$ s), the CWD results are shown in columns for PLBs on layers 10, 8, 5 and 0 for the four sensor types as labeled on the left for the frequency to 120 kHz in the top four rows. The bottom four rows show the same arrangement of information when the frequency is extended to 500 kHz. A color scale of intensity is shown on the right side.

Table 3 Summary of CWD area-pattern matches in extensional region

Sensors/PLB Layer	10	8	5	0
DW and Mist to 120 kHz	IS	IS	IS	PS
WD and R15 to 120 kHz	PS	IS	IS	IS
DW and Mist to 500 kHz	PS	IS	IS	PS
WD and R15 to 500 kHz	IS	IS	IS	IS

Table 4 Summary of CWD area-pattern matches in flexural region

Sensors/PLB Layer	10	8	5	0
DW and Mist to 120 kHz	PS	PS	IS	IS
WD and R15 to 120 kHz	IS	IS	PS	PS
DW and Mist to 500 kHz	PS	PS	IS	IS
WD and R15 to 500 kHz	PS	IS	IS	IS

### C. Additional observations relative to full thickness and/or single layer propagation.

#### i) Waveforms of Mist sensor signals

Due to the strong lower frequency sensitivity of the Mist sensor as a result of the use of hot melt glue coupling, this sensor's waveforms show some clear indications at lower frequencies of the presence of full-thickness Lamb wave propagation due to a contrast in the extensional and flexural regions for PLBs on the ends of layers near the outside and near the inside. Thus, as shown here, these results complement the modal results. Figure 13(a) shows the outer Mist sensor signal (top) for a PLB on layer 9, which is near the layer of the outer sensor, and it also shows the outer sensor signal (bottom) for a PLB on layer 1, which is near the inner layer of the wall. As illustrated in this figure by the vertical red cursor at about  $627 \mu\text{s}$  in the flexural region at about  $24 \text{ kHz } A_1$  mode (per the CWD results for  $84 \text{ mm GV}$ s), there is a complete reversal of phase for the signal from the near outer layer PLB compared to the near inner layer PLB signal (Note that for the  $84 \text{ mm}$  thickness the flexural mode is  $A_1$ , since the frequency at this time for the  $A_0$  mode of about  $2 \text{ kHz}$  is well below the capability of the Mist sensor and is also below the high pass  $10 \text{ kHz}$  filter used). In contrast, the red vertical cursor at about  $121 \mu\text{s}$  in the extensional region at about a frequency of  $35 \text{ kHz } S_0$  mode (per the CWD results for  $84 \text{ mm GV}$ s), shows the signals from PLBs on both the layers are in phase. This phase behavior (same in extensional region and reversed in the flexural region) in the signals from PLBs on the edge near the top of the LPV remnant wall compared to the PLB on the edge near the bottom of the wall thickness is the same as that previously obtained for a sensor on the top surface of a  $3.1 \text{ mm}$  thick aluminum plate, in unpublished work [7] for Lamb waves in the far-field (full-thickness propagation). By use of a broadband conical sensor located on the top surface at  $127 \text{ mm}$  from the PLB edge, the results shown in Fig. 13(b) were obtained. The top waveform was for an in-plane edge PLB near the top surface and the bottom waveform for an in-plane edge PLB near the bottom surface of the plate. In Fig. 13(b), the cursors again show in the flexural region at  $54 \mu\text{s}$  at a frequency of  $50 \text{ kHz } A_0$  mode (per CWD results for aluminum  $3.1 \text{ mm GV}$ s), the phase reversal is present, while in the extensional region at  $11 \mu\text{s}$  at a frequency of  $100 \text{ kHz } S_0$  mode (per CWD results for  $3.1 \text{ mm GV}$ s), the signals are in phase. The ability to show behavior similar to Fig. 13(a) with the other three sensor types is hindered by different factors. With the WD and R15 sensors the resonant behavior as well as a lack of lower frequency response precludes such an illustration. For the DW sensor less low frequency response and higher electronic noise does not allow such an illustration.

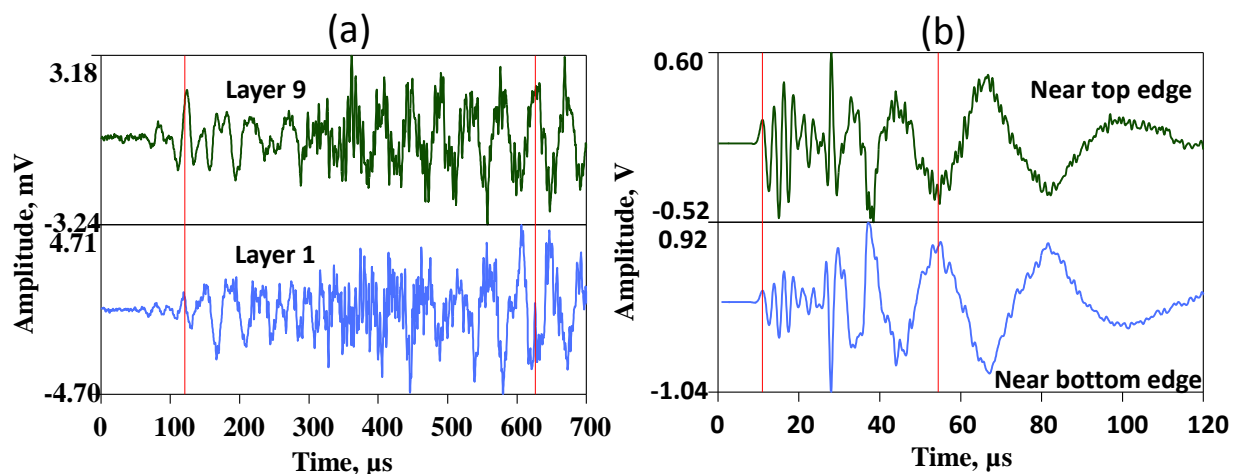


Fig. 13. (a) Example with the remnant for a low frequency portion in Mist outer sensor signals of reversal in phase in flexural region and no reversal of phase in extensional region. (b) Top surface broadband conical sensor signals for PLBs on end of large aluminum plate showing reversal in flexural region and no reversal in extensional region.

ii) Mist sensor CWD in the region of the initial arrival of the extensional mode

By use of Mist sensor results at the very first arrival portion of the extensional mode for a signal portion from 0 to 100  $\mu\text{s}$ , a changeover of mode dominance can be observed in the CWD results in Fig. 14. In this figure, the 84 mm GV's  $S_0$  and  $S_1$  modes are shown in the left column for PLBs on layers 10, 9, 8, 5, 2 and 0 with the CWD results, and the  $S_0$  mode GV for 7 mm thickness is shown along with the same CWD results in the right column for PLBs on the same set of layers. The initial match for the 7 mm  $S_0$  mode can be observed for layer 10 PLB (viewing both columns for these comparisons) and a partial shift to 84 mm GV for layer 8 PLB. Then, the dominance of 84 mm GV for  $S_0$  and  $S_1$  can be seen in the lower layers.

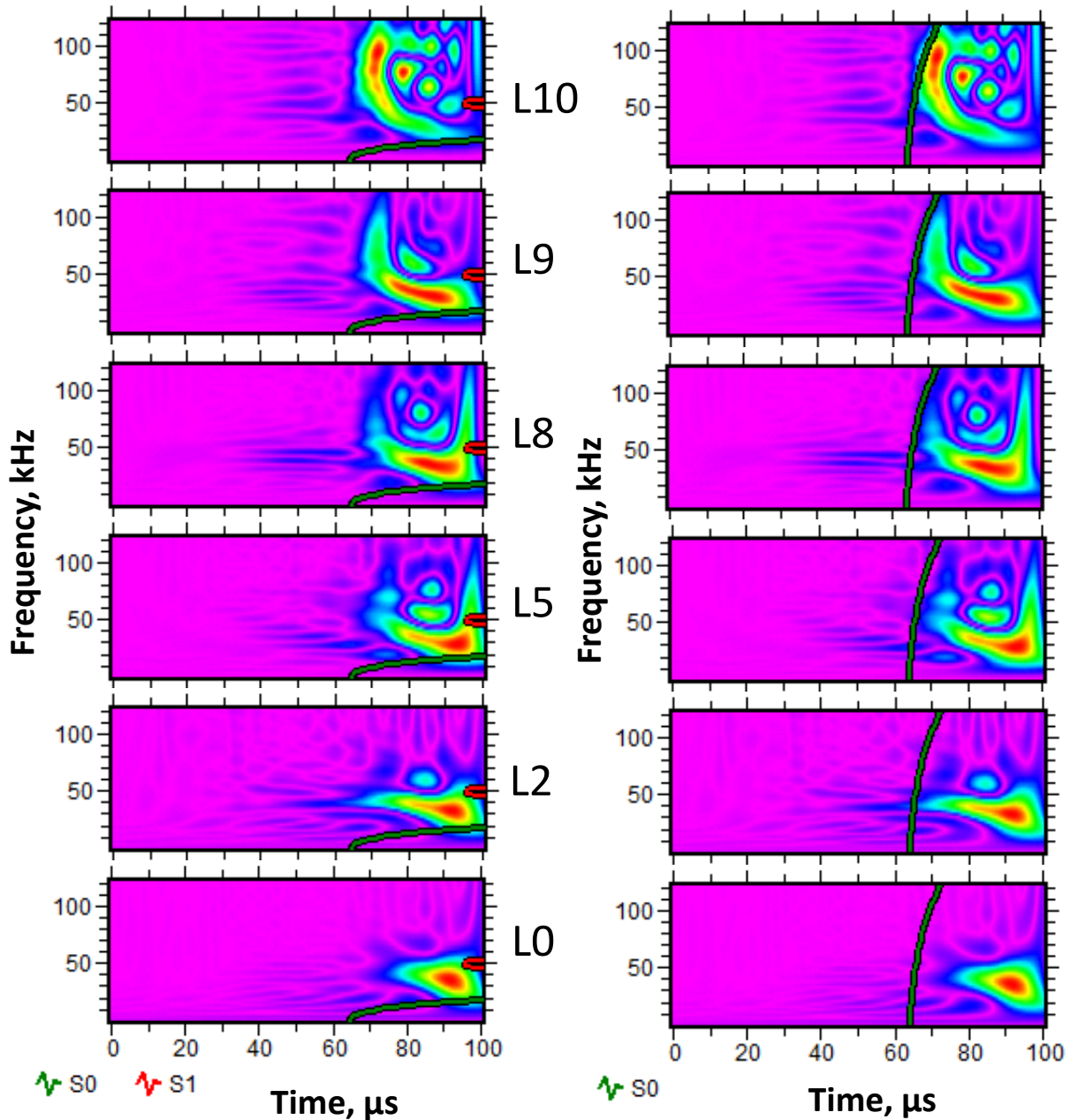


Fig. 14. Mist sensor CWD results very first portion of extensional mode as a function of the PLB layers and with GV's to 120 kHz shown for both the 84 mm thickness (left) and the 7 mm thickness (right).

## Overall Perspectives of the Research Results

When the most intense regions in the CWD results for the outer Mist sensor signals were examined for PLBs on layers 10, 8, 5, 2 and 0, the correspondence of the CWD results was with the 84 mm GVs for full-thickness dominant wave propagation with the peak frequencies ranging from 26 kHz to 32 kHz in all 20 cases in Tables 1 and 2.

For the outer DW sensor signals, the correspondence differed. Out of the 20 cases, the correspondence of the most intense CWD results was with the 84 mm GVs for 15 cases with peak frequencies ranging from 28 kHz to 107 kHz. It is noted that the higher frequencies 100 kHz to 107 kHz may have been influenced in part by single-layer propagation corresponding to 7 mm GVs. For three cases the CWD peak intensity results for the DW sensor signals showed correspondence with the 7 mm GVs for PLBs on the outer layers 10 and 8 when the CWD frequency range extended to 500 kHz.

In summary, the high intensity CWD results for the different broadband outer sensor signals provided evidence of both single-layer and full-thickness propagation when the frequency region of the CWD calculation was extended to 500 kHz for the PLBs on the outer layers 10 and 8. The Mist sensor signals showed peak intensity correspondence with 84 mm GVs (full-thickness propagation), and the DW sensor signals showed peak intensity correspondence with 7 mm GVs (single-layer propagation). Thus, correspondence with the two different modes of propagation depended on both the sensor frequency response characteristics and the frequency range used for the CWD calculation for these outer layer PLBs. For inner layers, the CWD peak intensity for both broadband sensors generally had correspondence with the 84 mm GVs representing full-thickness propagation for most of the PLB layers.

For the outer resonant sensor signals only a very few cases resulted in correspondence of the intense regions with the GV curves, and these were cases of either single-layer or full-thickness Lamb wave propagation. The WD sensor had five out of possible 20 cases (three for 84 mm GVs and two for 7 mm GVs). The R15 sensor had two out of possible 20 cases (both for 84 mm GVs).

Due to the couplant-modified frequency response of the Mist sensor, two other illustrations of full-thickness propagation were observed at low frequencies with this sensor:

- Waveform results at low frequencies (about 24 to 35 kHz) for the outer sensor when compared for PLBs on a near outer layer to those from a near inner layer showed no phase change in the extensional region and a phase reversal in the flexural region. These results are a characteristic of full-thickness propagation.
- At the very first arrival region of the extensional mode, the CWD results showed a transition from correspondence to single-layer propagation for 7 mm GVs to full-thickness propagation for 84 mm GVs as the PLBs moved from the outer layer to lower layers.

Comparisons of the two classes of different outer sensor types for PLBs on the same layer by CWD frequency/time areas of intensity showed some limited area-pattern intensity matches (seven out of possible 16) when the two broadband sensor signal results were compared to each other. For cases where there were such area-pattern matches for the same frequency/time regions, the relative CWD intensities were ordered differently for these two sensors. The key reason for the lack of matches was the couplant modified response of the Mist sensor. The limited CWD area-pattern matches (four out of a possible 16) for the resonant sensors, when compared to each other, were due to the different resonant frequencies of the two sensors.

### Conclusions for Sensors Mounted on the Outer Layer

- The fact that GV curves for 84 mm superimposed on top of the intense CWD results for the Mist sensor signals for all the cases demonstrated that full-thickness Lamb wave propagation was present for PLBs on all the layers when a broadband sensor with only lower frequency response was used.

- For outer layer PLBs, the DW sensor signals showed the presence of single-layer dominant Lamb wave propagation when the frequency range was extended to 500 kHz. For lower layer PLBs, the result was full-thickness propagation similar to the Mist results.
- The peak frequencies that corresponded to 84 mm GVs in the CWD results with the broadband sensor signals were primarily low frequencies ranging from 24 kHz to 32 kHz, with a few possible cases as high as 100 kHz to 107 kHz for peak frequencies in the flexural region.
- The CWD results from the resonant sensor signals along with the GV curves did not conclusively show full-thickness or single layer propagation for nearly all the PLB layers.
- Waveform results at low frequencies (about 24 to 35 kHz) for the Mist outer sensor when compared for PLBs on the ends of a near outer layer to those from a near inner layer showed no phase change in the extensional region and a phase reversal in the flexural region. These results are a characteristic of full-thickness propagation.
- For PLBs on the same layer, area-intensity pattern matches of the CWD frequency/time areas of intensity were limited for both sensor types. For the broadband sensors, it was due to different frequency ranges of response. For the resonant sensors, it was due to the different resonant frequencies of the two sensors.

### Acknowledgements

The author is grateful for the funding, purchase of equipment, facilities and excellent experimental support provided by NASA Marshall Space Flight Center, Huntsville, AL, USA.

### References

1. ASTM Standard E569, "Acoustic Emission Monitoring of Structures During Controlled Simulation," 2013 and ASTM Standard E1419, "Examination of Seamless, Gas-Filled, Pressure Vessels Using Acoustic Emission," 2015a, ASTM International, West Conshohocken, PA.
2. Choi, R., and Williams, W. J., "Improved Time-Frequency Representation of Multicomponent Signals Using Exponential Kernels," *IEEE Transactions in Acoustics, Speech, and Signal Processing*, Vol. 37, pp. 862-871, 1989.
3. Vallen Systeme Gmb, Icking, Germany, <http://www.vallen.de/downloads/>, Vallen Freeware for AGU-Vallen Wavelet version R2010.0202 and Vallen Dispersion version R2010.0202.
4. Kolsky, H., *Stress Waves in Solids*, Dover, New York, 1963.
5. Hamstad, M. A., "Far-field wave propagation signals from pencil lead breaks on the open end of a thick-walled layered cylinder: Part 1 Amplitudes and frequency content," *J. Acoustic Emission*, Vol. 36, pp. 30 – 50, 2019.
6. Hamstad, M. A., "On Lamb Modes as a Function of Acoustic Emission Source Rise Time," *J. Acoustic Emission*, Vol. 28, pp. 41 – 58, 2010.
7. Hamstad, M. A, Unpublished work at the University of Denver, Denver, CO, 2007.

# Detection of Defects in Spur Gears by Acoustic Emission Monitoring

Swati Gautam and Naresh Tandon

CART (Formerly ITMMEC), IIT Delhi, Hauz Khas, New Delhi 110016, INDIA

## Abstract

Many techniques have been used for detection of defects in gears. Vibration measurements along with signal processing methods have extensively been used for this purpose. Acoustic emission measurement is a relatively new technique for condition monitoring of gears. Acoustic emissions are structure borne stress waves in the frequency range of 50 kHz to about 1 MHz which is much beyond the range of vibrations. These measurements have been used for condition monitoring of machines by some researchers. In the present work acoustic emission (AE) measurements have been applied for the detection of local defects in spur gears. The usefulness of several AE parameters has been investigated. The measurements have been performed on standard Institution of Automobile Engineers (IAE) gear test rig using AE measurement system. The AE measurement system used consists of a resonant sensor, preamplifier with 40 dB gain and 2 channel processor. The measurements were performed at different loads of 0, 1 and 5 kg and test gear speed of 2000 rpm. AE parameters such as counts, energy, rms and amplitude were recorded. Circular defects simulating pits were created on one of the teeth of the test gear using spark erosion method. Defect sizes of 0.5, 1 and 2 mm diameter were used for measurements on healthy and defective gears. An increase in level of parameters with increasing defect sizes are observed indicating effective detection of defects. AE energy and rms showed better results as compared to AE counts and amplitude. The AE measurement technique has proven to be effective even for the smallest defect size of 0.5 mm used in the present work showing the usefulness of the technique in detection of defects at an early stage.

**Keywords:** Acoustic emission, spur gear, defect detection, condition monitoring

## 1. Introduction

Condition monitoring of machines and their elements is very important to avoid sudden unexpected failures which result in production stoppages, economic loss and safety issues. Gears and bearings are two common elements in rotating machines. These are critical components in the working of machines requiring application of condition monitoring. Various techniques have been employed for monitoring their condition. Present work was undertaken to study the condition monitoring of gears using acoustic emission (AE) measurements.

Vibration measurement have extensively been used for the detection of defect in gears [1-3]. Many signal processing techniques have also been used to improve detection of defects. Acoustic emission measurement is relatively new technique for condition monitoring of machines. AE is different from audible acoustic noise which is air borne and is generated in 20 Hz to 20 kHz frequency range. Acoustic emissions are structure borne stress waves in the frequency range of 50 kHz to about 1 MHz which is much beyond the range of vibrations. Defects in machine elements are one of the sources of AE generation. Some of the commonly measured AE parameters are, peak amplitude, rise time of the signal, energy, hits and counts. Counts are the number of threshold crossings and hence are dependent upon threshold voltage setting. Threshold setting is used to eliminate background noise from the desired AE signal. AE energy is the area under rectified signal envelope and can be measured as area under the curve of voltage squared. This area is

proportional to signal energy. AE measurements have been used for condition monitoring of gears by some researchers [4-11]. In the present work application of acoustic emission measurements for the detection of local defects in spur gears has been studied. Detailed investigation on the usefulness of several AE measurement parameters has been undertaken.

**2. Experiment**

The measurements have been performed on Institution of Automobile Engineers (IAE) gear test rig as shown in Fig. 1. Photographs of the gear test rig and front view of its gear box are shown in Figs. 2(a) and 2(b), respectively. Test gear has 15 teeth. AE measurement system from Physical Acoustics consisting of a resonant sensor type R15D, preamplifier with 40 dB gain and 2 channel processor was used. Threshold level of 60 dB<sub>AE</sub> was used for the measurements. PDT, HDT and HLT values of 200, 400 and 800 μs respectively were used in the measurement system. The test rig has possibility of applying different torque loads on the gears with the help of a loading arrangement as shown in Fig. 2(a). The measurements were performed at different loads of 0, 1 and 5 kg and test gear speed of 2000 rpm. AE parameters, AE counts, energy, rms and amplitude, were recorded. These parameters are directly displayed on the screen of AE measurement system and their average values were noted. Circular defects simulating pits were created on one of the teeth of the test gear using spark erosion method as shown in Fig. 2(c). The defect was created on the same tooth and its size (diameter) was increased successively keeping same defect depth. Defect diameter of 0.5, 1 and 2 mm diameter were used for the measurements. All the AE measurements were first performed when the gear was in healthy condition (without creation of defect on tooth) and then on defective gears.

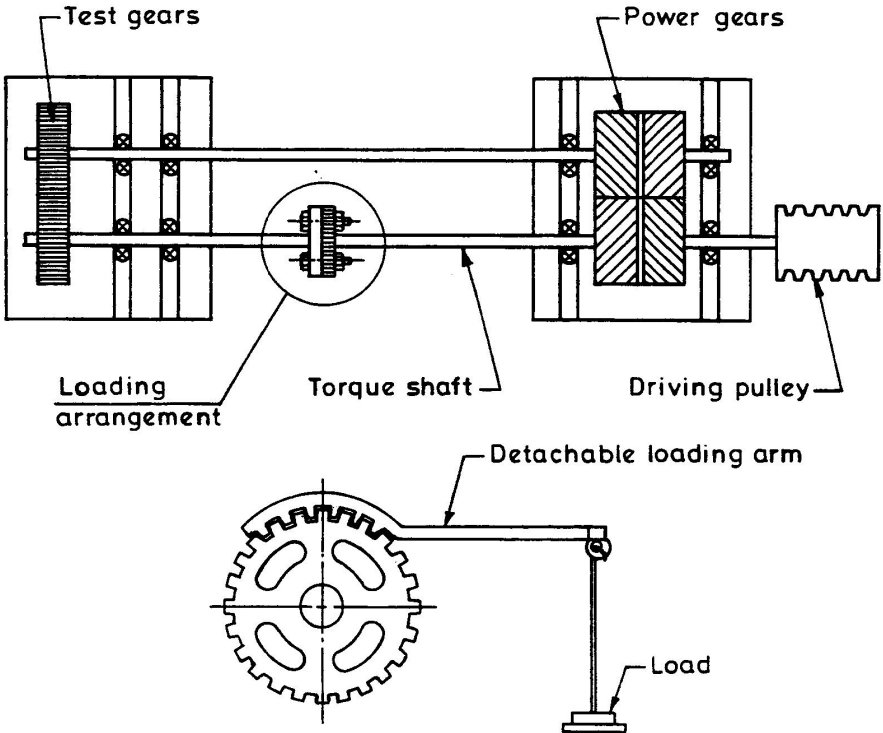


Fig. 1. Schematic diagram of IAE gear test rig [4].

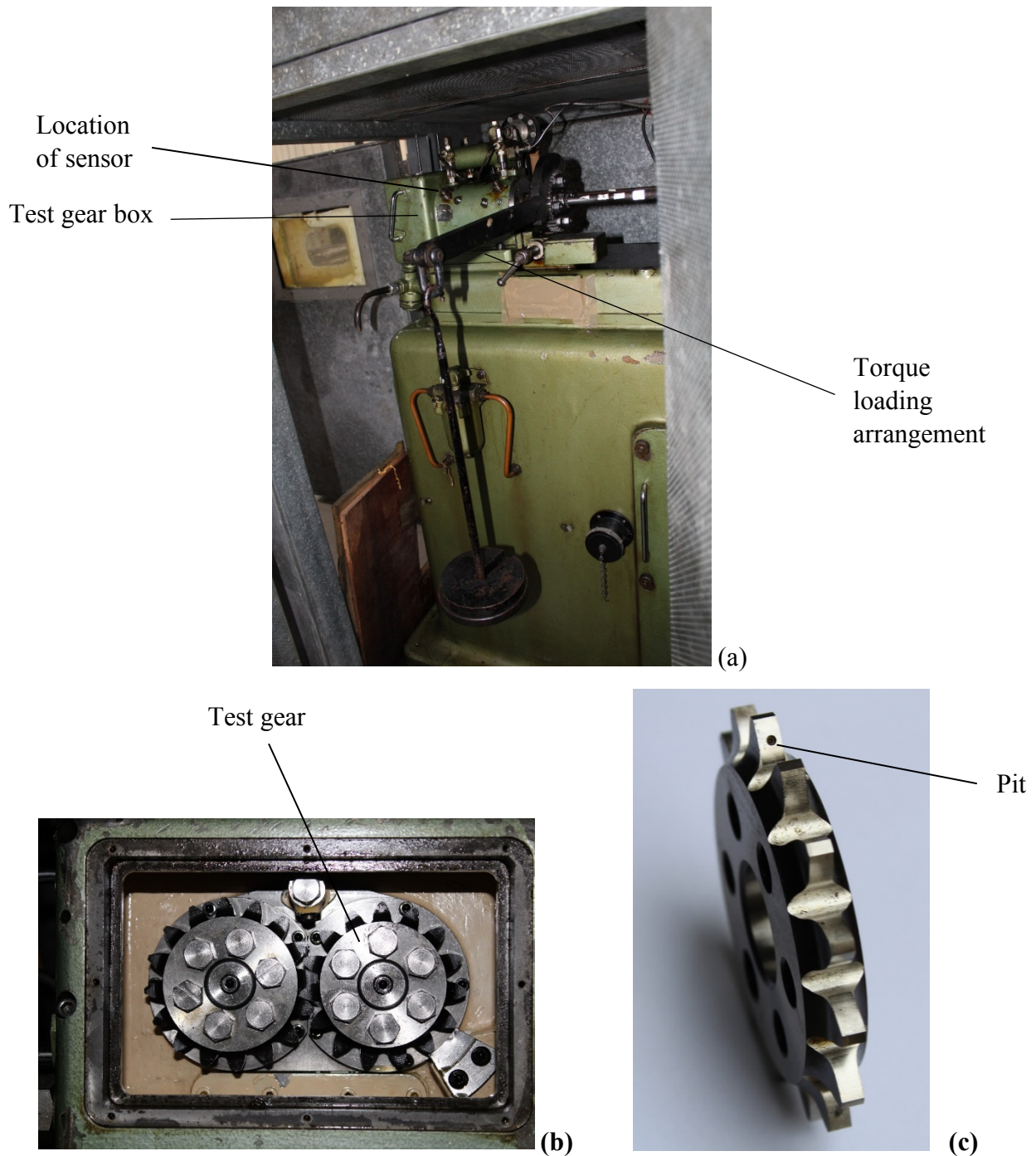


Fig. 2 (a) Gear test rig; (b) Front view of test gear box; (c) Pit created on gear tooth.

### 3. Results and Discussion

Acoustic emission measurement results for AE counts, energy, rms and amplitude for healthy and defective gears are shown in Figs 3 to 5 for 0, 1 and 5 kg loads respectively. All these measurements were recorded for 1 minute duration. The amplitudes shown in  $\text{dB}_{\text{AE}}$  are in reference to  $1 \mu\text{V}$  at the sensor output plus 40 dB from the preamplifier. It is seen that, as expected, the levels of AE parameters increase with increase in load. Also, an increase in levels of all four parameters with increasing defect sizes is observed indicating effective detection of defects. Figure

5 shows that for 5 kg load (corresponding to 22.4 Nm torque), counts have increased from just beyond  $29.4 \times 10^3$  to just beyond  $31.7 \times 10^3$  and rms from 0.56 to 2 volts from healthy gear to the gear with 2 mm defect size. Corresponding increase in energy (aJ) is from just beyond  $36.2 \times 10^8$  to just beyond  $34.2 \times 10^9$  whereas AE amplitude level increase is from 90.5 to 98.7dB<sub>AE</sub>. In terms of percentage, the increase is 7.7%, 262%, 845% and 9.1 % in AE counts, rms, energy and amplitude respectively. The increase is 3.2, 21.1, 105, and 2.8% even for the smallest defect size of 0.5 mm as seen in Fig. 5. Similar increasing trend is also observed for no load and 1 kg load given in Figs. 3 and 4 respectively although the increase is lesser as compared to the higher load of 5 kg.

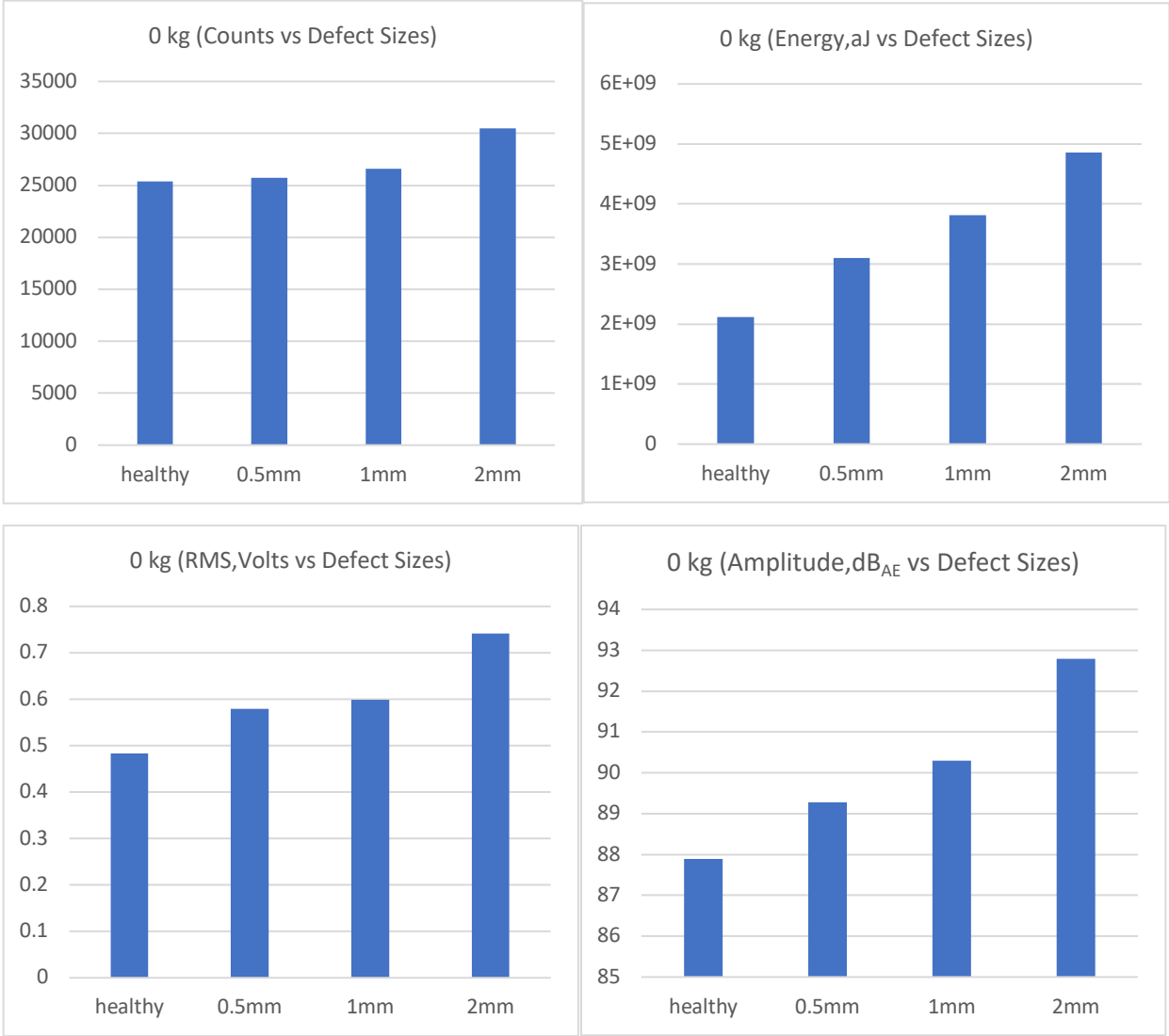


Fig. 3. Acoustic emission of gears at no load.

These results indicate that AE energy is the best parameter for gear defect detection followed by AE rms because the percentage increase in values from healthy to defective gear is the highest in case of energy. AE energy has proved to be a better parameter because it represents the energy level of the AE signal and is independent of the threshold level setting. Counts on the other hand depend upon the threshold level set during measurements and may not give very good results unless an optimum level is found and used. Also, the background noise level can change during measurements requiring adaptive variable threshold level. These could be the reasons for much

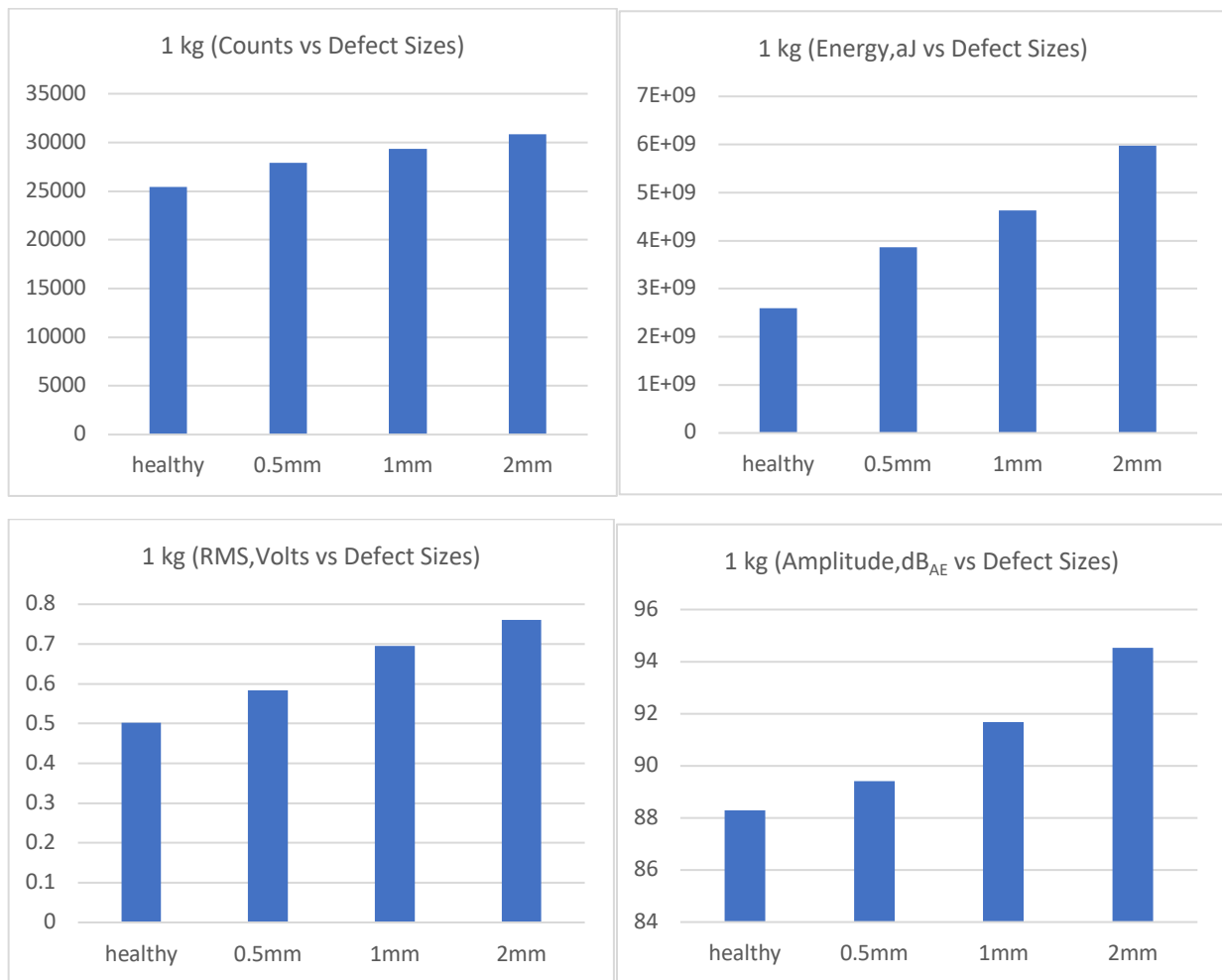


Fig. 4. Acoustic emission of gears at 1 kg load.

less increase in their values. AE energy has also been shown to be effective in detecting oil contamination in journal bearings in a recent study [12].

Figures 3 to 5 also show that there is a significant increase in AE parameters even for the smallest defect size of 0.5 mm. So, the AE measurement technique has proven to be effective in detecting even the smallest defect size of 0.5 mm used in the present work clearly showing the usefulness of the technique in detection of defects at an early stage.

#### 4. Conclusion

A comparison of the values of acoustic emission parameters for healthy and defective gears shows significant increase due to the presence of defects in gear tooth. This indicates that the technique can be effectively used for the detection of defects in gears. AE energy and amplitude show better results as compared to AE counts and rms. The AE measurement technique has detected even a very small defect size of 0.5 mm used in the present study showing the usefulness of the technique for detection of defects at an early stage.

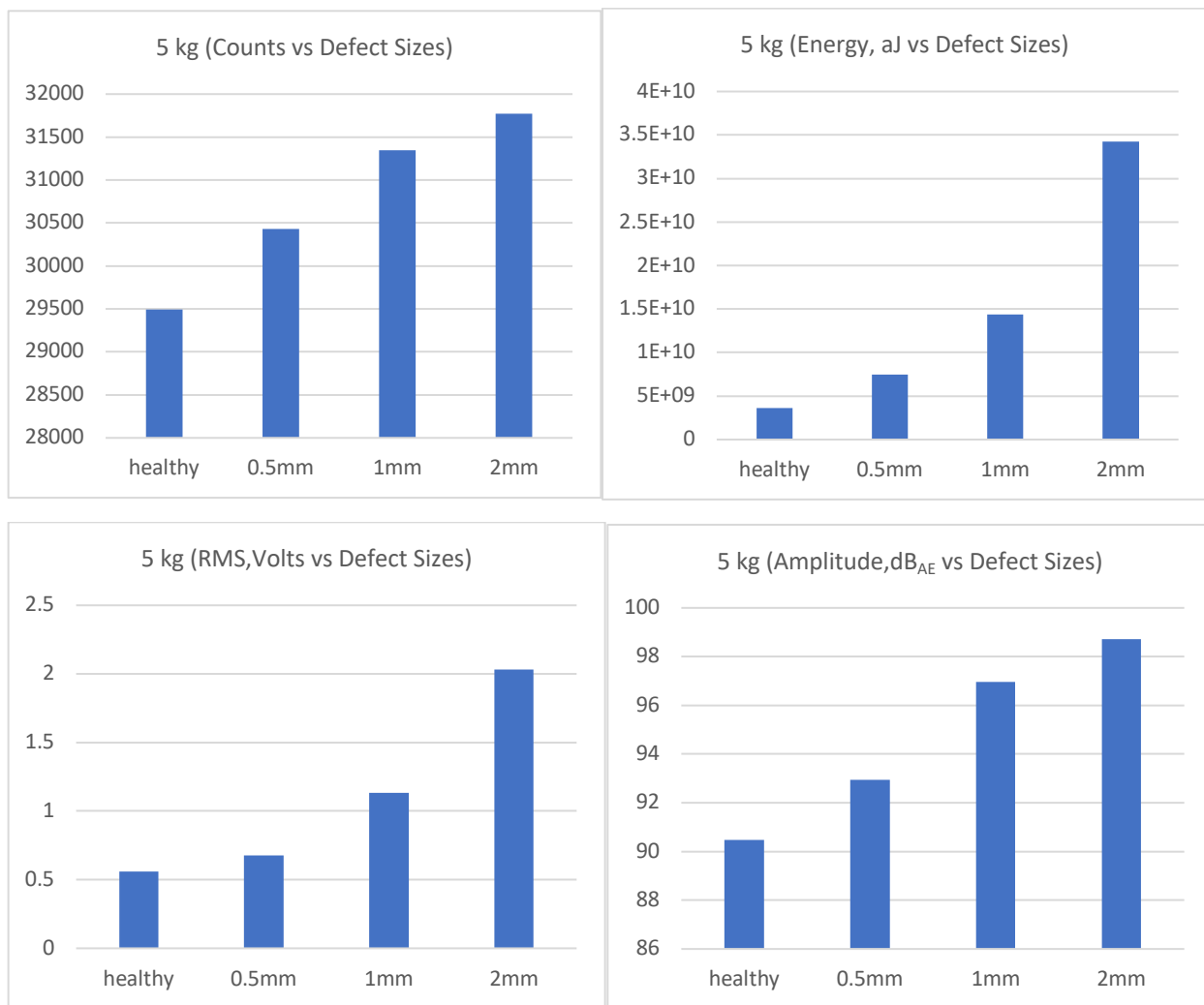


Fig. 5. Acoustic emission of gears at 5 kg load.

## References

1. Loutas TH, Sotiriades G, Kalaitzoglou I, V. et al. Condition monitoring of a single-stage gearbox with artificially induced gear cracks utilizing on-line vibration and acoustic emission measurements. *Appl. Acoust.* 2009; 70: 1148-1159.
2. Tan CK, Irving P and Mba D. A comparative experimental study on the diagnostic and prognostic capabilities of acoustic emission, vibration and spectrometric oil analysis for spur gears. *Mech. Syst and Sig. Process.* 2007; 21: 208-233.
3. Eftekharnjad B and Mba D. Monitoring natural pitting Progress on helical gear gesh using acoustic emission and vibration. *Int. J. Exp. Mech. Strain* 2011; 47:299-310.
4. Tandon N and Mata S. Detection of defects in gears by acoustic emission measurements. *J. Acoust. Emiss.* 1999; 17(1-2): 23-27.
5. Al-Balushi KR and Samanta B. Gear fault diagnosis using energy-based features of acoustic emission signals. *Proc Instn Mech. Eng. Part 1: J. Syst. Cont. Eng.* 2002; 216: 249-263.
6. Ulus S and Erkaya S. An experimental study on gear diagnosis by using acoustic emission technique. *Int. J. Acous. Vibr.* 2016; 21(1): 103-111.

7. Eftekharijad B and Mba D. Seeded fault detection on helical on gears with acoustic emission. *Appl. Acous.* 2009; 70: 547-555.
8. Toutountzakis T, Tan CK and Mba D. Application of acoustic emission to seeded gear fault detection. *NDT and E Int.* 2005; 38: 27-36.
9. Pullin R, Clarke A, Eaton MJ, et al. Identification of the onset of cracking in gear teeth using acoustic emission. *J. Phys.* 2012; Conference Series 382 :012050.
10. Pullin R, Clarke A, Eaton MJ, et al. Detection of cracking in gear teeth using acoustic emission. *Appl. Mech. Mater.* 2010; 24-25: 45-50.
11. Toutountzakis T and Mba D. Observations of acoustic emission activity during gear defect diagnosis. *NDT and E Int.* 2003; 36: 471-477.
12. Poddar S and Tandon N. Detection of particle contamination in journal bearing using acoustic emission and vibration monitoring techniques. *Tribol. Intl.* 2019; 134: 154-164.